UNIVERSITA' DEGLI STUDI DI PADOVA

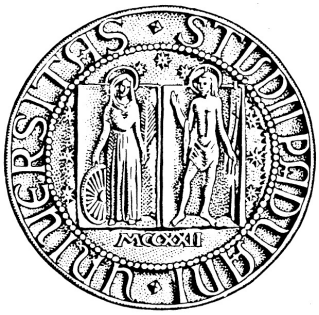

FACOLTA' DI INGEGNERIA

Corso di laurea in Ingegneria Aerospaziale

TESI DI LAUREA

# AERODYNAMIC OPTIMIZATION OF A TRANSONIC AXIAL COMPRESSOR ROTOR

## OTTIMIZZAZIONE AERODINAMICA DI UN COMPRESSORE ASSIALE TRANSONICO

**Relatore:** Prof. Ernesto Benini

**Correlatore:** Ing. Roberto Biollo

**Laureanda**: Giada Abate

UNIVERSITA' DEGLI STUDI DI PADOVA

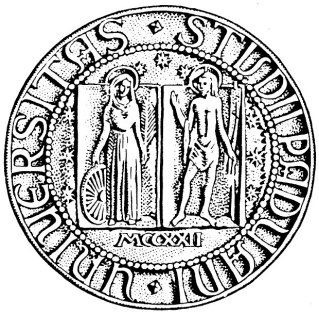

FACOLTA' DI INGEGNERIA

Corso di laurea in Ingegneria Aerospaziale

TESI DI LAUREA

# AERODYNAMIC OPTIMIZATION OF A TRANSONIC AXIAL COMPRESSOR ROTOR

OTTIMIZZAZIONE AERODINAMICA DI UN COMPRESSORE ASSIALE TRANSONICO

**Relatore:** Prof. Ernesto Benini

**Correlatore:** Ing. Robero Biollo

**Laureanda**: Giada Abate

# Abstract

The aim of this study is to carry out an optimization of the NASA Rotor 67 to maximize the isentropic efficiency and the pressure ratio. This is achieved by modifying the stacking line to obtain a swept or leaned blade. In particular, two studies have been done: optimization of the blade tip and optimization of the whole blade. In the optimization of the blade tip, the improvement of the performances of the blade has been made by changing only the shape of the tip. In the optimization of the whole blade, all the sections of the blade have been moved in the circumferential plane. In both optimizations, the geometry of the airfoils does not be changed. The Bezier curves have been used for the parameterization of the geometry, and the MATLAB Genetic Algorithm for the optimization process. For the optimization of the whole blade, it has been referred also to the hierarchical algorithm. Turbogrid and ANSYS CFX have been used to create the mesh (with about 2 millions elements) and to make the simulations. The aim of the optimization is to maximize isentropic efficiency and pressure ratio. The starting values are: isentropic efficiency of 0.8916 and pressure ratio of 1.5558. The result values of the optimization of the blade tip are: isentropic efficiency of 0.8982 and pressure ratio of 1.5562. Hence, the efficiency rise is 0.7% and the pressure ratio increase is 0.025%. Only the isentropic efficiency increase can be considered a good result, while the pressure ratio increase is not significant. The result values of the optimization of the whole blade are: isentropic efficiency of 0.8959 and pressure ratio of 1.5572. Hence, the efficiency rise is 0.5% and the pressure ratio increase is 0.09%. In the optimization of the whole blade, both isentropic efficiency can be considered significant and pressure ratio is again not significant. It is possible that these results have a more increase by raising the number of generations and individuals in the optimization process.

# Ringraziamenti

Con questa tesi si conclude un ciclo di studi impegnativo, con ostacoli e tante soddisfazioni. Vorrei a tal proposito ringraziare chi mi ha accompagnato in questi anni e mi ha aiutato a raggiungere questo obiettivo.
Per prima cosa vorrei ringraziare il prof. Ernesto Benini per avermi dato l'opportunità di lavorare a questo progetto e per la sua grande disponibilità che ha sempre avuto nei confronti di tutti gli studenti.
Ringrazio Roberto Biollo, che mi ha guidato nello svolgimento del mio lavoro di tesi e che si è sempre reso disponibile qualora ne avessi bisogno.
Ringrazio la mia famiglia, che mi ha sostenuto e supportato in questi anni e che mi ha dato la giusta serenità per portare a termine il mio lavoro.
Ringrazio mio zio Rosario, che si è sempre interessato ai miei studi e che ad ogni estate mi ha dato l'occasione per ripassare tutto quello che avevo imparato durante l'anno.
Ringrazio Andrea per l'enorme pazienza che ha avuto, per la forza che mi ha dato nei momenti di difficoltà e per essere stato sempre presente, anche quando era lui ad aver bisogno di un supporto.
Infine, ma non ultimi per importanza, ringrazio i miei compagni di avventure Desko e Flory, che hanno reso questi anni universitari indimenticabili e ricchi di risate anche quando i motivi per ridere erano ben pochi.

# Contents

**Abstract** **i**

**Contents** **vi**

**List of figures** **ix**

**List of tables** **xi**

**Nomenclature and Conventions** **xiii**

**1 Introduction** **1**

**2 Literature review** **5**

2.1 Transonic compressor . . . . . 5

2.1.1 Introduction . . . . . 5

2.1.2 Blade-to-blade flow . . . . . 5

2.1.3 Shock structure and the nature of the flow . . . . . 7

2.1.4 Losses in supersonic blades . . . . . 13

2.1.5 Optimization of supersonic blades: sweep and lean . . . . . 13

2.2 NASA rotor 67 . . . . . 17

2.3 Shape optimization of transonic compressor rotors . . . . . 19

2.4 Geometrical parameterization . . . . . 21

2.4.1 Bezier curves . . . . . 21

2.5 Optimization algorithms . . . . . 22

2.5.1 Definition of optimization problem . . . . . 22

2.5.2 Optimization methods . . . . . 23

2.6 Genetic algorithm . . . . . 25

2.6.1 Binary string . . . . . 25

2.6.2 GA operators . . . . . 26

2.6.3 Pareto ranking . . . . . 29

2.7 Advanced GA . . . . . 30

2.7.1 Distributed GA . . . 30
2.7.2 Hierarchical GA . . . 31
2.7.3 Metamodel assisted GA . . . 32

**3 Methodology 35**
3.1 Introduction . . . 35
3.2 Optimization strategy . . . 35
3.2.1 Optimization of the blade tip . . . 38
3.2.2 Optimization of the whole blade . . . 38
3.3 Mesh . . . 39
3.4 CFD set-up . . . 40
3.4.1 CFX-Pre . . . 43
3.4.2 CFX Solver-Manager . . . 46
3.4.3 CFX-Post . . . 46
3.5 Genetic algorithm set-up . . . 47
3.5.1 Number of generations and number of individuals . . . 47
3.5.2 Selection . . . 48
3.5.3 Reproduction . . . 49
3.5.4 Mutation . . . 51
3.5.5 GA for the optimization of the whole blade . . . 51
3.6 Fitness function . . . 52

**4 Results 53**
4.1 Optimization of the blade tip . . . 53
4.2 Optimization of the whole blade . . . 61

**5 Conclusions 69**

**A Additional results 71**
A.1 Optimization of the blade tip . . . 71
A.2 Optimization of the whole blade . . . 75

**Bibliography 81**

# List of Figures


2.1 Schlieren pictures of cascades with supersonic inlet flow. Stagger 48.5°, camber 14.9°, solidity 1.61, thickness-cord ratio 0.05. Cascade is chocked for $\alpha_1 = 56.8°$. [1] . . . . . 6
2.2 Tip clearance gap secondary flow [2] . . . . . 7
2.3 Tip clearance vortex streamlines [2] . . . . . 8
2.4 Shock configuration - sketch [2] . . . . . 8
2.5 Shock wave configuration inside a transonic compressor rotor [2] . . . 9
2.6 An idealized shock and expansion wave pattern around the forward part of a supersonic rotor row at the 'unique incidence' condition. [1] 9
2.7 Perspective views of the passage shock in a low hub-casing ratio rotor. For each flow rate each of the three views is rotated of 20°. [1] . . . . 10
2.8 Contours of relative Mach number in NASA Rotor 67, 10 per cent of span in from casing at peak efficiency. [1] . . . . . 11
2.9 Contours of casing static pressure beneath a high-speed rotor (550 m/s tip speed) with pronounced negative camber. [1] . . . . . 12
2.10 Sweep and lean definition. [2] . . . . . 14
2.11 Endwall effect on shock structure near the casing. [3] . . . . . 15
2.12 Impact of swept on radial migration of boundary layer fluid particles on subsonic compressor rotor. [4] . . . . . 16
2.13 Impact of sweep on blade loading in the front area near the casing. [5] 16
2.14 NASA Rotor 67. . . . . 17
2.15 Velocity diagrams at design conditions at 10-percent span from tip. . 18
2.16 Swept and leaned stacking line definition. [5] . . . . . 19
2.17 Bezier curves for an aerodynamic airfoil. [6] . . . . . 23
2.18 GA reproduction mechanism. . . . . 26
2.19 Roulette method of selection. . . . . 27
2.20 Crossover . . . . . 28
2.21 Genetic mutation . . . . . 28
2.22 Pareto front [6] . . . . . 29

2.23 Pareto ranking process for a two objective optimization problem. [6] . 30
2.24 Hierarchical GA topology. . . . . 31

3.1 Optimization loop . . . . . 36
3.2 Geometry blade Rotor 67 . . . . . 36
3.3 Blade sections . . . . . 37
3.4 Layers . . . . . 39
3.5 Trend of y+ along the streamwise at 10% of the span . . . . . 41
3.6 Trend of y+ along the streamwise at 50% of the span . . . . . 41
3.7 Trend of y+ along the streamwise at 90% of the span . . . . . 42
3.8 Mesh . . . . . 42

4.1 Evolution of the blade tip optimization. . . . . 54
4.2 $\alpha - \eta$ distribution of the control point at 95% of the span . . . . . 54
4.3 $\alpha - \eta$ distribution of the control point at 100% of the span . . . . . 55
4.4 Mach number at 98% of the span of the initial blade . . . . . 56
4.5 Mach number at 98% of the span of the optimized blade . . . . . 57
4.6 Isentropic efficiency of the original blade and the optimized blade just downstream the blade. . . . . 58
4.7 Mass flow rate of the original blade and the optimized blade just downstream the blade. . . . . 58
4.8 Isentropic efficiency of the original blade and the optimized blade one chord downstream. . . . . 59
4.9 Mass flow rate of the original blade and the optimized blade one chord downstream. . . . . 59
4.10 Isentropic efficiency of the original blade and the optimized blade at duct outlet. . . . . 60
4.11 Mass flow rate of the original blade and the optimized blade at duct outlet. . . . . 60
4.12 Evolution of the whole blade optimization . . . . . 63
4.13 $\alpha - \eta$ distribution of the control point at 33% of the span . . . . . 63
4.14 $\alpha - \eta$ distribution of the control point at 66% of the span . . . . . 64
4.15 $\alpha - \eta$ distribution of the control point at 90% of the span . . . . . 64
4.16 $\alpha - \eta$ distribution of the control point at 95% of the span . . . . . 65
4.17 $\alpha - \eta$ distribution of the control point at 100% of the span . . . . . 65
4.18 Isentropic efficiency of the original blade and the optimized blade just downstream the blade. . . . . 66

4.19 Mass flow rate of the original blade and the optimized blade just downstream the blade. . . . . 66
4.20 Isentropic efficiency of the original blade and the optimized blade one chord downstream. . . . . 67
4.21 Mass flow rate of the original blade and the optimized blade one chord downstream. . . . . 67
4.22 Isentropic efficiency of the original blade and the optimized blade at the duct outlet. . . . . 68
4.23 Mass flow rate of the original blade and the optimized blade at the duct outlet. . . . . 68

A.1 Fig. PR of the original blade and the optimized blade just downstream the blade . . . . . 72
A.2 Fig. Total temperature ratio of the original blade and the optimized blade just downstream the blade . . . . . 72
A.3 Fig. PR of the original blade and the optimized blade one chord downstream . . . . . 73
A.4 Fig. Total temperature ratio of the original blade and the optimized blade one chord downstream . . . . . 73
A.5 Fig. PR of the original blade and the optimized blade at the duct outlet. . . . . 74
A.6 Fig. Total temperature ratio of the original blade and the optimized blade at the duct outlet. . . . . 74
A.7 PR of the original blade and the optimized blades just downstream the blade . . . . . 76
A.8 PR of the original blade and the optimized blades just downstream the blade . . . . . 76
A.9 PR of the original blade and the optimized blades one chord downstream 77
A.10 PR of the original blade and the optimized blades one chord downstream 77
A.11 PR of the original blade and the optimized blades at the duct outlet . 78
A.12 PR of the original blade and the optimized blades oat the duct outlet 78

# List of Tables

4.1 Tip optimization results . . . . . 53
4.2 Blade optimization results . . . . . 61

# Nomenclature and Conventions

## Abbreviations

| | |
|---|---|
| **PR** | Pressure Ratio |
| **GA** | Genetic Algorithm |
| $P$ | Total pressure |
| $T_t$ | Total temperature |
| $\eta$ | Isentropic efficiency |
| $\gamma$ | Ratio of constant pressure and constant volume specific heat |

## Subscripts and superscripts

| | |
|---|---|
| **1** | At duct inlet |
| **2** | At duct outlet |

# Chapter 1

# Introduction

Modern high-performance aircraft engines require that the compressors operate at higher efficiency and higher pressure ratios. The reason is that high values of pressure ratios are important to reduce the engine weight and size. Therefore, it is possible to reduce engine costs, in particular the operational costs. In the past few decades, a lot of investigations have been conduced to understand the three-dimensionality of the flow and the structure of the shock waves in transonic compressor rotors.

Many techniques and approaches have been developed to improve the compressor performance. Among them, the study and the optimization of the blade sweeping and curvilinear stacking have shown noticeable performance improvement. With the rapid progress of computer technology and numerical schemes for computational fluid dynamic (CFD), it has become possible to apply Navier-Stokes equations to three-dimensional viscous flow field analysis in turbomachinery. Indeed, the 3D simulation of a transonic blade was impossible to do in the past decades, due to the low power calculation. The flow in a transonic compressor blade is characterized by shock waves. Hence, the simulation of these blades need a high number of cells to analyze the flow and to obtain plausible results. Many three-dimensional viscous flow codes have also been developed, validated and applied in industry. The lower time cost and higher accuracy of these methods have made possible to solve the real design problems to study the effect of three-dimensional blade stacking. Recently, the use of sweep and lean in axial flow compressor rotor has become a matter of interest in the design of turbomachinery blades. These shape parameters are generally introduced in transonic compressor rotor to reduce shock losses, the corner separation in the blade hub, and tip clearance losses. The first investigation that tries to understand the impact of axially swept and tangentially leaned blades on the aerodynamic behaviour of transonic axial flow compressor rotors was made on NASA Rotor 37. Simulations showed the possibility to increase the overall efficiency of the

baseline rotor (up to 1.5 percentage points at the nominal working condition) using a blade properly curved downstream (aft swept) or inclined towards the direction of rotor rotation (forward leaned).

The aim of this thesis is to try to optimize a transonic compressor blade. In particular, the NASA Rotor 67 has been considered for the optimization process. Rotor 67 is a rotor with a low-aspect-ratio, and it is the first-stage rotor of a two-stage fan. This study wants to maximize the isentropic efficiency ( $\eta$ ) and the pressure ratio ( PR ). The optimization process has been made by changing the stacking line of the blade. The geometry of the airfoils has been unchanged, but the sections of the blade have been moved on the circumferential plane. Hence, the overall geometry of the blade has been changed. In particular, this study is divided into two parts: the optimization of the blade tip, and the optimization of the whole blade. The study of the tip of the blade is important to understand its influence on the performance of the blade. Few studies have been done on this topic in the transonic compressor rotors, hence, there is much interest in this field.

The geometry of the Rotor 67 is discretized by 14 sections. The Bezier curves have been used for the geometrical parameterization. In particular, they define the position of the airfoils on the circumferential plane. The displacement of the blade sections has been described by the displacement angle $\theta$. Hence, a Bezier curve with four control points (on 0%, 33%, 66%, 90% of the span) has been built to define the $\Delta\theta$ of the section 1 until the section 12 of the blade. The optimization coefficients $\Delta\theta$ of the last two sections (tip region) have been kept independent. Six optimization coefficients have been used for the optimization of the whole blade, and two for the optimization of the tip. The $\Delta\theta$ increase must be add to the theta-coordinates of the old geometry to give the theta-coordinates of the new geometry. Some $\Delta\theta$ limits have been imposed, beyond which the simulation trends to diverge. The $\Delta\theta$ limits are: $\pm 0.5°$, $\pm 1°$, $\pm 1.5°$ for the control points respectively at 33%, 66% and 90% of the span. The two control points of the tip are bound to the position of the control point at 90% of the span. Hence, the $\Delta\theta$ limits for these two points are $\pm 1°$ and $\pm 2°$, and they are referred to the control point at 90% of the span, that is fixed in the optimization of the tip, and movable in the optimization of the whole blade. The genetic algorithm has been used for the optimization, in particular MATLAB GA has been considered. The genetic algorithms are one of the most suitable methodology for aerodynamic optimization problems. Aerodynamic optimization is a "noisy" problem, and the GA is able to explore efficiently the whole design space without getting trapped in local minima. This is the reasons why it has been decided to use the genetic algorithm for this optimization process. The

computational time is high for the optimization of the whole blade. The hierarchical GA is a way to accelerate the GA by using a low fidelity model for a first optimization process. The objective function is evaluated by using less accurate tools, which can be achieved by reducing the number of grid points or by reducing the complexity of the analysis. These models are computationally less expensive but have a lower accuracy. Each promising individual based on the low fidelity optimization needs to be reevaluated by the high fidelity model. Hence, this method should speed up the convergence of the optimization process. Hence, a coarse mesh and a fine mesh have been used for the optimization of the blade. The individuals on the Pareto front of the optimization with the coarse mesh have been put on the initial population of the second optimization with the fine mesh. In this way, the time of simulation has been reduced. The computer programs used for the optimization process are: Turbogrid to generate the mesh and ANSYS CFX for the simulations.

# Chapter 2

# Literature review

## 2.1 Transonic compressor

### 2.1.1 Introduction

Today, transonic axial-flow compressor rotors are used in aircraft engines to obtain maximum pressure ratios per single stage with a high efficiency. High values of total pressure ratios are important to decrease the number of stages and hence the compressor weight and size.

Actually, the total pressure ratio of the stage is increased by giving the rotor a higher tip speed. Hence, there are higher relative flow velocities at the outer span in the transonic compressor rotors; therefore, the blade is affected by a transonic flow field: supersonic at the outer span and subsonic at the inner span. Due to the supersonic flow, there are intense shock waves close to the blade tip and over part of span; this fact entails a lower efficiency of the transonic compressor than traditional subsonic solutions.

Today, one of the most promising technological evolution to improve the performance of transonic compressor rotors is the application of sweep and lean, roughly speaking, the use of a curvilinear stacking line leading to a three-dimensional shaped blade. "However, the effects of sweep and lean on the aerodynamic behavior of transonic rotors were not completely understood and further studies are needed. This is mainly due to the complexity of the flow field inside these machine" [7].

### 2.1.2 Blade-to-blade flow

The supersonic flow has a subsonic axial velocity at the blade inlet. The shocks or expansion waves produced by the blades may propagate upstream; in this way the compressor is able to influence the incoming flow. "If the supersonic inlet flow

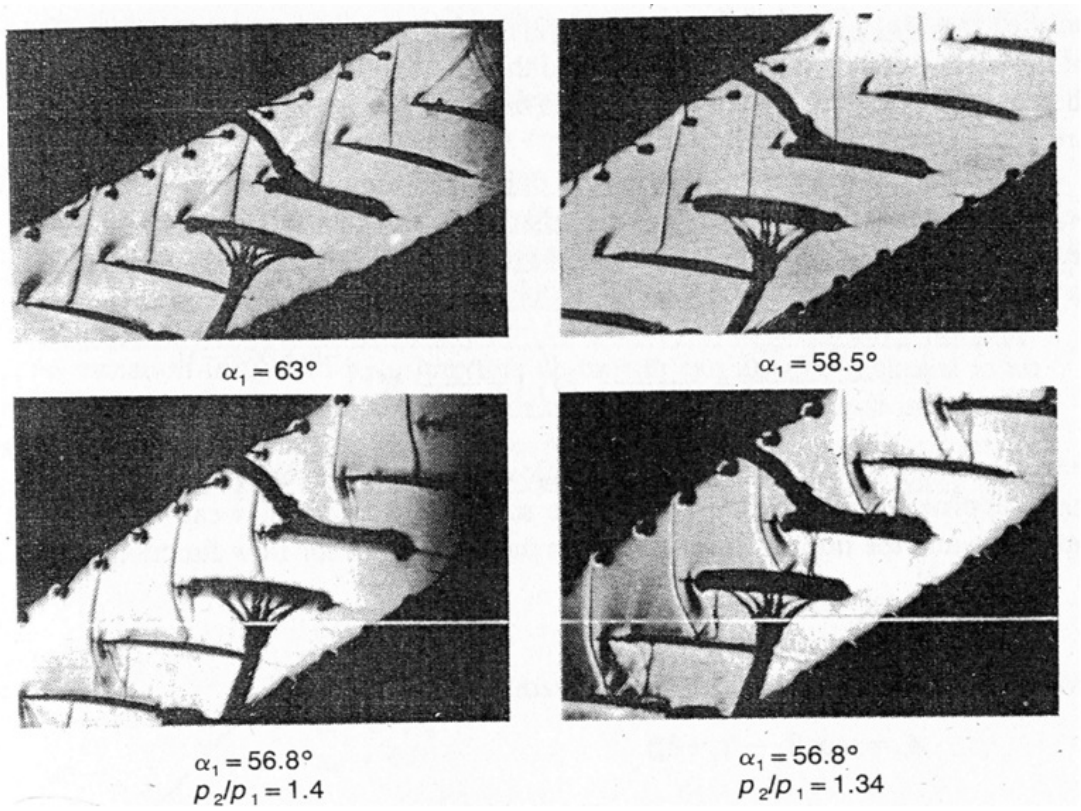


**Figure 2.1:** Schlieren pictures of cascades with supersonic inlet flow. Stagger 48.5°, camber 14.9°, solidity 1.61, thickness-cord ratio 0.05. Cascade is chocked for $\alpha_1$ = 56.8°. [1]

blading has a subsonic axial velocity it follows that the tangential component of velocity will be high, hence supersonic compressor blades are highly staggered, often by more than 60°to the axial direction" [1].

The deceleration of the relative velocity in the blade passage would normally be accomplished with one or more shockwaves. Therefore, supersonic blades have two features: a very small camber and a very low thickness (about 2 per cent of chord for the tip section of a transonic fan). The shock pattern is not only affected by the geometry of the blade but also very strongly by the inlet Mach number, the inlet flow direction and the back pressure behind the blade row.

The Fig. 2.1 shows blades in linear cascade with an inlet Mach number just above unity. Two of the pictures are for the choked condition but with different back pressure. The flow pattern is simpler at the lower flow rate (higher incidence), with the shock at the leading edge that dominates and creates the majority of the pressure rise. The complexity of the flow field makes the aerodynamic design of transonic compressor rotors very hard. Some complex flow features are not still completely understood and consequently the optimization process remains hard.

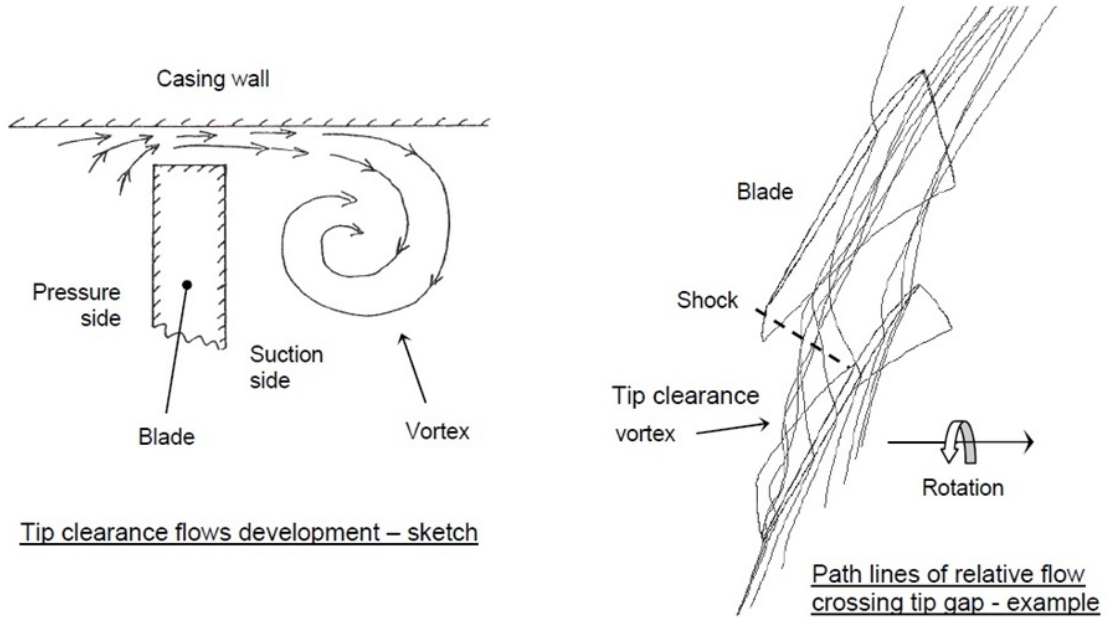


**Figure 2.2:** Tip clearance gap secondary flow [2]

The most detrimental region in transonic compressor rotors is the tip endwall region where the tip gap region develops intense secondary flows (Fig. 2.2). "The pressure difference between the suction side and the pressure side drives the fluid through the blade tip gap, inducing a jet which propagates into the main flow. The interaction between the jet and the main flow gives rise to a vortex ('tip clearance vortex') which generally starts at the leading edge and develops into the passage" [2]. From the interaction between these tip clearance flows, the casing boundary layer and the passage shock arise a complex flow structure that has detrimental effects on the overall rotor performance and induces aerodynamic losses, blockage and instabilities.

Interacting with the shock, the tip clearance vortex is subject to a sudden and strong deceleration, and this interaction has a key role on rotor instability. In particular, the vortex breakdown can occur at lower flow operating conditions, as illustrated in Fig. 2.3. Depending on the intensity of the interaction, this phenomenon can induce the compressor stall.

### 2.1.3 Shock structure and the nature of the flow

The supersonic flow generates intense shock waves with a three-dimensional structure. "At the outer span of the blade, the relative flow is supersonic and the deflection imposed by the blade pressure side wall gives rise to a shock wave, which starts from the blade leading edge and propagates into the blade passage" [2] (Fig. 2.4).

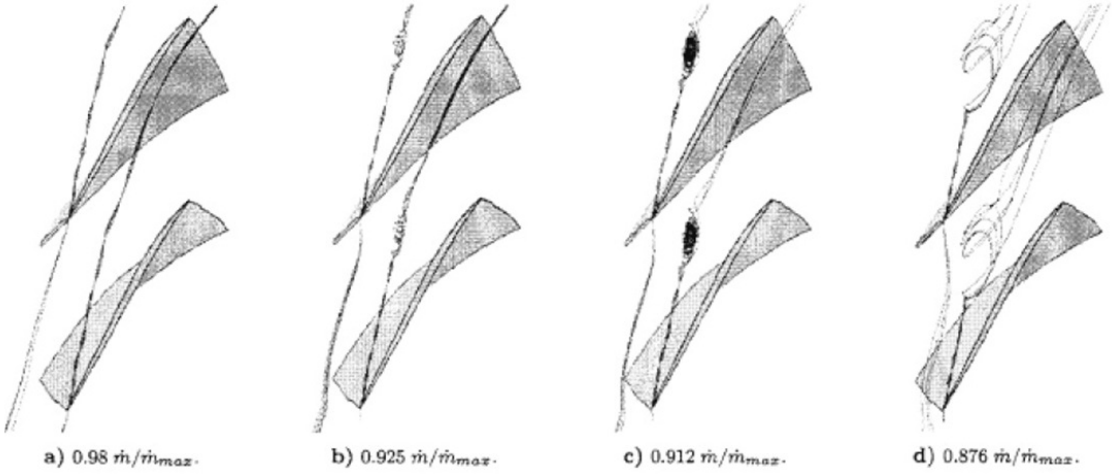


**Figure 2.3:** Tip clearance vortex streamlines [2]

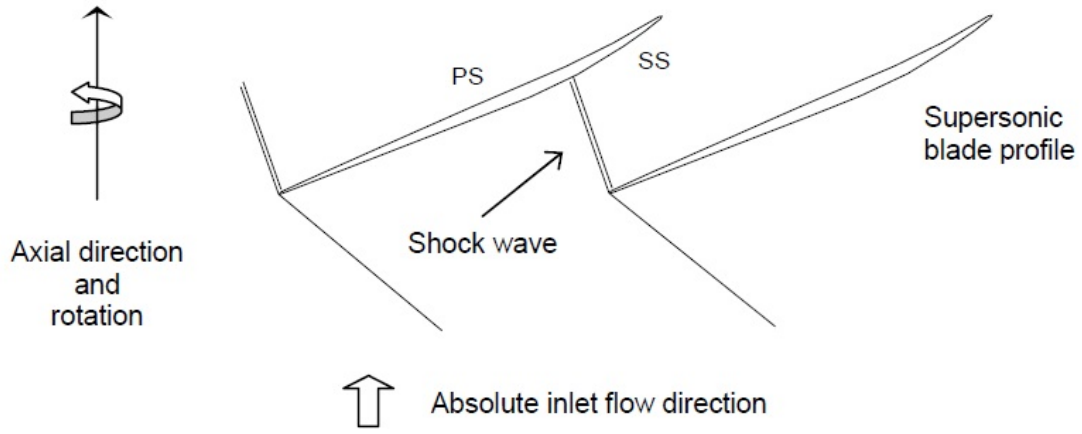


**Figure 2.4:** Shock configuration - sketch [2]

The shock is an irreversible process, and it induces entropy generation that influences negatively the rotor efficiency. In addition, the interaction between the shock and secondary flows (tip clearance flows and wall boundary layers) has a negative impact on the local flow field with negative effects on the overall rotor performance. The interaction between the shock and tip clearance flows is one of the main reasons of stall in transonic compressor rotors.

The shock can develop in different way, depending on rotor geometry and operating conditions. The Fig. 2.5 shows the blade-to-blade shock configuration inside a generic transonic compressor rotor.

The Fig. 2.6 shows an idealized choked flow with a subsonic axial velocity, and oblique shock waves and expansion waves are shown. The shocks are attached to the leading edge, and the type of floe is known as 'unique incidence'. Most of

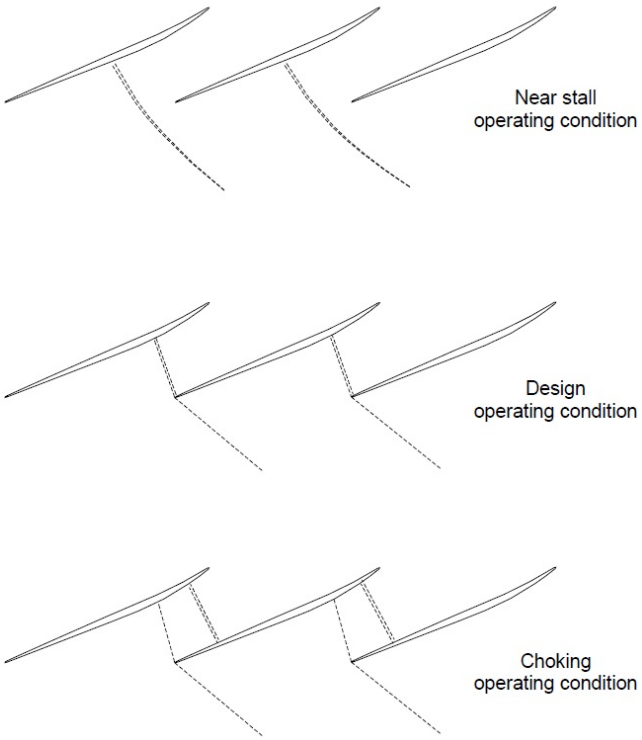


**Figure 2.5:** Shock wave configuration inside a transonic compressor rotor [2]

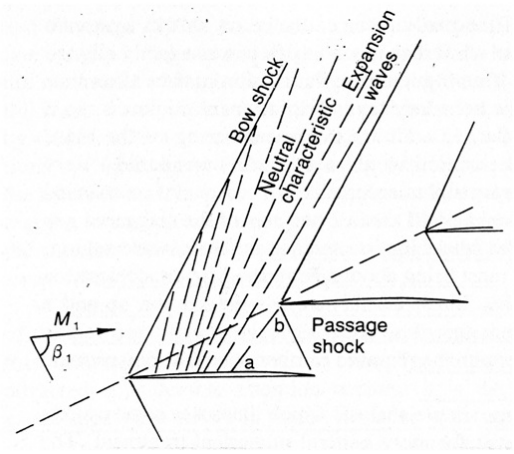


**Figure 2.6:** An idealized shock and expansion wave pattern around the forward part of a supersonic rotor row at the 'unique incidence' condition. [1]

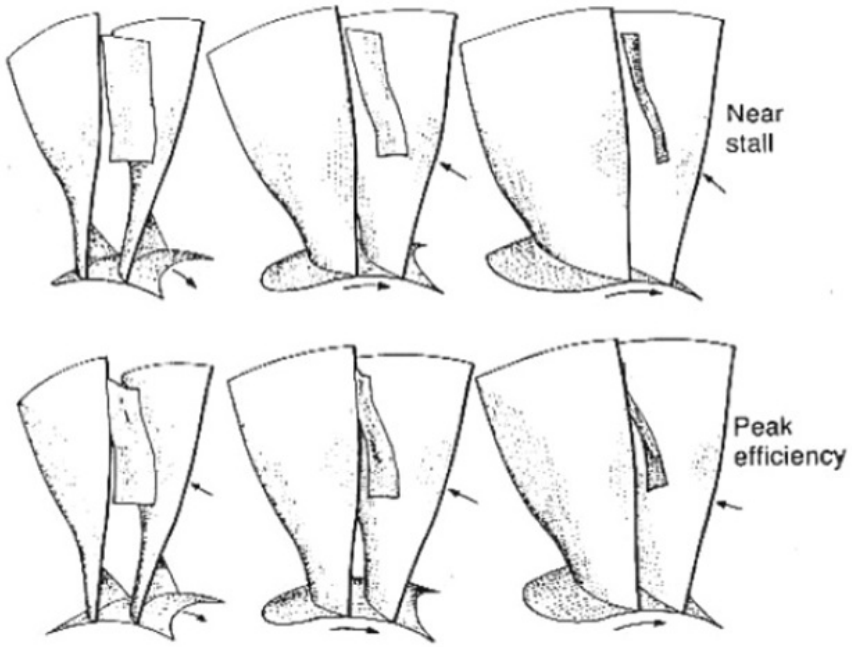


**Figure 2.7:** Perspective views of the passage shock in a low hub-casing ratio rotor. For each flow rate each of the three views is rotated of 20°. [1]

the pressure rise is produced by the passage shock. The bow shock is caused by the leading edge thickness and also by the expansion waves produced by the blade suction surface curvature. The expansion waves interact with the shocks upstream of the blades. The flow in the figure has one expansion wave ab which passes from the suction surface of one blade to the leading edge of the next. Therefore, the flow is supersonic in the region between the ab wave and the passage shock.

"Any curvature of the blade suction surface in the forward region - where the flow is supersonic - must bring about a Prandtl-Meyer acceleration of the flow leading to a higher Mach number across the section ab, and therefore, a lower mass flow" [1]. Hence, it is usual to make the forward region of the blades as flat as possible.

"Generally, the shock shifts upstream and becomes normal to the incoming flow as the operating point moves toward lower mass flow operating condition, as a consequence of the higher flow incidence due to the lower mass flow rate" [2]. The Fig. 2.7 shows some 3D views of a shock front at peak efficiency and near stall conditions in a transonic rotor with a low hub-casing ratio.

The three-dimensional structure of the shock requires a three-dimensional treatment to understand and to study the flow into a transonic compressor rotor. "Fig. 2.8 shows calculated and measured Mach numbers for a section near the tip of NASA Rotor 67 at the condition of peak efficiency. The calculated results, using Denton three-dimensional code, are for an inviscid calculation and another included

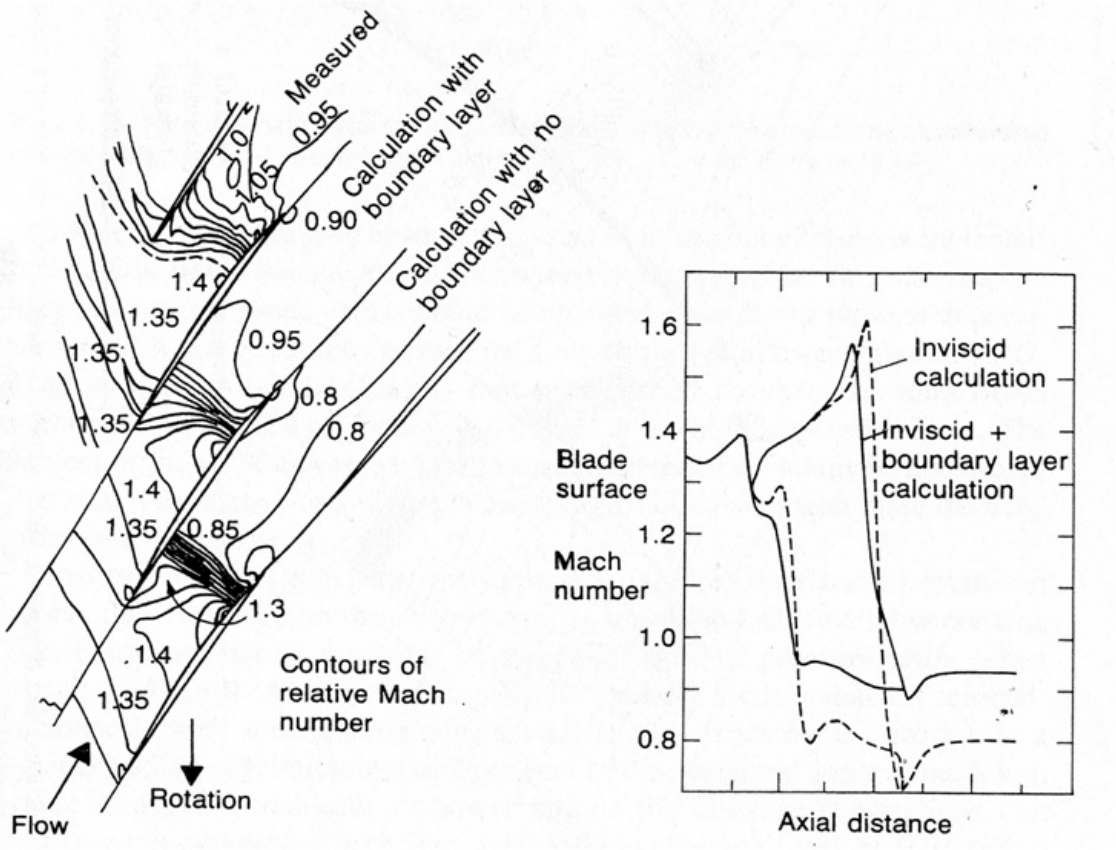


**Figure 2.8:** Contours of relative Mach number in NASA Rotor 67, 10 per cent of span in from casing at peak efficiency. [1]

a very simple boundary layer prediction" [1]. Including the boundary layer, the Mach numbers contours agree quite well with the measurements. The absence of the boundary layer blockage does lead to a significant overestimate of blade loading, most evident in the right-hand part of the figure where the surface Mach numbers are plotted against chord-wise distance. It can also be seen that the shock is further downstream without the boundary layer. On the other hand, if the boundary layer is considered, the shock begins at the leading edge and appears to reflect off the suction surface.

The three-dimensional calculations demonstrate that nearly all the pressure rise takes place across the passage shock. Just as most of the pressure rise is being produced in the leading edge region, it is also true that this is the region with most of losses. In the tests made by Starken and Lichtfuss [8], "it was realized that the shock could separate the boundary layer on the suction surface and that the loss then became sensitive to the cascade solidity" [1]. This fact happens because high solidity allows a separated boundary layer to reattach. The Reynolds number influences the possibility of boundary layer separation. After a laminar separation, the ability to

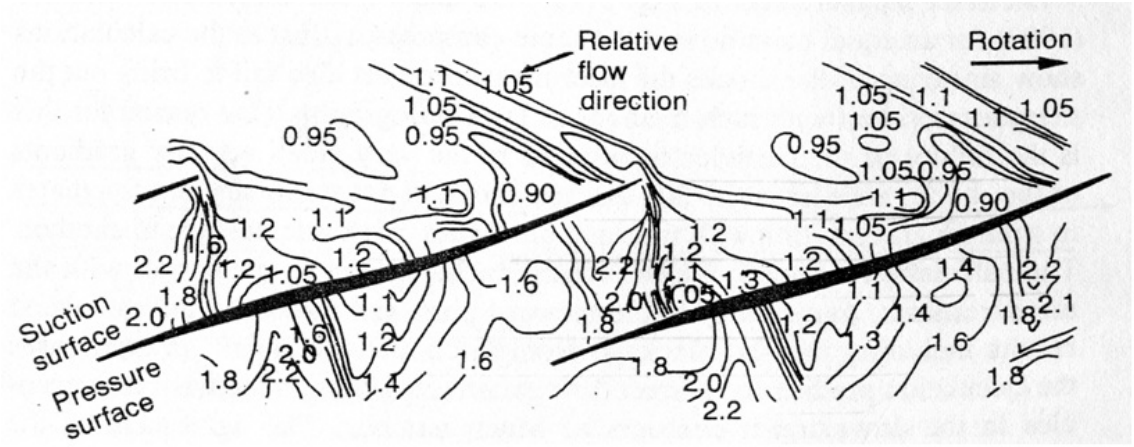


**Figure 2.9:** Contours of casing static pressure beneath a high-speed rotor (550 m/s tip speed) with pronounced negative camber. [1]

resist separation or to reattach of a turbulent flow rises with the Reynolds number.

From this cascade tests, it was also clear that the strength of the shock was increased by the amount of convex curvature on the suction surface between the leading edge and the shock. Hence, the expansion could be minimized by having a very flat suction surface. This is the reason why there is a curvature in the opposite sense (negative camber) in the leading edge region, with a gradual compression along the suction surface. "This may be thought of in two ways: the curvature of the blade surface towards the tangential produces compression waves which may coalesce into a series of weak oblique shocks; alternatively, but equivalently, the flow cross-sectional area is decreased in the flow direction by this negative camber and this leads to a deceleration of the supersonic flow" [1]. The Fig. 2.9 shows an example of pronounced negative camber.

In 1988, Ginder and Calvert [9] described the design of a rotor for a tip inlet relative Mach number of 1.47. "With a conventional blade the Mach number was predicted to be 1.5 in front of the passage shock, causing the suction surface boundary layer to separate and reattach just before the trailing edge. With negative camber the Mach number ahead of the shock was reduced to 1.4 and the boundary layer separated for only a short length and the predicted loss was substantially reduced. Ginder and Calvert point out that the success of the design depends critically on the response of the boundary layer to the shock, for with only slightly more blockage the negatively cambered blade could choke" [1].

### 2.1.4 Losses in supersonic blades

The estimation of loss in supersonic compressor blades has been a subject of major concern. Whereas for subsonic flow the blade-to-blade loss is not so important compared to other sources of loss and other aspects of blade performance, "with supersonic inlet velocities the blade-to-blade loss can be so large as to be of first-order importance" [1].

In 1961, Miller [10] assumed that the loss could be divided in two parts: the loss created by the shock across the passage from one leading edge to the next (the passage shock) and the profile loss (analogous to the loss in subsonic blades). This division is not physically plausible because the shock waves bring about the separation of boundary layers. Hence, where the shock wave intersects the adjacent suction surface, it affects the profile loss (the drag) that depends on the boundary layer thickness. Therefore, the shock wave loss and the profile loss cannot be considered separated.

At the present time, the Navier-Stokes methods for three-dimensional flow seem able to give good indications of the overall flow pattern, static pressure variations and the distribution of loss. "The accurate prediction of loss probably requires a fairly accurate description of shear stresses (and therefore turbulent modelling) whereas the overall flow pattern is only a weakly sensitive to this" [1].

In 1989, Freeman and Cumpsty [11] found that the minimum loss was that of a normal shock at the inlet Mach number ahead of the blades but this could only be achieved for zero thickness blades at zero incidence. The calculations show that loss is a strong function of incidence and blade speed. The thickness has only a small effects on loss for a given incidence. However, thickness determines the minimum incidence at which chocking occurs. Therefore, the knowledge of internal flow - in particular the impact of shock waves on the overall flow field - is fundamental when the objective is to improve the aerodynamic behavior of a transonic compressor rotor.

### 2.1.5 Optimization of supersonic blades: sweep and lean

Recently, the use of sweep and lean in axial flow compressor rotor has become a matter of interest in the design of turbomachinery blades. These shape parameters are generally introduced in transonic compressor rotor to reduce shock losses, the corner separation in the blade hub and tip clearance losses. "Traditionally, rotor blades are radially-stacked. The application of sweep and/or lean leads to a curvilinear stacking line, i.e. to a three-dimensional shaped blade" [2]. As shown in Fig.

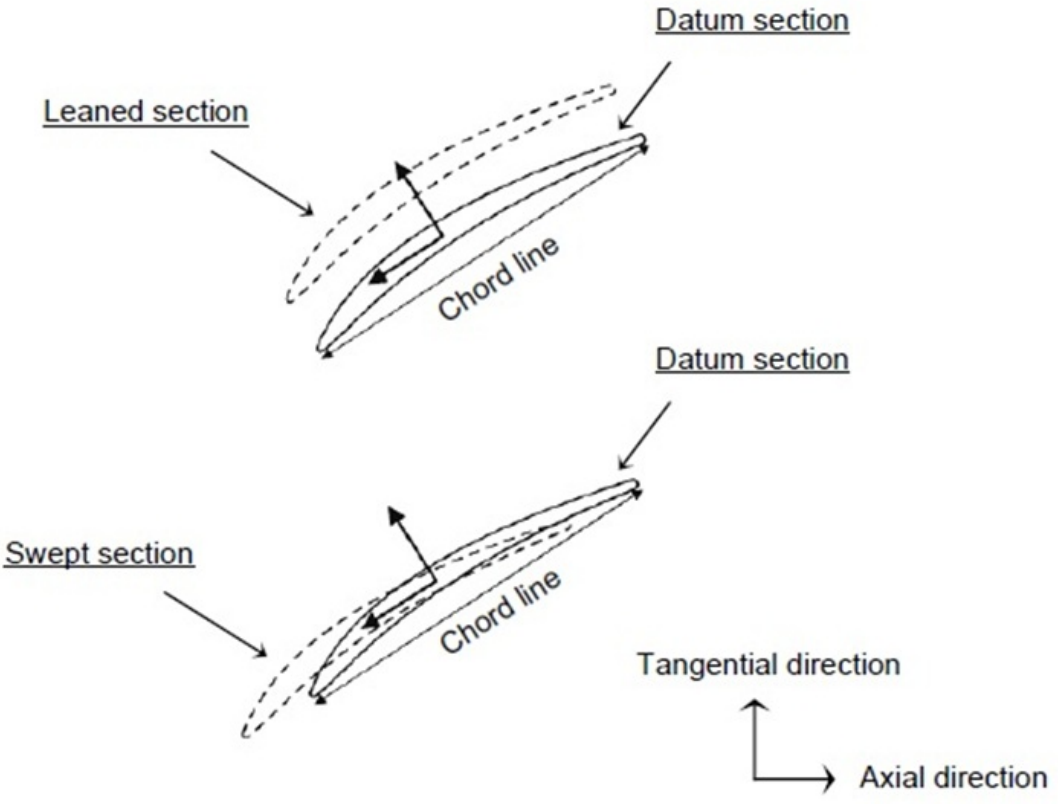


**Figure 2.10:** Sweep and lean definition. [2]

2.10, the term of sweep is used to describe the movement of blade sections along the local chord direction. Lean is defined when the blade moves normal to the airfoil chord line. To understand the sweep and lean influence on the performance of a transonic blade, it is necessary to consider the three-dimensional shock structure.

"The shock starts from the blade leading edge and propagates into the blade passage, the application of sweep or lean modifies the spatial shape of the blade leading edge and, consequently, the spatial shape of the shock. An aft swept blade, for instance, develops an aft swept shock, at least far from the tip (at the tip endwall region the shock shape is influenced also by the presence of the casing)" [2].

"The influence of sweep on shock structures and secondary flows has been widely analyzed in the literature and it seems to be of general agreement that the forward sweep leads generally to significant benefits" [5]. Numerical and experimental analysis have been conducted by Hah et al. (1998) [3] to evaluate the performance of a conventional unswept rotor. A forward-swept rotor and an aft-swept rotor showed that the forward-swept rotor had a higher peak efficiency and a larger stall margin than the baseline unswept rotor. On the other hand, the aft-swept rotor had a similar peak efficiency with a significantly smaller stall margin. In 2002, using a CFD

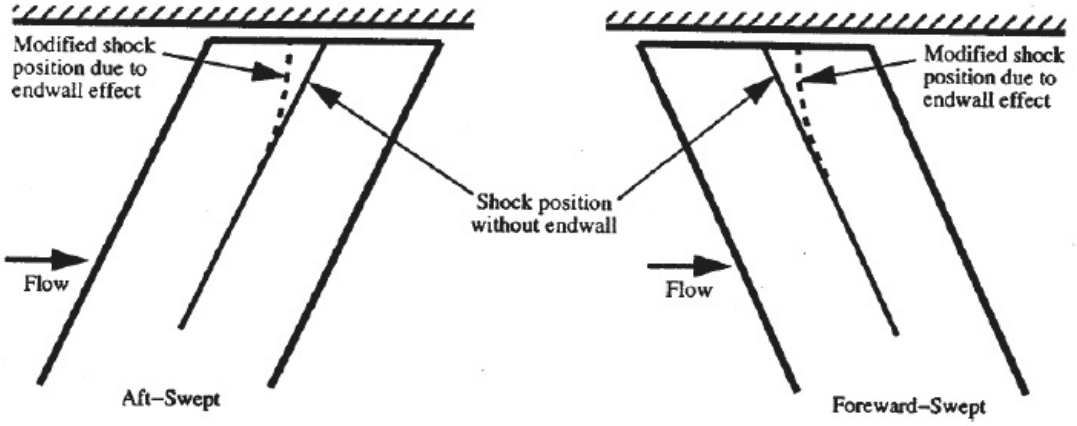


**Figure 2.11:** Endwall effect on shock structure near the casing. [3]

model, Denton and Xu [12] observed that the global effects of swept blades on transonic fan efficiency and pressure ratio are not very remarkable, but confirmed the significant improvements on compressor stability induced by forward sweep in term of larger stall margin. As said previously, the three-dimensional shock structure is one of the most important aspect to consider when the influence of sweep and lean on the performance of transonic blade row is analyzed. As described by Hah et al. [3], the shock must intersect the casing at right angles (a phenomenon known as endwall effect); this fact induces the shock to move upstream in an aft-swept rotor and downstream in a forward-swept rotor (Fig. 2.11). Usually, a shock located more downstream near the casing leads to a better stability and this is observed in forward-swept rotor.

In addition, the Fig. 2.12 shows a flow phenomenon caused by the considerable influence of sweep on the accumulation of low momentum fluid near the tip endwall region.

Yamaguchi et al. [4] found that this phenomenon is of lesser importance in forward-swept rotor than in conventional radial rotor blades. The reason can be associated to a redistribution of pressure field around the blade, which contrasts the radial migration of boundary layer fluid particles. “Moreover, as observed by Denton and Xu [12], the sweep influences the loading on the blade near the walls; in particular, the forward sweep can reduce the blade loading in front of the tip region, where the loading rapidly falls down to zero (no blade) as one moves radially from the tip to a lower span” [5] (Fig. 2.13). This helps to reduce the sensitivity to changes in incidence and the intensity of the tip leakage flows in this area. The influence of lean in transonic compressor rotors is not extensively described in the literature, but it seems - as observed by Bergner et al. in 2002 [13] - that the use

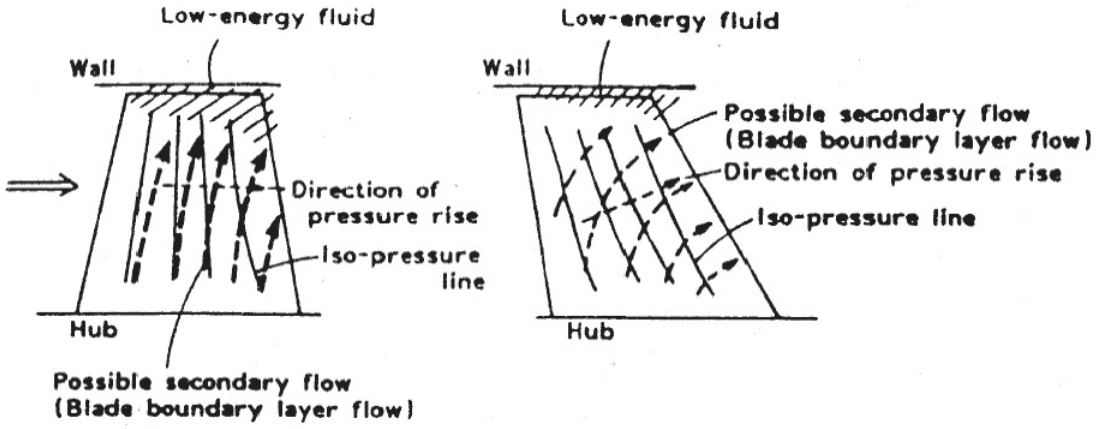


**Figure 2.12:** Impact of swept on radial migration of boundary layer fluid particles on subsonic compressor rotor. [4]

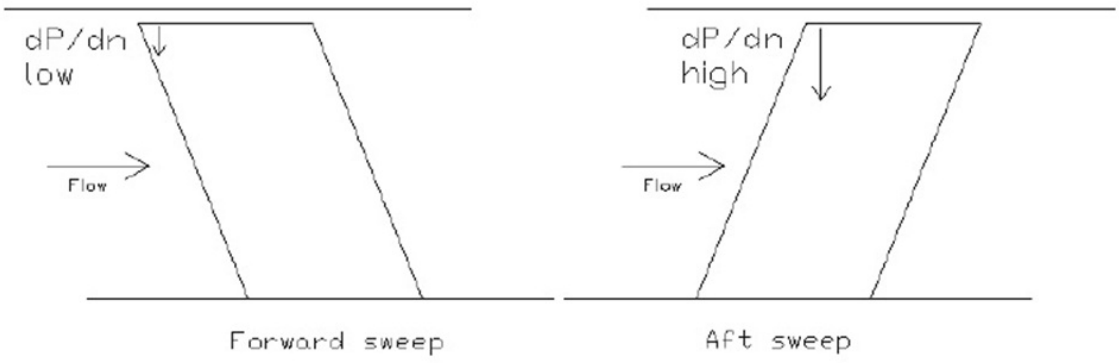


**Figure 2.13:** Impact of sweep on blade loading in the front area near the casing. [5]

of lean can give rise to a significant change in the shock pattern. Recently, Benini (2004) [14] performed a multi-objective design optimization on the NASA Rotor 37, and he demonstrated that the overall efficiency can be significantly improved by giving the blade a proper lean toward the direction of rotation, due to a drastic modification in the shock structure within the blade passage.

## 2.2 NASA rotor 67

NASA Rotor 67 is a rotor with a low-aspect-ratio, and it is the first-stage rotor of a two-stage fan (Fig. 2.14).

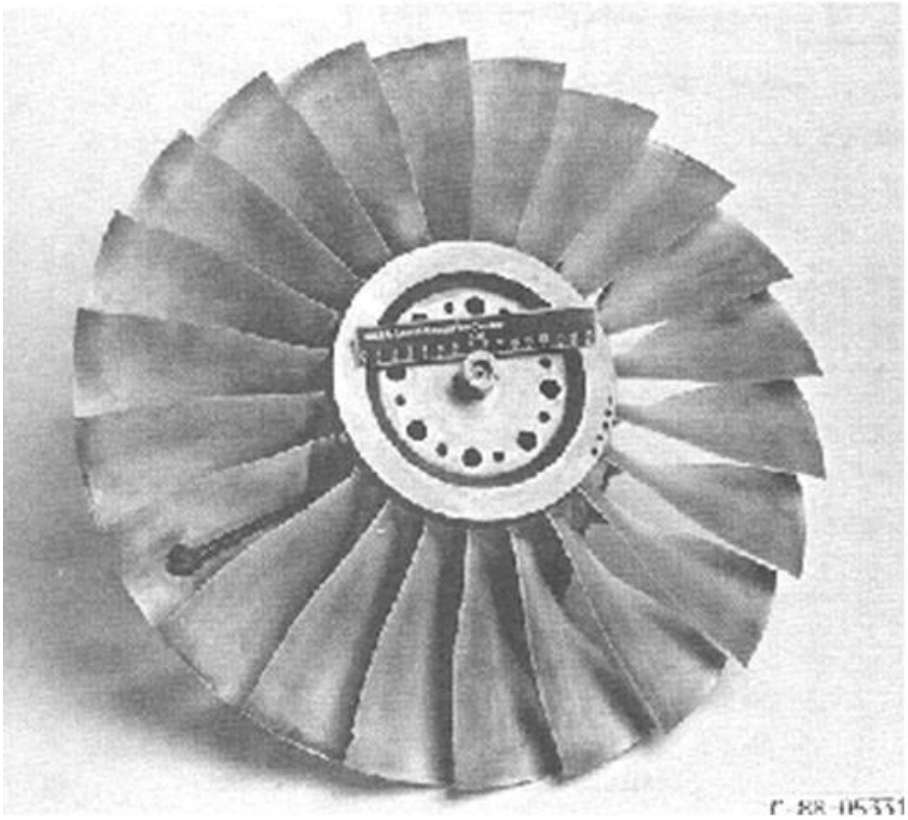

**Figure 2.14:** NASA Rotor 67.

The Fig. 2.15 shows the diagram of the inlet and outlet velocity vector at the design condition at 10-percent span. The design pressure ratio is 1.63 with a mass flow of 33.25 kg/s. The design rotational speed is 16043 rpm, which yields a tip speed of 429 m/s and an inlet tip relative Mach number of 1.38. The rotor has 22 blades and an aspect ratio of 1.56 (based on average span/root axial chord). The rotor solidity varies from 3.11 at the hub to 1.29 at the tip. The inlet and exit tip diameters are respectively 51.4 and 4805 cm. The ratio between the hub and the tip

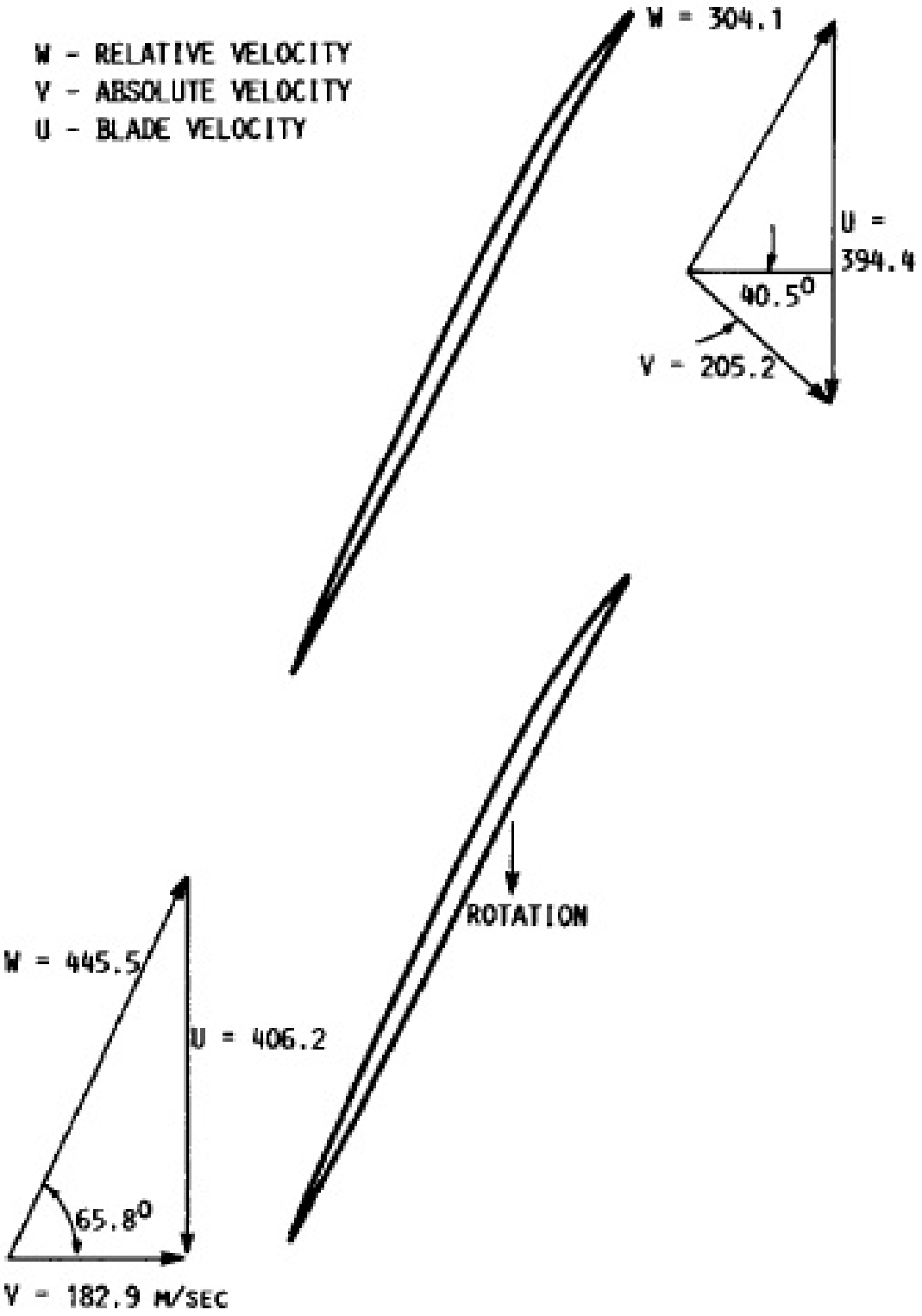


**Figure 2.15:** Velocity diagrams at design conditions at 10-percent span from tip.

radii is 0.375 at the inlet and 0.478 at the outlet. The rotor geometry under design speed operating conditions is normally determined by applying deflections calculated by the NASTRAN finite-element computer code to the blade manufacturing coordinates. The geometry derived was also corrected with the laser measurements at the blade tip.

## 2.3 Shape optimization of transonic compressor rotors

A study on NASA Rotor 37 was the first investigation to understand the impact of axially swept and tangentially leaned blades on the aerodynamic behaviour of transonic axial flow compressor rotors. "In order to model the new swept and leaned blades, the radial stacking line of Rotor 37 was modified as shown in Fig. 2.16" [5]. All the available curvatures (27 configurations for both sweep and lean, including

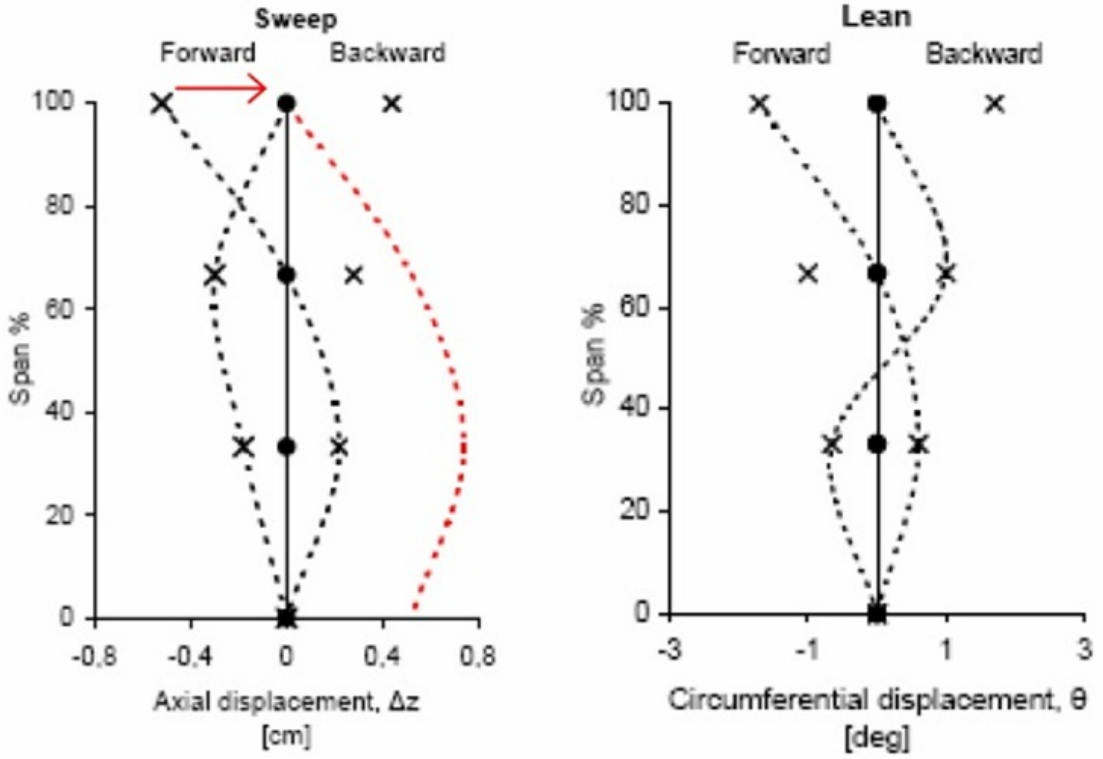


**Figure 2.16:** Swept and leaned stacking line definition. [5]

the baseline) were obtained by moving the control point (black circles) located on 33%, 67%, and 100% of the span. For all the investigated geometries, the flow field around the blade was computed using a commercial CFD code which solves the Reynolds-average Navier-Stokes equations. From this study, the backward-swept

rotors led to a slightly better performance compared to the forward-swept rotors, with a predicted efficiency that was 0.5-0.6% higher than the original Rotor 37 at the same operating conditions. The analyzed backward-swept rotor showed the possibility to obtain a considerable aft-swept shock front with a convenient meridional leading edge curvature. There was also a substantial increment in the overall efficiency (up to 1.3% higher), applying a stacking line curved toward the direction of rotation. In addition, this study demonstrated that the use of swept or leaned blades can reduce the shock losses and improve the aerodynamic behaviour of the rotor. Another accurate numerical investigation on the influence of blade stacking line curvature on the performance of a transonic axial flow compressor rotor (NASA Rotor 37) was successfully carried out by Biollo and Benini [7]. In this study, the calculated flow fields were analyzed in detail to better understand the impact of sweep and lean on the internal flow features and to realize the aerodynamic reasons for the efficiency improvements shown by the aft-swept and forward leaned rotors.

The main observations of this study are:

- compared to the baseline rotor, the forward leaned rotors and the aft-swept rotors gave a significant increment in the overall efficiency (the first one showed the higher increments).

- The blade curvature impacted on the shock structure. Sweep can influence the shock shape in the meridional plane, inducing the shock to assume the meridional curvature of the blade leading edge. On the other hand, lean seems to helpful to change the blade-to-blade shock shape, inducing the shock to move downstream when the blade is curved towards the direction of rotor rotation and slightly upstream when the blade is curved contrarily.

- Sweep had an impact on the radial outward migration of fluid particles which takes place inside the blade suction side boundary layer after the interaction with the shock.

- The higher efficiency shown by the aft-swept rotors can be associated with the reduction of the secondary flow mentioned in the previous point. This phenomenon obstructs the boundary layer development in the streamwise direction, leading to a thickening of blade wakes. A reduction of its strength helps to reduce the entropy generation and the aerodynamic losses associated with the blade wake development.

- The change in the shock structure induced by lean can be associated with a change in the flow pattern near the pressure side of the blade leading edge.

Lean induces the flow to move radially inward when the blade is curved towards the direction of rotor rotation and radially outward when the blade is contrarily curved.

- The higher efficiency induced by forward lean can be associated with a more favourable 3D shock structure at the outer span (where the shock strength reaches its maximum value). All the forward leaned rotors gave a shock front more oblique to the incoming flow in the peripheral region. This effect reduces the aerodynamic shock losses and entropy generation, with a positive impact on the overall rotor efficiency.

## 2.4 Geometrical parameterization

A good geometrical parameterization using curve methodologies is important when a shape optimization has to be made. It is important to choose a methodology that allows to have:

- a low number of parameters necessary to reproduce adequately the original curve;
- enough degrees of freedom to allow the optimization algorithm to generate a wide range of different shapes (explore the solution space).

The choice is a dichotomic problem because a large number of parameters implies a wide range of possible shapes, but also a huge number of degrees of freedom. A large number of DOF means that the computational power and the time resources that the optimization algorithm needs are massive. On the other hand, a low number of parameters permits to reduce the necessary computational resources, but it reduces the optimization ability to find the optimal shape. The most common curve parameterization methodologies are: classical polynomials, spline, Bezier curves and B-spline. In this section, only the Bezier curves method is described because it is the geometrical representation used in this thesis.

### 2.4.1 Bezier curves

Historically speaking, the Bezier curves became popular around the 1962 thanks to Pierre Bezier. He was a French engineer that worked for Renault, and he used these curves to design automobile bodies. Bezier used this representation on his Computer-aided Design (CAD) studies; in fact, Bezier curve is nowadays used in PostScript language and in some of the vector graphical program. Every polynomial

curve segment can be represented by its Bezier polygon. They are closely related and "have common end points and tangents, the curve segment lies in the convex hull of its Bezier polygon, etc" [6]. A $n$th degree Bezier representation is described by:

$$b(t) = \sum_{i=0}^{n} c_i B_i^n(t) \tag{2.1}$$

where $C_i$ are the coordinates of control points, $t \in [0, 1]$, and $B_i^n(t)$ are the polynomial coefficients. For a 2D problem the Eq. 2.1 becomes:

$$\left\{ \begin{array}{c} x(t) \\ y(t) \end{array} \right\} = \sum_{i=0}^{n} B_{n,i} t^i (1-t)^{n-1} \left\{ \begin{array}{c} x_{cp,i} \\ y_{cp,i} \end{array} \right\} \tag{2.2}$$

where the binomial coefficient are:

$$B_i^n = \frac{n!}{i!(n-1)!} \tag{2.3}$$

The characteristics of Bezier curves are:

- they does not get over the control points (except for the first and the last point);
- the line joining the first and the second point is tangent to the curve on the initial point; similarly the line joining the last and the second last point is tangent to the curve on the last point.

In Fig. 2.17 is shown an example of the use of Bezier curves for an aerodynamic airfoil.

## 2.5 Optimization algorithms

### 2.5.1 Definition of optimization problem

A typical engineering optimization problem consists to improve the performances and the characteristics of an existing design. For example, it is possible to optimize the shape of an airplane to reduce weight, or to find the flight path that leads to the less fuel consumption. The optimization algorithms have a strong mathematical and statistical background. It is necessary to subdivide the optimization problems into single-objective problems and multi-objective problems, depending on the number of objectives that need to be minimized or maximized. The single-objective problem is when only one objective needs to be minimized or maximized; the multi-objective

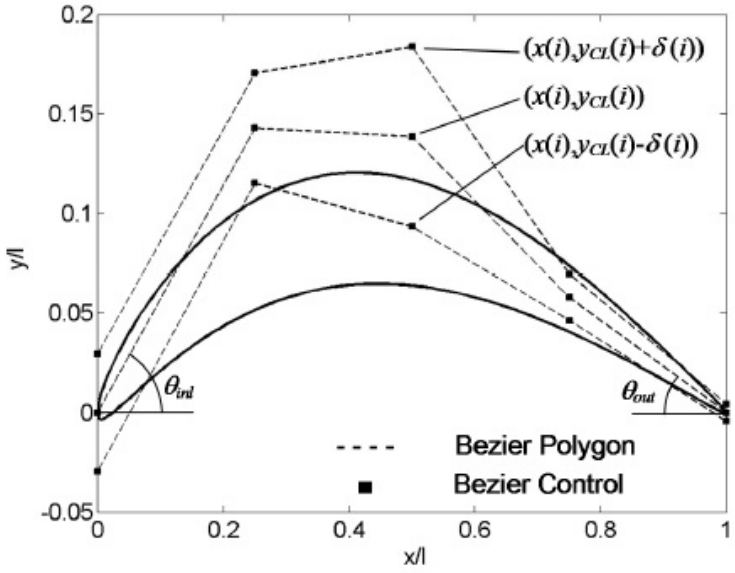


**Figure 2.17:** Bezier curves for an aerodynamic airfoil. [6]

problem is when more objectives need to be minimized or maximized. It is clear that a single-objective problem is a particular case of a multi-objective problem. Another subdivision to do is:

- Constrained Problems: the decision variables space is constrained;
- Unconstrained Problems: the decision variables space has not constrain.

Hence, the unconstrained problem can be considered as a special case of the constrained problem.

### 2.5.2 Optimization methods

It is possible to group the optimization methods depending on the order of derivatives of the objective function used: there are zero, first and second order methods.

#### Zero order methods

The zero order methods fall into the category of not-deterministic (stochastic) optimization methods. In fact, "for identical problems and identical starting conditions, the evolution of the solution will not follow the same path on repeated applications" [15]. Zero order methods include:

**Random Search** the simplest way to minimize an objective function is to create randomly a large number of candidate vectors and evaluate the objective for each of them.

**Random Walk** a variation of random search. In this method the new decision variables are based on a random perturbation of the previous design.

**Simulated Annealing** is based on the analogy of the simulation of the annealing solids. "In material science, annealing denotes a physical process in which a solid is heated up to a maximum temperature value at which all particles of the solid randomly move in the liquid phase, followed by a slow cooling of the heat bath. In this way, all particles arrange themselves in the low energy ground state of the solid lattice, provided that the cooling is carried out sufficiently slowly" [16].

**Evolutionary Algorithms** "they are based on Darwinian evolution, whereby populations of individuals evolve over a search space and adapt to the environment by the use of different mechanisms such as mutation,crossover and selection. Individuals with higher fitness have more chance to survive and/or get reproduced" [16]. This method is described better in the next section.

### First order methods

First order methods use gradient information and are therefore usually more efficient than zero-order methods, but the higher efficiency comes at price of higher computational cost to compute the gradient. These methods are not the most suitable for aerodynamic optimization problems. They have been used for optimization problems before the development of evolutionary algorithms. Today they are used for simple single-objective optimization problems, where the efficiency of these methods plays an important role. Moreover, another drawback of these methods is that they cannot be used for the multi-objective problems.

### Second order methods

Second order methods have the advantage that only one iteration is needed to minimize a quadratic function. For a non-quadratic function, some more iterations are needed, but the convergence is faster than any first order method. As the first order methods, second order methods cannot be used for multi-objective optimization problems. Second order methods include:

**Newton method** is one of the most famous and common second order optimization method. It is based on the local quadratic approximation of the objective function. The advantages of this method are: a reduction of iteration number required, only one iteration is required if the function is quadratic, and the

capability to find the minimum also for non-quadratic functions without the risk of local minimum or inflection point convergence.

**Quasi Newton method** uses the information of previous iteration to estimate the Hessian matrix. The description of this method is heavy, and it requires a large use of vector algebra theorems.

## 2.6 Genetic algorithm

The Genetic Algorithm (GA) is the most popular evolutionary method, and it is one of the most suitable methodology for aerodynamic optimization problems because:

- "do not require the computation of gradient and can tolerate even more approximate or noisy design objective evaluation" [17];
- "can be efficiently parallelized and can take full advantage of the massively parallel computer architecture" [17];
- "can directly approach to a multi-objective optimization problems" [17].

Genetic Algorithms are based on the mechanisms of natural selection, and they use the survival of the fittest to obtain the optimum. A population consists of a fixed number of individuals, and each one is represented by a binary string, containing all values of parameters (the analogy can be made with living creatures where the binary string is their chromosomes). In Fig. 2.18 is shown the reproduction mechanism used by GA. Roughly speaking, a starting population is created and its genetic material is manipulated by a reproduction mechanism (Fig. 2.18). The result of reproduction is new individuals that compose the new generation. These individuals are in competition, and who adapt better to the environment, have more chance to survive and to hand down their gene pool. The population evolves from generation to generation, increasing the average fitness of the individuals.

### 2.6.1 Binary string

In GA, each individual is usually represented by a binary string. The number of bits per parameters depends on the required accuracy to represent the parameter. Hence, a value $x \quad (x^l < x < x^u)$ can be rounded by a binary string $S = [b_q, b_{q-1}, ..., b_1, b_0]$ defined as:

$$x = x^l + \frac{x^u - x^l}{2^q - 1} \sum_{k=0}^{q} 2^k b_k \tag{2.4}$$

where $b_i$ is 0 or 1 and $q$ is the number of bits used for the encoding.

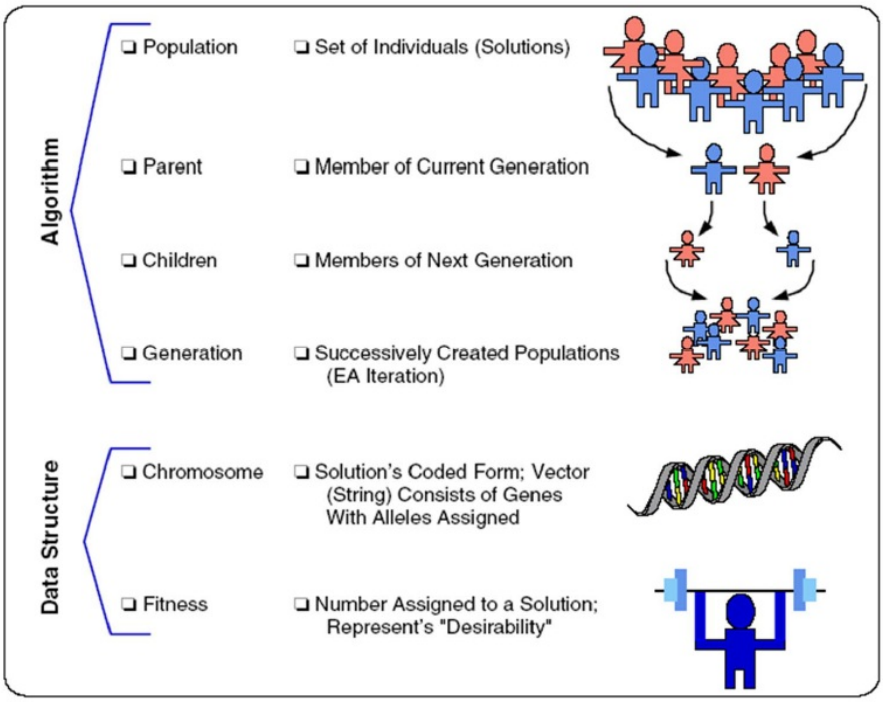


**Figure 2.18:** GA reproduction mechanism.

### 2.6.2 GA operators

GAs use three operators in the reproducing process:

- Selection
- Reproduction
- Genetic Mutation

#### Selection

The Selection operator chooses the individuals depending on the strength of their fitness value. The most common selection methods are: tournament selection and roulette wheel selection. In a *tournament selection*, $s$ individuals are chosen randomly from the population, and the best among them is selected as the first parent.

The second parent is selected in the same way. The parameters $s$ is called *tournament size*. Large values of $s$ result in a more elitist selection, while a low values allow less fit parents to be selected and result in a more diverse population. Therefore, the s choice influences the exploration and the exploitation capability of the algorithm. In [18] is proposed to use $s = 2$.

As an alternative, a *roulette wheel selection* can be used. As shown in Fig. 2.19, the number of parts of the circle represents the number of individuals, and the size

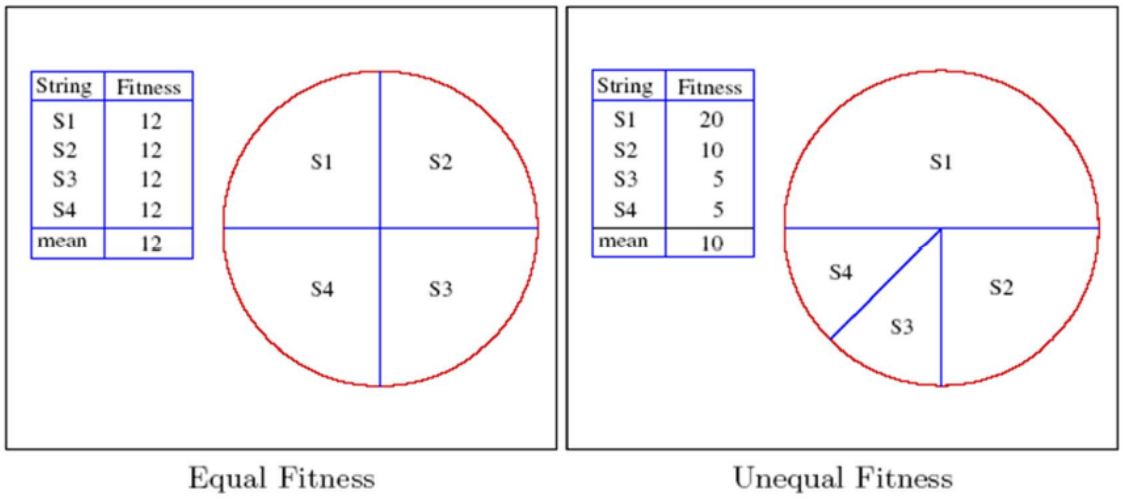


**Figure 2.19:** Roulette method of selection.

of each part symbolizes the fitness of each individual. Hence, the probability to choose one individual is directly proportional to his fitness value.

### Reproduction

The Reproduction operator mixes the parent genes. A fundamental operator is the *crossover* that consists of a random counter that chooses a random point in the binary string. At this random point (breaking point), the two strings of the two individuals are broken, and the two parts are exchanged, as shown in Fig. 2.20.

### Genetic mutation

The Genetic Mutation changes an element of the chromosome (0 becomes 1 and vice versa) at a random position (Fig. 2.21). This operation is made on a closed part of individuals of the population. The mutation is essential for the exploration of the research space. During the evolutionary process, it is possible that the best individual is lost by mutation or crossover. Hence, most genetic algorithms use the elitism strategy to prevent this loss of valuable information for the evolution. In case the best individual of the new generation is worse than that of the previous generation, the latter one will replace a randomly selected individual of the new generation. In this way, the best individual prevails or can be replaced by a better one.

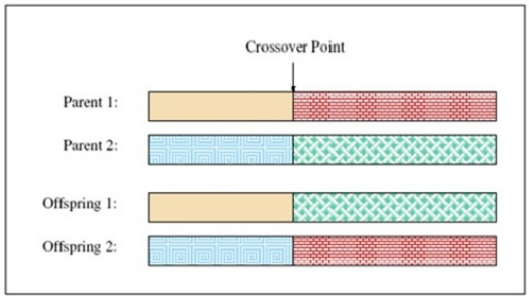


(Parent 1) $\mathbf{X}_1 = \{0\ 1\ 0 \mid 1\ 0\ 1\ 1\ 0\ 1\ 1\}$

(Parent 2) $\mathbf{X}_2 = \{1\ 0\ 0 \mid 0\ 1\ 1\ 1\ 1\ 0\ 0\}$

(Offspring 1) $\mathbf{X}_3 = \{0\ 1\ 0 \mid 0\ 1\ 1\ 1\ 1\ 0\ 0\}$

(Offspring 2) $\mathbf{X}_4 = \{1\ 0\ 0 \mid 1\ 0\ 1\ 1\ 0\ 1\ 1\}$

**Figure 2.20:** Crossover

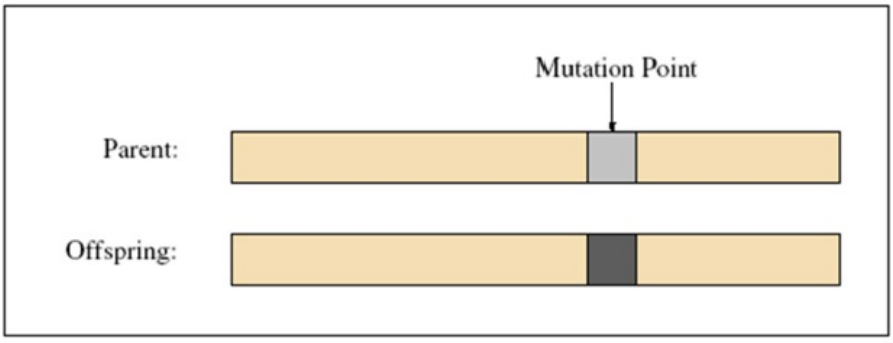


**Figure 2.21:** Genetic mutation

### 2.6.3 Pareto ranking

The Pareto ranking is one of the most common approach for multi-objective optimization problems. In a multi-objective function there is a set of solutions that are all "enough good", this means that in this group no solution is better than others. All these solutions form the Pareto front. Hence, the Pareto front is the group of non-dominated solutions. The definition of domination (Pareto criterion) is

*A solution $\vec{x}^{(1)}$ dominate a solution $\vec{x}^{(2)}$ ($\vec{x}^{(1)} \prec \vec{x}^{(2)}$) if both the following condition are met:*

- *solution $\vec{x}^{(1)}$ is not worse than $\vec{x}^{(2)}$ for all the objective functions*

$$f_j(\vec{x}^{(1)}) \leq f_j(\vec{x}^{(2)}) \quad \textit{for any} \quad j = 1 \cdots l$$

- *solution $\vec{x}^{(1)}$ is strictly better than $\vec{x}^{(2)}$ for at least one objective functions*

$$f_j(\vec{x}^{(1)}) < f_j(\vec{x}^{(2)}) \quad \textit{for at least one} \quad j \in 1 \cdots l$$

An example of Pareto front is illustrated in Fig. 2.22. Solution A is dominated by both solution B and solution C, but solutions B and C as the same rank; in fact, neither B dominates C, nor C dominates B.

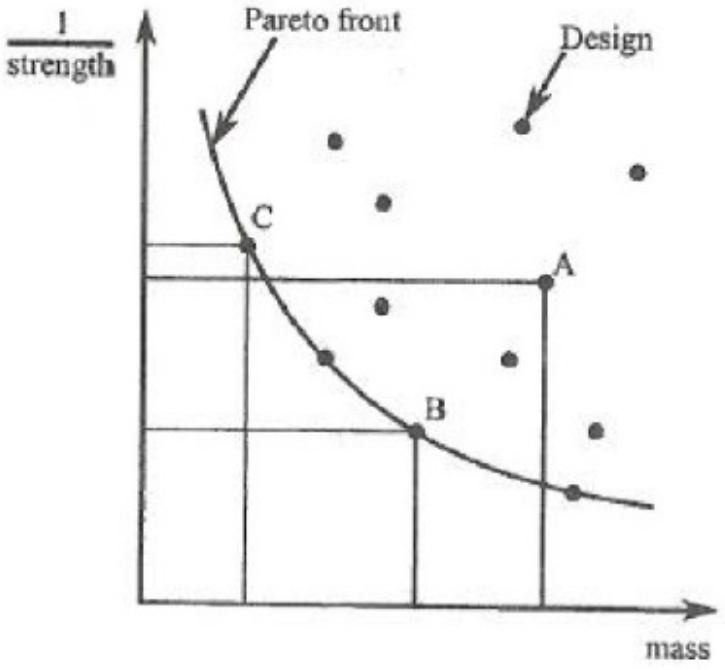


**Figure 2.22:** Pareto front [6]

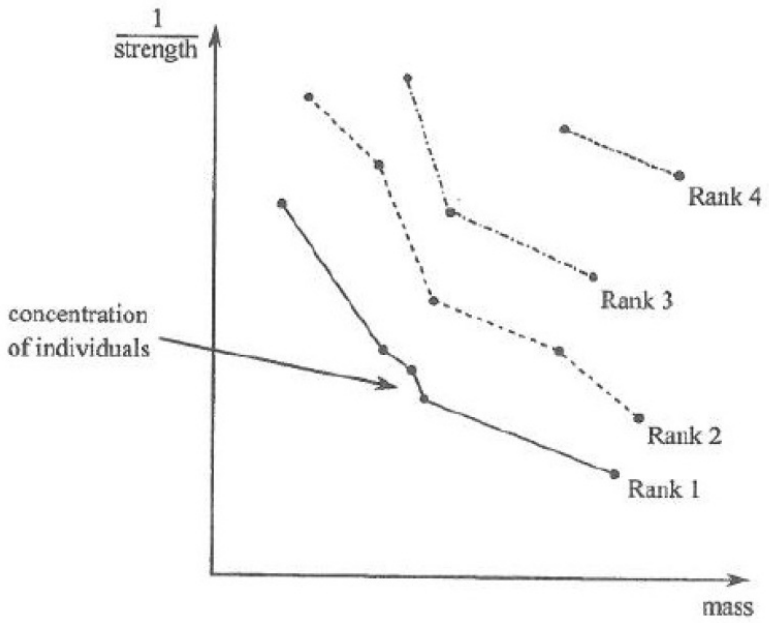


**Figure 2.23:** Pareto ranking process for a two objective optimization problem. [6]

The Pareto ranking selects first the non-dominated solutions of the entire population (Pareto rank 1). This set of individuals is removed from the population and then the selection of the non-dominated individuals is repeated on the remaining population. The resulting individuals are given the Pareto rank 2. The algorithm is repeated until the entire population is ranked (Fig. 2.23). The fitness of each individual is inversely proportional with the Pareto rank $r$, $f = 1/r$. Hence, the individuals of the first rank have the highest fitness, and they have more chance to be reproduced while higher ranks have a lower fitness. The target is to produce an offspring that dominates the individuals of the current Pareto front rank 1. However, some restrictions on the reproduction may be needed to prevent a concentration of individuals on some parts of the Pareto front.

## 2.7 Advanced GA

### 2.7.1 Distributed GA

The Distributed Evolutionary Algorithm is one way to accelerate the GA, and to improve the evolution. The population is divided into islands which evolve in isolation. The most promising individuals are exchanged between islands. Hence, "distributes GAs outperform conventional GAs in term of total number of evaluations" [19] [20].

This approach is suitable for parallel computing because each island is computed by a single processor or a single solver node. "The main idea is the use of small size

of interconnected sub-populations instead of a single large population; these sub-populations evolve independently on each node for a time or period called an epoch. After each epoch a period of migration and information is exchanged between nodes and successive new periods of isolation occur" [15].

### 2.7.2 Hierarchical GA

The hierarchical GA is another way to accelerate the GA by using a low fidelity model. The objective function is evaluated by using less accurate tools, which can be achieved by reducing the number of grid points or by reducing the complexity of the analysis. These models are computationally less expensive but have a lower efficiency. Each promising individual based on the low fidelity optimization needs to be reevaluated by the high fidelity model. However, the total computational effort decreases in search towards the optimum. The distributed GA is often used to implement the hierarchical GA: the evolution takes place on isolated islands, for which some use the high fidelity model and others the low fidelity model. The individuals who go from low fidelity islands to high fidelity islands must be reevaluated with the high fidelity model. An example of hierarchical GA topology is illustrated in Fig. 2.24. The bottom layer can be entirely devoted to exploration, the intermedi-

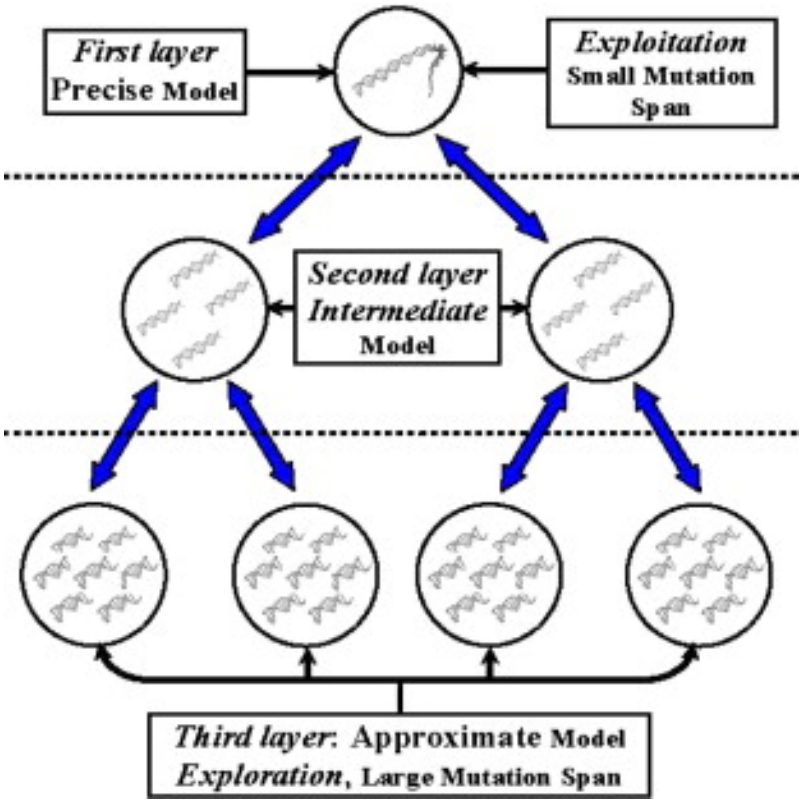


**Figure 2.24:** Hierarchical GA topology.

ate layer is a compromise between exploitation and exploration and the top layer concentrates on refining solutions. The main feature is the interaction between the given layers. The best solution progresses from the bottom layer to the top layer where it is refined. Hence:

- the top layer concentrates on refining solutions, that can be achieved by tuning the GA in a way that takes very small steps between successive crossover and mutation operations;
- the intermediate layer is a compromise between exploitation and exploration;
- the bottom layer can be entirely devoted to exploration, that means that the GA can make large leaps in the search space.

All the bottom layers can use a less accurate fast model to compute the fitness function of the individuals of the sub-population. Even though these solutions may be evaluated rather roughly, the hierarchical topology allows to use them. These solutions are sent up to the intermediate layer during the migration phase and they are reevaluated using a more precise model to give a more accurate representation of the actual quality of the solution. The process is repeated again by sending the solution up to the top layer during the migration process. These solutions are reevaluated with a more precise model that gives a genuinely accurate value for the fitness function. Making a comparison between traditional GA and hierarchical GA, it has shown that hierarchical GA can speed up an optimization process by a factor three.

### 2.7.3 Metamodel assisted GA

"The Metamodel Assisted Evolutionary Algorithm is another way to reduce the total computational cost by using an even less accurate model, not based on a physical model, but on an interpolation of already analyzed individuals by higher fidelity models" [21]. The metamodel performs the same task as the high fidelity model, but at a very low computational cost. However, it is less accurate, especially for an evaluation far away from the already analyzed points in the design space. The first technique to implement the metamodels consists to use the metamodel for interpolations close to existing design. During each generation of the evolutionary process, the metamodel and accurate tool are used together. Another implementation consists in using the metamodel on all individuals and reevaluate the most promising ones by accurate tool. This technique is called "on-line trained metamodel", because the metamodel needs to be trained during the GA process. Another technique, called

"off-line trained metamodel", uses the metamodel as an evaluation tool during the entire evolutionary process. After several generations the evolution is stopped and the best individual is analyzed by the expensive tool. The difference between the predicted value of the metamodel and the high fidelity tool is a direct measure for the accuracy of the metamodel. One of the most common tool used to build a metamodel in the optimization loop is the neural network; there are several studies on NN implementation.

# Chapter 3

# Methodology

## 3.1 Introduction

The aim of this study, as described in Chap. 1, is to carry out an optimization of a transonic rotor blade. The optimization targets are to maximize the isentropic efficiency and the pressure ratio. In particular two different studies have been done:

- optimization of the blade tip;
- optimization of the whole blade.

In this way, it is possible to assess the influence of the tip on the performances of the blade. As described in Sect. 2.1.2, the most detrimental region in transonic compressor rotors is the tip endwall region where the tip gap region develops intense secondary flows. Hence, the study of the tip region allows to see how the change of the shape of the tip can influence the flow, especially the secondary flow.

## 3.2 Optimization strategy

The geometry (Fig. 3.2) is provided by 14 sections, and each section is defined by 260 points in cylindrical coordinates (Fig. 3.3).

From an optimization point of view, the geometry is modified by moving the blade sections in the circumferential plane. This means that the sections of the new geometry have the same r-coordinates and z-coordinates as original geometry; the new theta-coordinate is defined as:

$$\theta_{new} = \theta_{in} + \Delta\theta \tag{3.1}$$

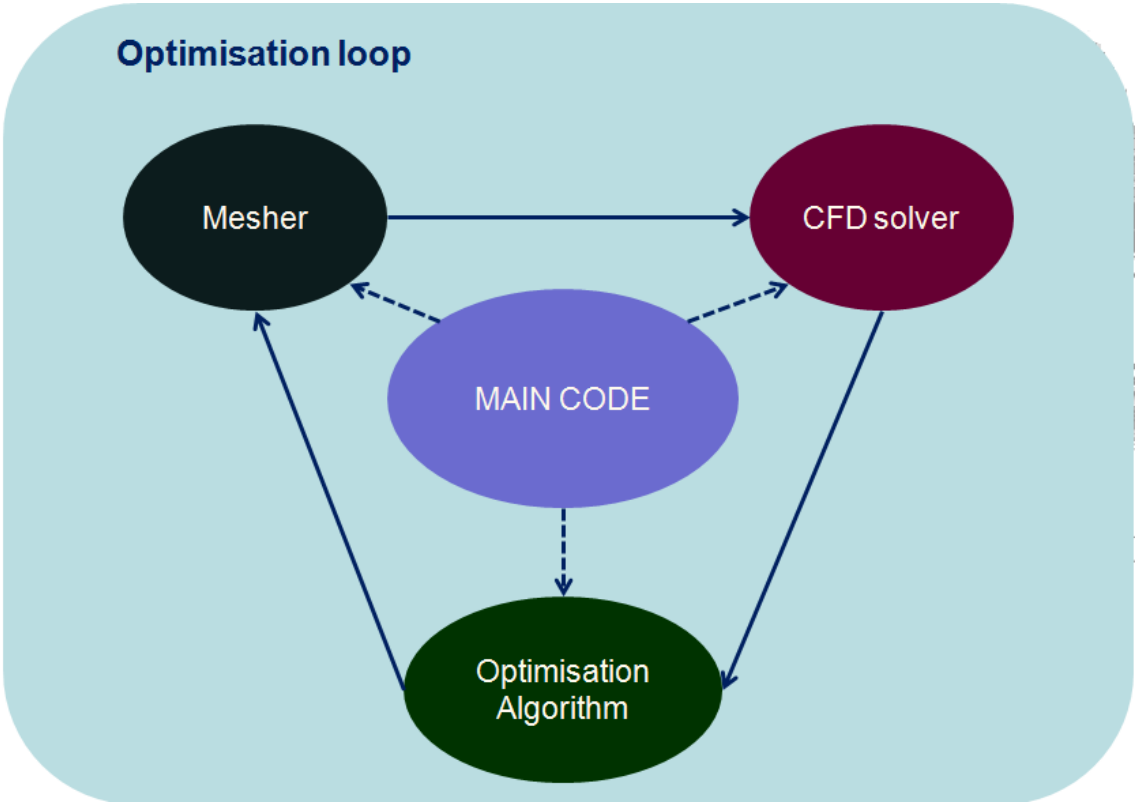


**Figure 3.1:** Optimization loop

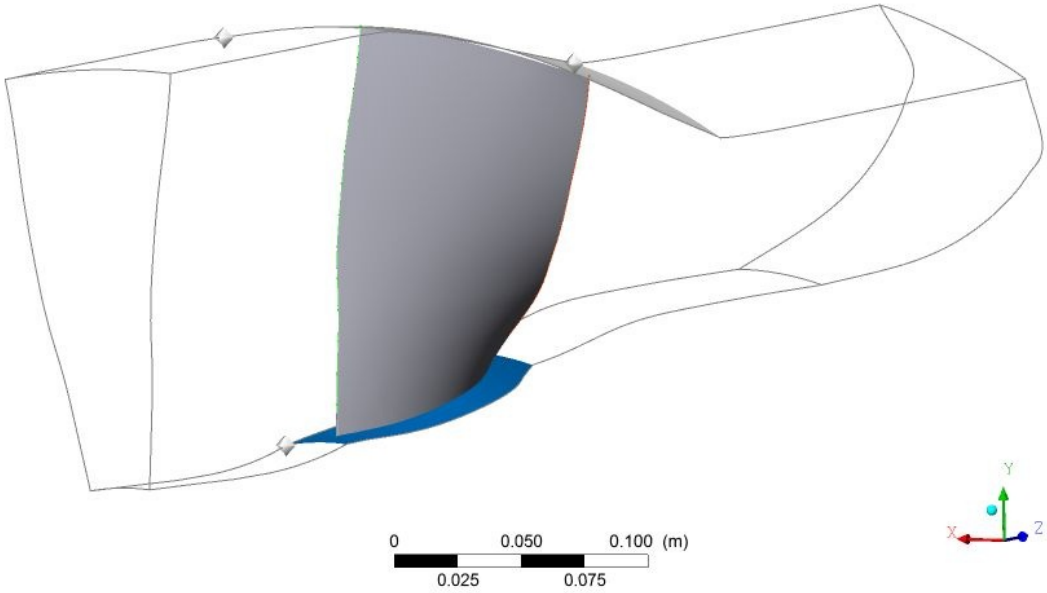


**Figure 3.2:** Geometry blade Rotor 67

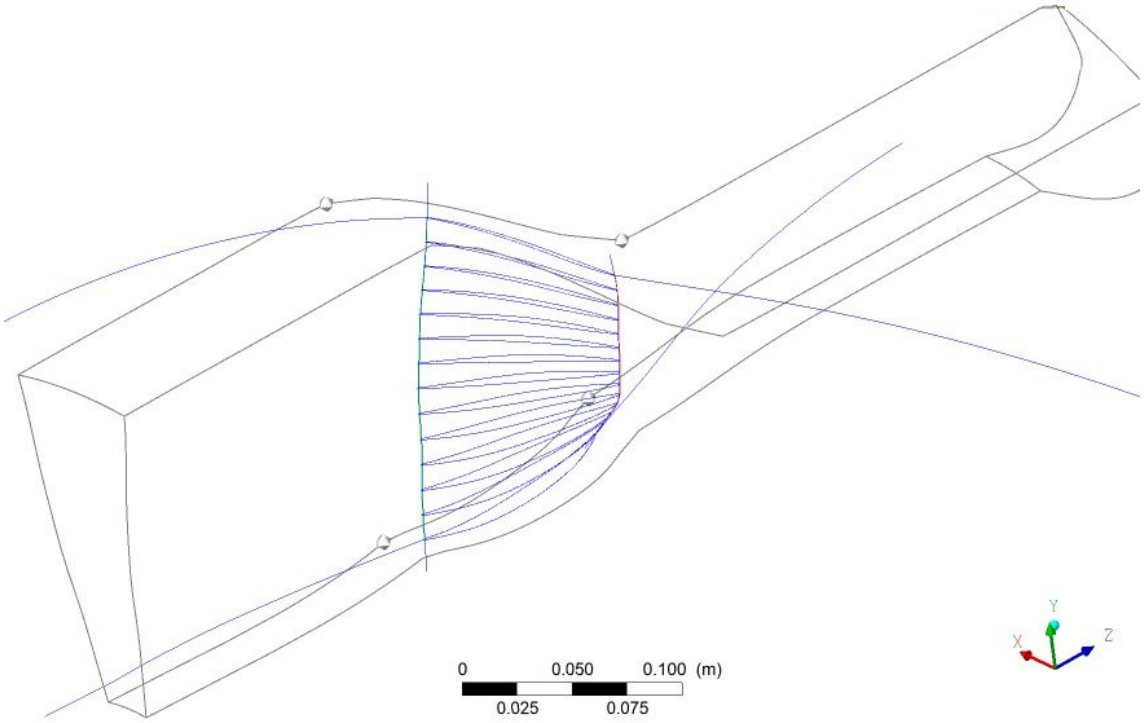


**Figure 3.3:** Blade sections

where $\theta_{in}$ is the theta-coordinate of the original geometry, and $\Delta\theta$ is the increase of displacement.

As there are 14 sections, the definition of an independent $\Delta\theta$ for each section would have implied 14 optimization coefficients. A similar CFD optimization process is impossible to carry out with the computational power available.

In addition, the blade shape is usually smooth, this means that is impossible to have a large difference between the theta-coordinates of two close sections. These two aspects have led to find a strategy that allow to obtain smooth geometry with a relatively low number of degrees of freedom. In particular, the parameterization of the $\Delta\theta$ has been defined by using Bezier curves, because it is possible to obtain different trend of $\Delta\theta$ with a reduced number of degrees of freedom. For both optimization of the tip and of the whole blade, a condition on the $\Delta\theta$ of the two last sections of the blade has been imposed. The displacement angles of the control point at 95% and 100% of the span must be both positive or both negative, and also the $\Delta\theta$ at 100% of the span must be major than the $\Delta\theta$ at 95% of the span.

### 3.2.1 Optimization of the blade tip

For the optimization of the blade tip, only the last two sections have been moved, respectively at 95% and 100% of the span. Hence, the two angles $\Delta\theta$ of the sections considered have been chosen as the optimization coefficients. As described in Eq. 3.1, the $\Delta\theta$ increase must be add to the theta-coordinates of the old geometry to give the theta-coordinates of the new geometry. For the displacement of the two points of the tip, the $\Delta\theta$ limits have been imposed, beyond which the simulation trends to diverge. The $\Delta\theta$ limits are $\pm 1°$ for the point at 95% of the span and $\pm 2°$ for the last point at 100% of the span.

### 3.2.2 Optimization of the whole blade

In the optimization of the whole blade, all the sections of the blade have to been moved. As described in Sect. 3.2, Bezier curves are used to obtain different trend of $\Delta\theta$ with a reduced number of degrees of freedom. Hence, a Bezier curve with four control points (on 0%, 33%, 66%, 90% of the span) has been built to define the $\Delta\theta$ of the section 1 until the section 12 of the blade. If four control points have been considered, there are four binomial coefficients:

$$\begin{aligned} C_0 &= 1 \\ C_1 &= 3 \\ C_2 &= 3 \\ C_3 &= 1 \end{aligned}$$

and the equation for the Bezied curve is:

$$\left\{ \begin{array}{c} x(t) \\ y(t) \end{array} \right\} = \sum_{i=0}^{3} C_{n,i} t^i (1-t)^{n-1} \left\{ \begin{array}{c} x_{cp,i} \\ y_{cp,i} \end{array} \right\} \tag{3.2}$$

where $x_{cp,i}$ and $y_{cp,i}$ are the control point coordinates.

The x-coordinates represents the sections of the blade, hence they are fixed. The y-coordinates represents the $\Delta\theta$. The optimization coefficients $\Delta\theta$ of the last two sections (tip region) have been kept independent. Hence, six optimization coefficients have been used for the optimization of the whole blade. Similarly to the optimization of the tip, some $\Delta\theta$ limits have been imposed for the displacement of the control points. The $\Delta\theta$ limits are: $\pm 0.5°$, $\pm 1°$, $\pm 1.5°$ for the control points respectively at 33%, 66% and 90% of the span. The two control points of the tip are bound to the position of the control point at 90% of the span. Hence, the $\Delta\theta$

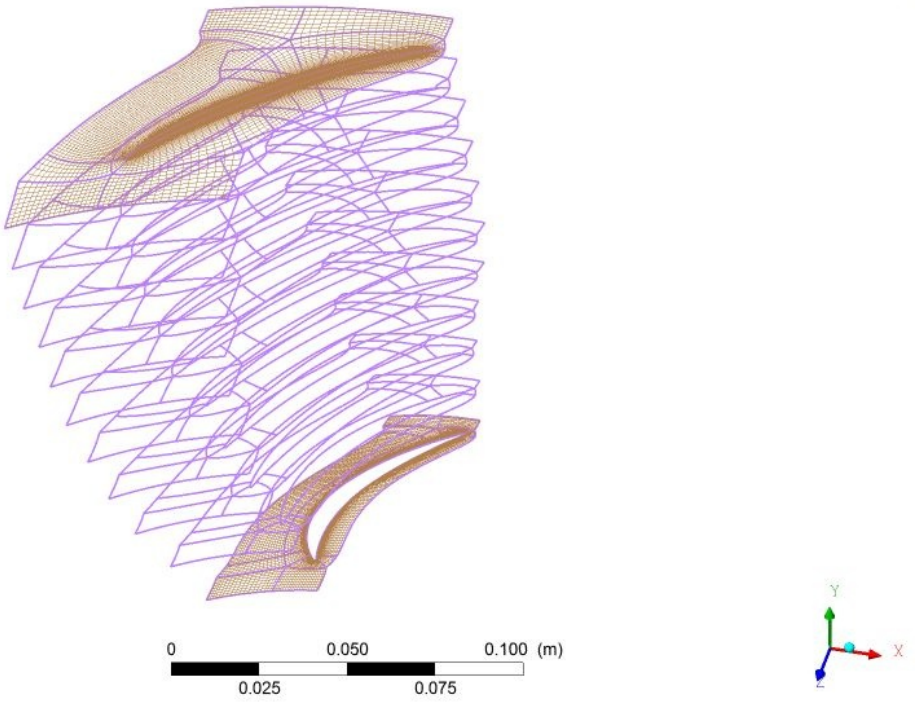


**Figure 3.4:** Layers

limits for these two points are ±1° and ±2° - as described in Sect. 3.2.1 - but these limits are referred to the control point at 90% of the span.

## 3.3 Mesh

The mesh creation is one of the most important phase of a CFD simulation. A bad mesh can strongly affect the results. The mesher code used in this study is Turbogrid, and the settings to create the mesh have been given by a previous study where the mesh was validated. The stage is composed by 22 blades. Each blade has a tip clearance at shroud of 0.1016 cm. The coordinates are cylindrical with radian as angle units and cm as length units. The three files .curve (hub.curve, shroud.curve and blade.curve) have been used to create the geometry. The topology set is created with the Automatic Topology and Meshing (ATM Optimized). This topology type enables to create high quality meshes with minimal effort, and there is no need for control point adjustment. As the Fig. 3.4 shows, ten layers along the span have been created to reduce the distortion of the mesh. One method to control the mesh size of the boundary layer is specifying the y+ height and Reynolds number. The y+ value is connected to the height of the first cell on the walls and with the Reynolds number of the main flow. Every turbulence model has a specific

range within the y+ has to stay in order to obtain valid results from the turbulence model point of view. In particular, there are two strategies to solve the boundary layer:

- Wall Functions;
- Direct Boundary Layer Resolution.

The wall function method uses a set of polynomial equation to solve the boundary layer, it requires a y+ value higher than the direct boundary layer resolution method. Therefore, the number of cells required is lower. The main drawback is that it is not able to describe properly the boundary layer evolution in presence of shock waves.

The direct boundary layer resolution method solves the whole boundary layer, but it requires a y+ value close or lower than 1. This means a very fine mesh, and thus an high number of cells. This is why the main drawback of this method is the high computational power and high time required for the simulations. On the other hand, the advantage is the capability to obtain a high fidelity simulation of the boundary layer, even in presence of shock waves or other strong phenomena like flow recirculation. For this study, it has been decided to use the direct boundary layer resolution approach, because there is a strong interaction between the shock wave and the boundary layer.

In this study the Reynolds number is $2 \cdot 10^{-6}$ and the turbulence model selected is the k-$\omega$-Shear Stress Transport. It is decided to solve all the boundary layer, therefore the mesh has been created to obtain the y+ value less than 1. In this way, the mesh created is good for the model chosen. As shown in Fig. 3.5, 3.6, 3.7, the trend of y+ along the streamwise is falling due to the presence of the shock wave.

When all the settings are set up, the mesh has been created, and it is made of about 2 million of elements (Fig. 3.8).

## 3.4 CFD set-up

For the simulation, it has been done a 3D simulation using the software ANSYS CFX, that is divided into:

- CFX-Pre;
- CFX-Solver Manager;
- CFX-Post.

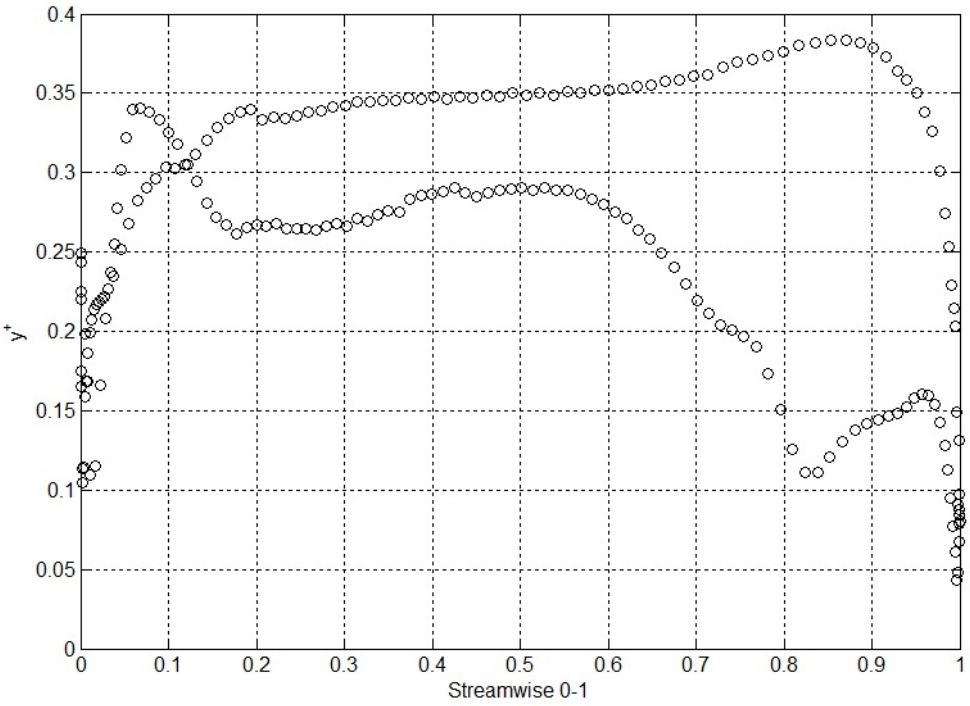


**Figure 3.5:** Trend of y+ along the streamwise at 10% of the span

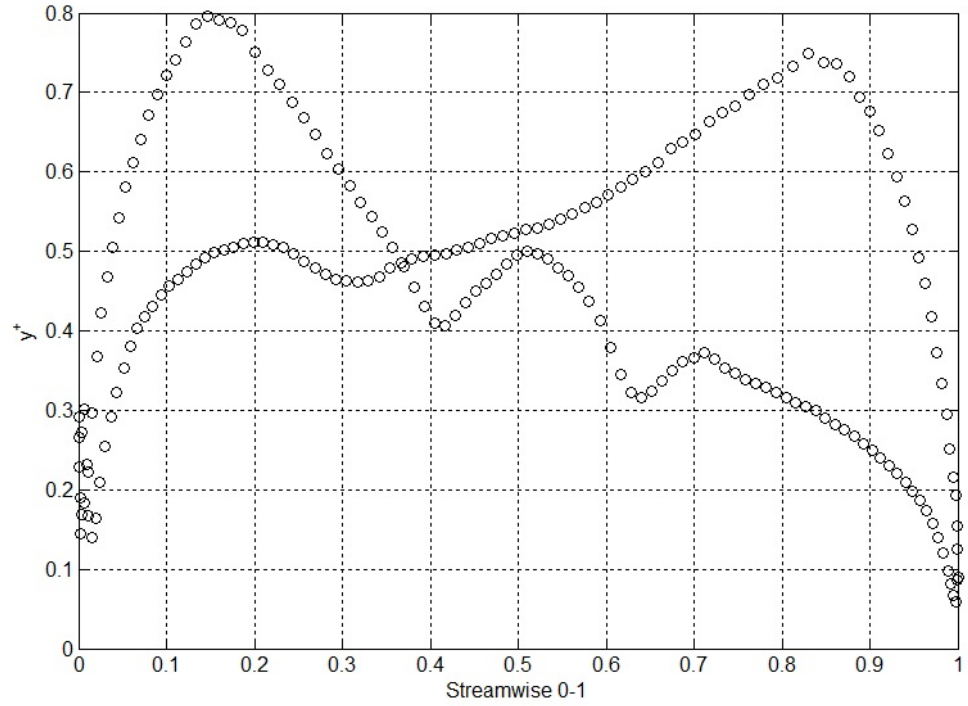


**Figure 3.6:** Trend of y+ along the streamwise at 50% of the span

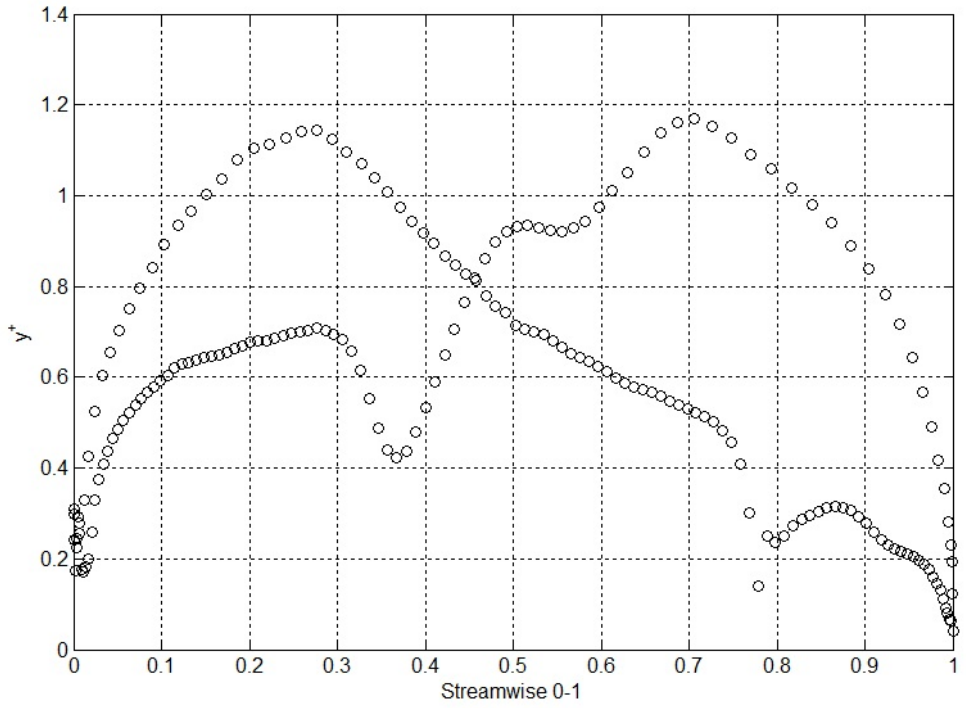


**Figure 3.7:** Trend of y+ along the streamwise at 90% of the span

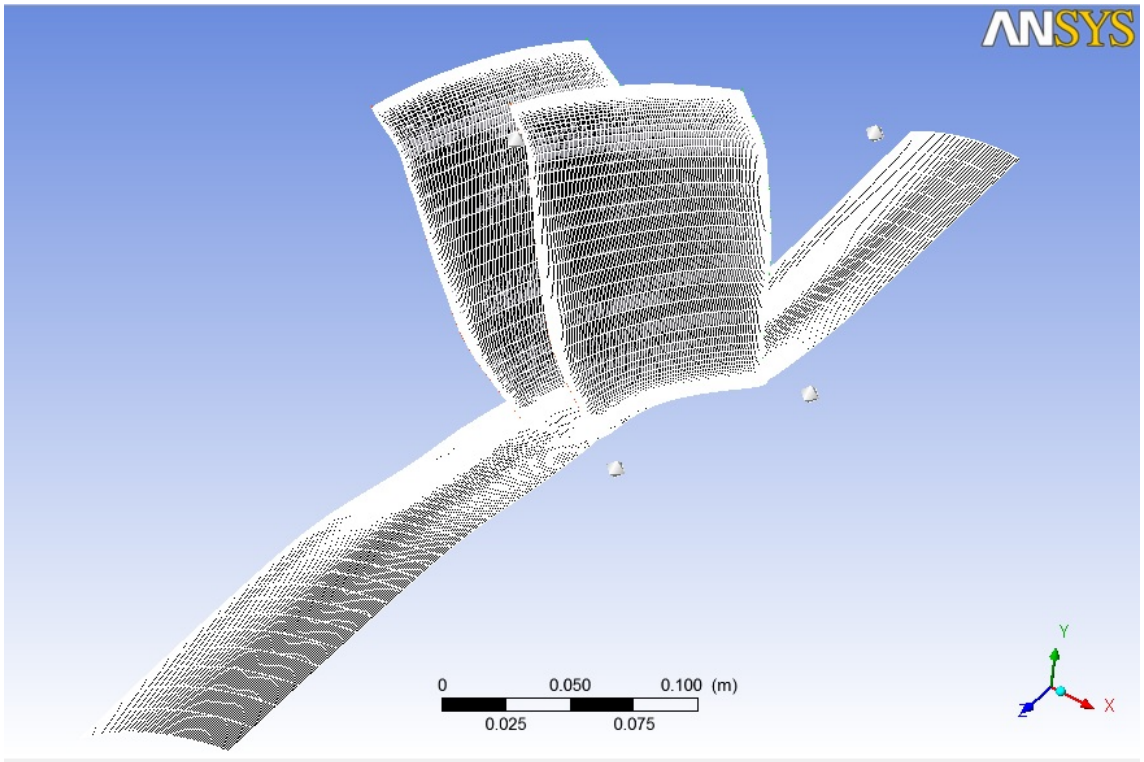


**Figure 3.8:** Mesh

### 3.4.1 CFX-Pre

CFX-Pre is the physics definition pre-processor for ANSYS CFX. The mesh produced by Turbogrid is imported into CFX-Pre, and the physical model used in the CFD simulation is selected. The setting for CFX-Pre are:

- *Basic Settings*
  - *Machine Type*: **Axial Compressor**
  - *Rotation Axis*: **z**
- *Component type R67*
  - *Type*: **Rotating**
  - *Value*: **-16043 [RPM]**
  - *Tip clearance at shroud*: **yes**
- *Physics Definition*
  - Fluid: **Air Ideal Gas**
  - Analysis Type: **Steady State**
  - Model Data:
    - Reference Pressure: **0 [atm]**
    - Heat Transfer: **Total Energy**
    - Wall Function : **Automatic, High speed (compressible) Wall Heat, Transfer Model**
    - Turbulence: **Shear Stress Transport**
  - Inflow/Outflow boundary templates: **P-total inlet P-static outlet**
  - Inflow:
    - P-total = **101325 [Pa]**
    - T-total = **288.2 [K]**
    - Flow Direction: **Normal to boundary**
  - Outflow:
    - P-static = **114500 [Pa]**
  - Solver Parameters:
    - Advection scheme: **High Resolution**

        * Convergence control: **Auto timescale**
        * Time Scale option: **Conservative**

- *Solver Control:*
    - Advection Scheme: **High Resolution**
    - Turbulence Numerics: **High Resolution**
    - Convergence Control:
        * Min. Iterations = **1**
        * Max. Iterations = **40**
    - Fluid Timescale Control:
        * Max. timescale = **1e-6**
    - Convergence Criteria:
        * Residual Type: **MAX**
        * Residual Target: **0.00001**

Hence with these settings, the rotor moves with a rotation speed of 16043 rev/min (the signal "-" is referred to the geometry). The model chosen to describe the fluid is air ideal gas because the simulation does not have high temperature values to entail changes of the gas constants (Cp and Cv). In this study, total energy is set as heat transfer model. This models the transport of enthalpy and includes kinetic energy effects. As suggested in [22], the Total Energy model should be used where the kinetic energy effects become significant, for example gas flows where the Mach number exceeds 0.3. The turbulence model used is the shear stress transport (SST). The k-$\omega$ based SST model accounts for the transport of the turbulent shear stress, and it gives highly accurate predictions of the onset and the amount of flow separation under adverse pressure gradients. The SST model is recommended for high accuracy boundary layer simulations. To benefit from this model, a resolution of the boundary layer of more than 10 points is required.

As described in Sect. 3.3, two approaches are commonly used to model the flow in the near-wall region:

- the wall function method uses empirical formulas that impose suitable conditions near the wall without resolving the boundary layer. In this way it is possible to save computational resources. The major advantages of the wall function approach is that the high gradient shear layers near walls can be modeled with relatively coarse meshes. It also avoids the need to account for viscous effects in the turbulence model.

- The Low-Reynolds-Number method resolves the details of the boundary layer profile by using very small mesh length scales in the direction normal to the wall (very thin inflation layers). Turbulence models based on the $\omega$-equation, such as the SST model, are suitable for a low-Re method. Note that the low-Re method does not refer to the device Reynolds number, but to the turbulent Reynolds number, which is low in the viscous sublayer. The low-Re approach requires a very fine mesh in the near-wall zone and correspondingly large number of nodes. To reduce the resolution requirements, an automatic wall treatment was developed by CFX, which allows a gradual switch between wall functions and low-Reynolds number grids, without a loss in accuracy.

Hence for the SST model an Automatic near-wall treatment method is applied.

For the convergence control, 40 iterations have been set with the maximum timescale of $1 \cdot 10^{-6}$, and then the maximum number of iterations has been changed into 260 with the maximum timescale of $1 \cdot 10^{-5}$. The timescale influences the stability of the solution. Hence, if the maximum timescale is low, the solution becomes more stable. Therefore, in this study, the solution has more probability to diverge in the first 40 iterations, hence the maximum timescale is reduced to $1 \cdot 10^{-6}$ to improve the solution and to make it more stable.

Some *Monitors* have been defined to control the evolution and the convergence of the simulation. In particular, the Monitors created are:

- MONITOR TO CONTROL THE MACH NUMBER NEAR HUB:
  - *Option*: **Cartesian coordinates**
  - *Output Variable list*: **Mach Number**
  - *Cartesian coordinates*: **0.14, 0.045, 0.11**
- MONITOR TO CONTROL THE MACH NUMBER NEAR TIP:
  - *Option*: **Cartesian coordinates**
  - *Output Variable list*: **Mach Number**
  - *Cartesian coordinates*: **0.215, 0.09, 0.08**
- MONITOR TO CONTROL THE MASS FLOW RATE AT THE OUTLET:
  - *Expression*: **massFlow()@R67outlet**
- MONITOR TO CONTROL THE TOTAL PRESSURE AT THE OUTLET:

  - *Expression*: **massFlowAveAbs(Total Pressure in Stn Frame) @ R67outlet**

- MONITOR TO CONTROL THE TOTAL TEMPERATURE AT THE OUTLET:

  - *Expression*: **massFlowAveAbs(Total Temperature in Stn Frame) @ R67Outlet**

### 3.4.2 CFX Solver-Manager

The CFX-Solver Manager takes as input the definition file generated by CFX-Pre. CFX-Solver Manager is a graphical user interface that is used to set attributes for CFD calculation, control the CFX-Solver interactively, and view information about the emerging solution. CFX-Solver Manager allows to select the numerical precision and to choose between the serial and the parallel run mode. For this study, the double precision scheme has been used. The double precision permits more accurate numerical mathematical operation. When double precision is used, the computer memory used for a given problem and grid size are double that of the default (single precision) executable. In another way, the maximum problem size to run on a given computer for the double precision executable is half that of the default single precision executable. As the computer used has 12 CPUs, it has been decided to run the simulation in parallel mode on 10 CPUs (the remaining two are necessary for the GA). Each simulation has been initialized by using a file of initialization. This file is the result file of a simulation of the original geometry with the settings written in the Sect. 3.4.1 and 1000 iterations.

### 3.4.3 CFX-Post

The results file of simulation is then loaded into CFX-Post, where it can be analyzed.

After the initialization of the results, it is possible to extract the thermodynamic parameters useful for the optimization process: the pressure ratio and the isentropic efficiency. Hence, the expressions of isentropic efficiency and pressure ratio are created in the Expressions tab:

**Pressure ratio** is the ratio between the total pressure at the outlet and the total pressure at the inlet of the rotor. In the CFX-Post, it has been defined as:

**massFlowAve**(Total Pressure in Stn Frame)**@R67 Outlet/massFlowAve** ( Total Pressure in Stn Frame)**@R67 Inlet**

**Isentropic Efficiency** is defined as:

$$\eta = \frac{PR^{\frac{\gamma-1}{\gamma}} - 1}{\frac{T_{t2}}{T_{t1}-1}} \tag{3.3}$$

where PR is the pressure ratio, $\gamma$ is a constant value ($\gamma = 1.4$ for the air), $T_{t2}$ and $T_{t1}$ are the total temperature at the outlet and at the inlet respectively. In the CFX-Post, it has been defined as:

(rappcomp^(0.4/1.4)-1)/(**massFlowAve**(Total Temperature in Stn Frame)@ **R67 Outlet** /**massFlowAve**(Total Temperature in Stn Frame)@**R67 Inlet** -1)

**MassFlowAve** means that the total pressure value is evaluated as the average total pressure value on the mass flow rate. The values obtained are exported and saved in a ASCII file (.dat) to be read by the genetic algorithm.

## 3.5 Genetic algorithm set-up

In this section, a brief description of the GA set-up is given. The GA used in this thesis is the genetic algorithm implemented in MATLAB. Hence, most of the description provided are taken directly from the MATLAB User Guide [23].

### 3.5.1 Number of generations and number of individuals

The number of individuals for each generation and the maximum number of generations are two fundamental parameters in the GA set-up, because they determine the algorithm exploration capacity. A high number of individuals allows a high number of crossovers, and a good decision variable space exploration is achieved if the initial population is enough spread. The maximum number of generations determines the algorithm ability to find the optimal x in the regions returned as the more interesting from an optimization point of view by exploration phase. Hence, a high number of individuals and generations is suggested to obtain better results. On the other hand, a high number of individuals and generations implies a high number of fitness function computation, hence a high computation time. Thus, it is important to find a trade-off between the quality of the results and the computational time required. In this thesis, it has been decided to use 10 generations and 6 individuals for the optimization of the blade tip, and 10 generations and 10 individuals for the optimization of the whole blade. The initial population has been created randomly

by a used function. The user function is implemented to generate individuals that spread in the whole design space.

### 3.5.2 Selection

The MATLAB GA provides six selection options:

**Stochastic uniform** "the default selection function, stochastic uniform, lays out a line in which each parent correspond to a section of the line of length proportional to its scaled value. The algorithm moves along the line in steps of equal size. At each step, the algorithm allocates a parent from the section it lands on. The first step is a uniform random number less than the step size" [23].

**Remainder** "Remainder selection assigns parents deterministically from the integer part of each individual's scaled value and then uses roulette selection on the remaining fractional part. For example, if the scaled value of an individual is 2.3, that individual is listed twice as a parent because the integer part is 2. After parents have been assigned according to the integer parts of the scaled values, the rest of the parents are chosen stochastically. The probability that a parent is chosen in this step is proportional to the fractional part of its scaled value" [23].

**Uniform** "Uniform selection chooses parents using the expectations and number of parents. Uniform selection is useful for debugging and testing, but is not a very effective search strategy" [23].

**Roulette** "Roulette selection chooses parents by simulating a roulette wheel, in which the area of section of the wheel corresponding to an individual is proportional to the individual's expectation. The algorithm uses random number to select one of the sections with a probability equal to its area" [23].

**Tournament** "Tournament selection chooses each parent by choosing Tournament size players at random and then choosing the best individual out of that set to be a parent. Tournament size must be at least 2. The default value of Tournament size is 4" [23].

The Tournament selection has been chosen with a Tournament size of 2, as suggested previously.

### 3.5.3 Reproduction

The reproduction is based on the Crossover operator - as described in Sect. 2.6.2 - and it specifies how the genetic algorithm combines two individuals, or parents, to form a crossover child for the next generation. The options available are [23]:

**Scattered** this is the default crossover function. "It creates a random binary vector and selects the genes where the vector is a 1 from the first parent, and the genes where the vector is a 0 from the second parent, and combines the genes to form the child". For example, if $\vec{x}_1$ and $\vec{x}_2$ are the parents, and the $\vec{b}$ is the binary vector, the children returned are $\vec{x}_{c,1}$ and $\vec{x}_{c,2}$

$$\vec{x}_1 = [abcdefgh] \tag{3.4}$$
$$\vec{x}_2 = [12345678] \tag{3.5}$$
$$\vec{b} = [11001000] \tag{3.6}$$
$$\vec{x}_{c,1} = [ab34e678] \tag{3.7}$$
$$\vec{x}_{c,2} = [12cd5fgh] \tag{3.8}$$

**Single point** It chooses a random integer $n$ between 1 and Number of variables and then

1. Selects vector entries numbered less than or equal to $n$ from the first parent.
2. Selects vector entries numbered greater than $n$ from the second parent.
3. Concatenates these entries to form a child vector.

For example, if $\vec{x}_1$ and $\vec{x}_2$ are the parents, and the crossover point is 6, the children generated are $\vec{x}_{c,1}$ and $\vec{x}_{c,2}$

$$\vec{x}_1 = [abcdefgh] \tag{3.9}$$
$$\vec{x}_2 = [12345678] \tag{3.10}$$
$$\vec{x}_{c,1} = [abcdef78] \tag{3.11}$$
$$\vec{x}_{c,2} = [123456gh] \tag{3.12}$$

**Two point** It chooses randomly two crossover points in the two parents. The chromosomes between the two crossover points in the two parents are interchanged

to produce two new children. For example, if $\vec{x}_1$ and $\vec{x}_2$ are the parents, and the crossover point are 2 and 6, the children generated are $\vec{x}_{c,1}$ and $\vec{x}_{c,2}$

$$\vec{x}_1 = [abcdefgh] \tag{3.13}$$
$$\vec{x}_2 = [12345678] \tag{3.14}$$
$$\vec{x}_{c,1} = [ab3456gh] \tag{3.15}$$
$$\vec{x}_{c,2} = [12cdef78] \tag{3.16}$$

**Intermediate** It creates childrens by taking a weighted average of the parents. The weights can be specified by a single parameter, which can be a scalar (r) or a row vector of length number of variables ($\vec{r}$). The function creates the childrens from $\vec{x}_1$ and $\vec{x}_2$ using the following formula, where rand is a random number between 0 and 1.

$$\vec{x}_{c,1} = \vec{x}_1 + \text{rand}\vec{r}(\vec{x}_2 - \vec{x}_1) \tag{3.17}$$
$$\vec{x}_{c,2} = \vec{x}_1 - \text{rand}\vec{r}(\vec{x}_2 - \vec{x}_1) \tag{3.18}$$

**Heuristic** "It returns a child that lies on the line containing the two parents, a small distance away from the parent with the better fitness value in the direction away from the parent with the worse fitness value. You can specify how far the child is from the better parent by the parameter $r$". If $\vec{x}_1$ and $\vec{x}_2$ are the parents, and $\vec{x}_1$ has the better fitness value, the function returns the children $\vec{x}_{c,1}$ and $\vec{x}_{c,2}$ by

$$\vec{x}_{c,1} = \vec{x}_2 + r(\vec{x}_1 - \vec{x}_2) \tag{3.19}$$
$$\vec{x}_{c,2} = \vec{x}_1 \tag{3.20}$$

**Arithmetic** It creates children that are the weighted arithmetic mean of two parents.

**Custom** It enables the user to write your own crossover function.

For this thesis the default option Scattered has been selected.

The *CrossoverFraction* is an option that gives the possibility to set how many individuals have to be generated by a crossover process in each generation; the rest

of the population is generated by mutation. The value sets up is the default value of 0.8 (80%).

### 3.5.4 Mutation

This option specifies how the genetic algorithm makes small random changes in the individuals to create mutation children. The options available are:

**Gaussian** "The default mutation function, Gaussian, adds a random number taken from a Gaussian distribution with mean 0 to each entry of the parent vector" [23].

**Uniform** "Uniform mutation is a two-step process. First, the algorithm selects a fraction of the vector entries of an individual for mutation, where each entry has a probability rate of being mutated. In the second step, the algorithm replaces each selected entry by a random number selected uniformly from the range for that entry" [23].

**Adaptive Feasible** " Adaptive feasible mutation randomly generates directions that are adaptive with respect to the last successful or unsuccessful generation. The feasible region is bounded by the constraints and inequality constraints. A step length is chosen along each direction so that linear constraints and bounds are satisfied" [23].

In this study, the Adaptive Feasible has been used because the feasible region is narrow and beyond this region the simulation diverges.

### 3.5.5 GA for the optimization of the whole blade

In the optimization of the whole blade, 10 generations and 10 individuals are set up.

To reduce the optimization time and inspired by the hierarchical GA (Sect. 2.7.2), it has been decided to make a optimization process by using a coarse mesh with about 190000 elements, and then a second simulation by using a fine mesh with about 2 million elements. At the end of the first simulation, the Pareto front generated is used to create the initial population of the second optimization process. The second optimization is made by using a fine mesh with about 2 million elements. Hence, the second simulation uses the design space regions provided by the first optimization for the exploitation phase. The main difference between the two optimizations is the model chosen to solve the boundary layer. In the first one, the boundary layer has been solved by using the wall functions, while a direct boundary

layer resolution has been used in the second simulation. This choice was able to reduce the number of cells and the computational time. The first optimization with the coarse mesh had a time of calculation of two days by using 6 processors, whereas the time of calculation of the second optimization with the fine mesh was about ten days by using 10 processors.

## 3.6 Fitness function

The aim of this thesis is to optimize the performance of a transonic compressor rotor, in particular to maximize the pressure ratio and the isentropic efficiency. The pressure ratio is the ratio between the total pressure at the outlet and at the inlet of the rotor:

$$PR = \frac{P_2}{P_1} \tag{3.21}$$

The isentropic efficiency is:

$$\eta = \frac{T_{t2,is} - T_{t1}}{T_{t2} - T_{t1}} \tag{3.22}$$

where $T_{t2,is}$ is the isentropic total temperature at the outlet of the rotor, $T_{t1}$ is the total temperature at the inlet and $T_{t2}$ is the total temperature at the outlet. If the isentropic relationships between total temperature and total pressure have been considered:

$$\frac{P_2}{P_1} = \left(\frac{T_{t2}}{T_{t1}}\right)^{\frac{\gamma}{\gamma-1}} \tag{3.23}$$

the equation Eq. 3.22 becomes:

$$\eta = \frac{PR^{\frac{\gamma-1}{\gamma}} - 1}{\frac{T_{t2}}{T_{t1}-1}} \tag{3.24}$$

The values of the initial geometry are:

$$\begin{aligned} PR &= 1.5558 \\ \eta &= 0.8916 \end{aligned}$$

As the MATLAB GA is implemented to minimize the parameters chosen, hence, the ratios $1/PR$ and $1/\eta$ are considered as fitness functions of the optimization. If some error is generated during the optimization process (mesh error or simulation divergence), a penalty function is used. The ratios $1/PR$ and $1/\eta$ are assumed 1000.

# Chapter 4

# Results

## 4.1 Optimization of the blade tip

The Fig. 4.1 shows the Pareto front obtained from the optimization of the blade tip. The three numbered individuals makes up the Pareto front. Two of them belong to the generation number 10, and one individual belongs to the ninth generation.

Fig. 4.2 and Fig. 4.3 show the $\Delta\theta$ limit range and the distribution of the isentropic efficiency of the control point at 95% of the span (Fig. 4.2), and the isentropic efficiency of the control point at 100% of the span (Fig. 4.3). Hence, it is possible to see that these values are centered on a region, and they are not scattered. Therefore the range of $\Delta\theta$ chosen for the optimization process seems to be appropriate and it must not be extended.

The Tab. 4.1 represents the PR and $\eta$ values of the initial configuration of the blade and of the three individuals on the Pareto front.

The point 3 has maximum efficiency, hence:

$$\frac{\eta_3}{\eta_{in}} = 1.0074 \tag{4.1}$$

$$\frac{PR_3}{PR_{in}} = 1.00025 \tag{4.2}$$

| | PR | $\eta$ |
|---|---|---|
| Initial Values | 1.5558 | 0.8916 |
| Point 1 | 1.5563 | 0.8979 |
| Point 2 | 1.5563 | 0.8980 |
| Point 3 | 1.5562 | 0.8982 |

**Table 4.1:** Tip optimization results

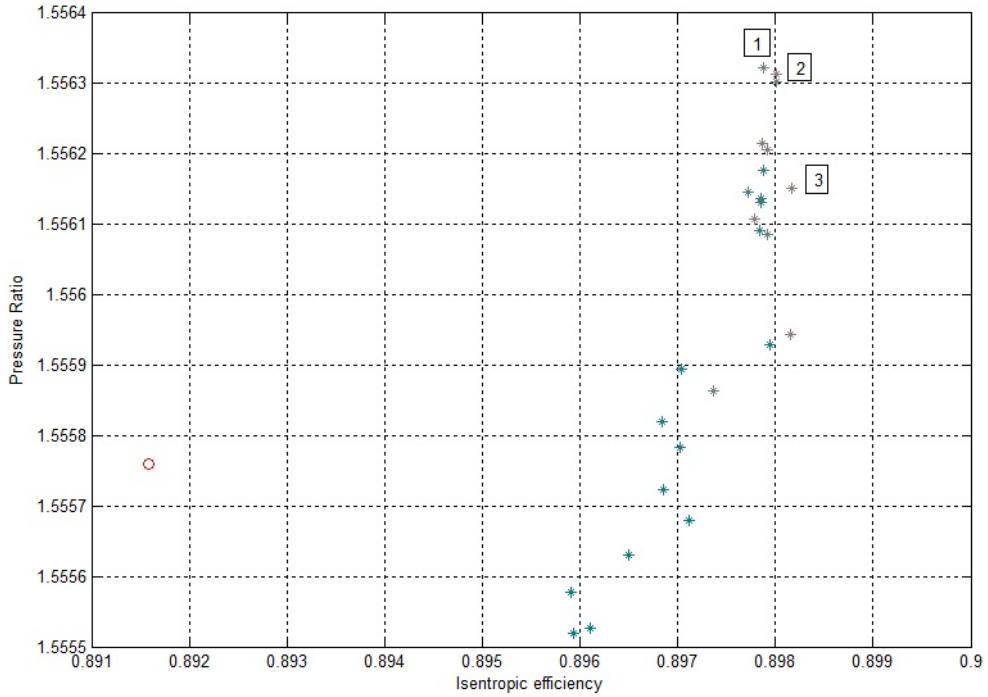


**Figure 4.1:** Evolution of the blade tip optimization.

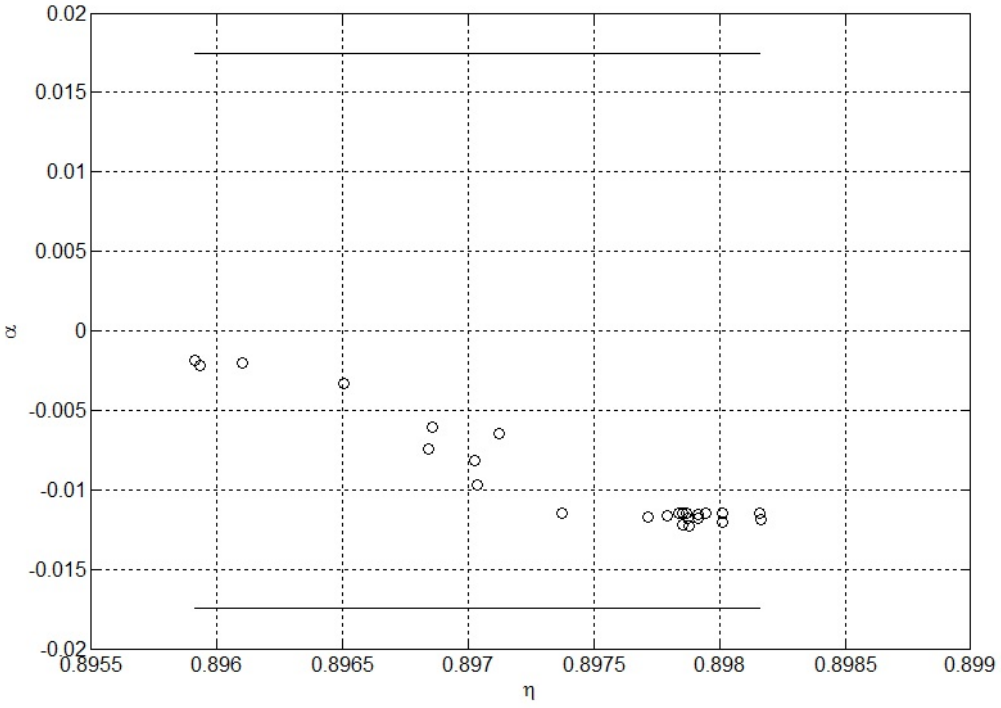


**Figure 4.2:** $\alpha - \eta$ distribution of the control point at 95% of the span

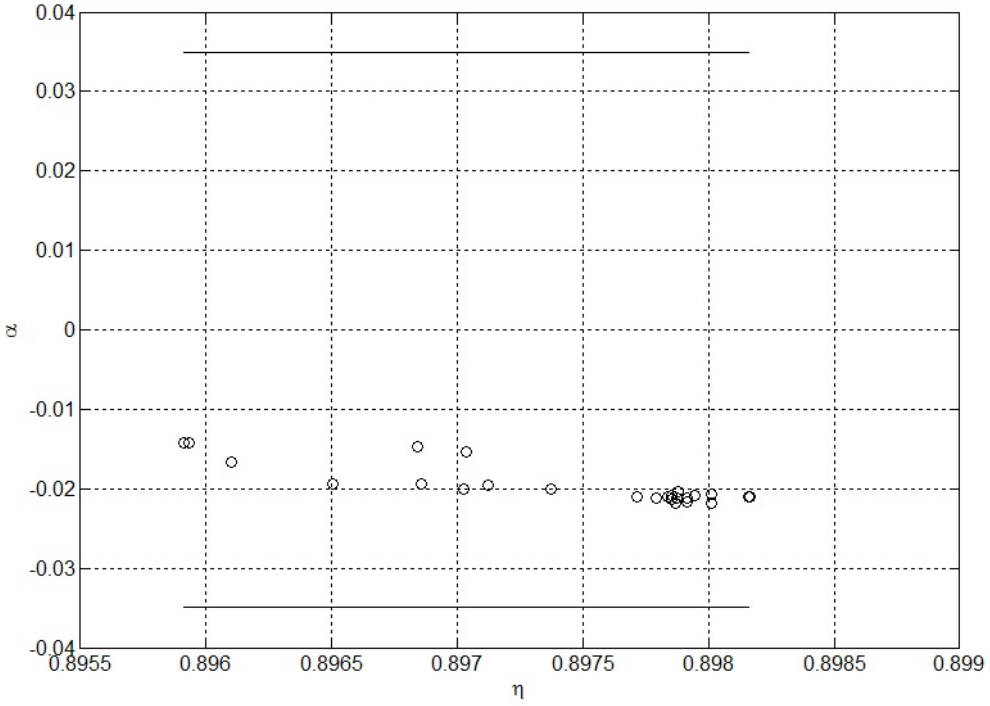


**Figure 4.3:** $\alpha - \eta$ distribution of the control point at 100% of the span

It is possible to see that the increase of the isentropic efficiency is 0.7% and the increase of the pressure ratio is 0.025%. If the individual with maximum PR (number 1) is considered:

$$\frac{\eta_1}{\eta_{in}} = 1.00704 \tag{4.3}$$

$$\frac{PR_1}{PR_{in}} = 1.00036 \tag{4.4}$$

The increases are 0.7% and 0.036%. In both cases, the PR increase is not relevant, but the increase of the isentropic efficiency of 0.7% is a sensible increase for a transonic compressor. In fact, the transonic compressor rotors are not simple to optimize, and the blade considered in this study was already optimized by NASA laboratory. The individual chosen for the result analysis is the individual with the maximum isentropic efficiency, that is the first individual of the tenth generation.

The displacement angles of this individual are 0.679°and 1.202°, respectively for the points at 95% and 100% of the span. The displacements are in the direction of the blade rotational speed.

The blade tip region is critical for the shock waves produced by the supersonic

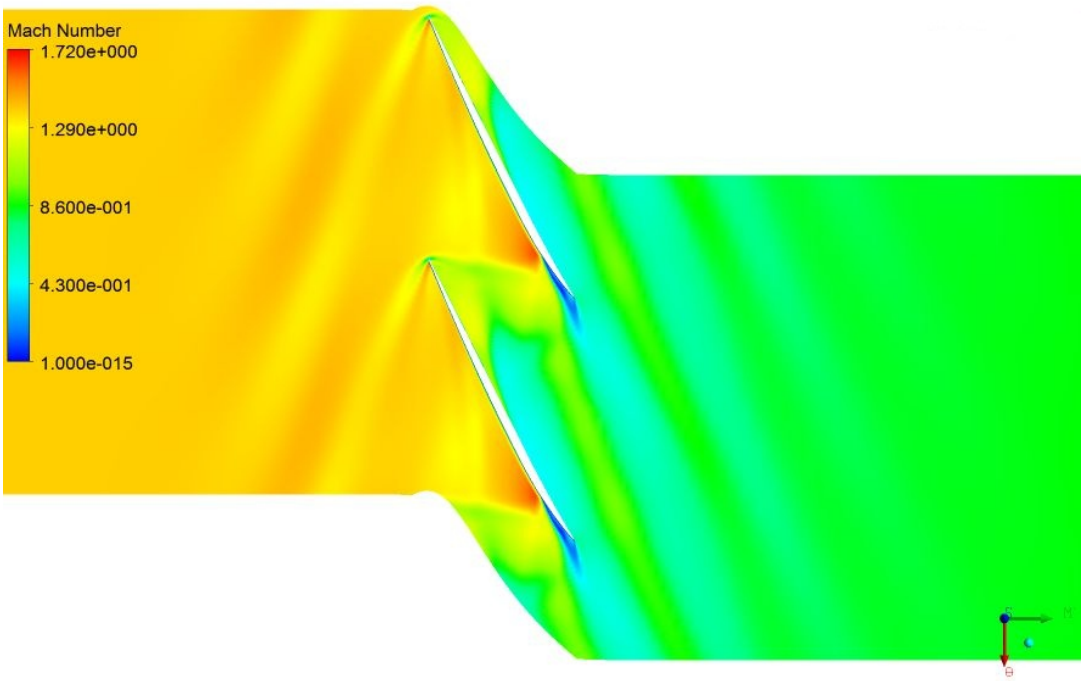


**Figure 4.4:** Mach number at 98% of the span of the initial blade

inlet flow. In the Fig. 4.4 and Fig. 4.5 it is possible to see the Mach number at 98% of the span in the blade with the initial configuration and in the optimized blade. The shock wave is generated at the leading edge and intersects the next blade at about 75% of the chord. This intersection causes the separation of the boundary layer. It is possible to see that there are no significant differences between the Mach number values of the initial blade and the optimized. The shock is slightly more weak in Fig. 4.5, and this means the increase of the isentropic efficiency in the optimized blade.

The Fig.4.6-4.11 shows the trends of isentropic efficiency and the mass flow rate of the optimized blade just downstream the blade (Fig.4.6,4.7), one chord downstream (Fig.4.8,4.9) and at the duct outlet (Fig.4.10,4.11). There is an increase of the isentropic efficiency especially near the hub and minimally on the tip region. Little by little the trends of the original and optimized blade change because the flow mixes and homogenizes itself. The reason why there is a biggest increase of the efficiency near the hub is that there is an increase of the mass flow in that region (as seen in 4.7). This means that there is a better incidence angle of the flow, and hence, the flow separation is delayed. The result is an increase of the isentropic efficiency. The region of the blade near the hub is very important in the transonic compressor, because it is the region affected by corner stall. “Numerical solutions based on the Reynolds-averaged Navier-Stokes equations and available experimental

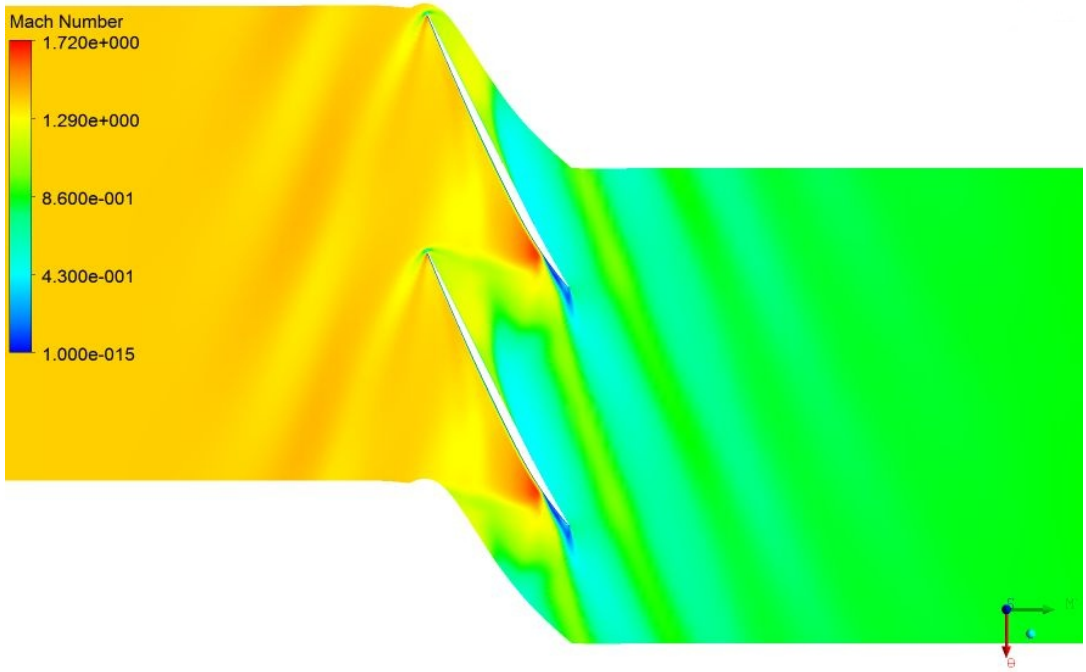


**Figure 4.5:** Mach number at 98% of the span of the optimized blade

data were analyzed to construct detailed flow structures of compressor hub corner stall. The last study reveals that a vortex is formed at the corner of the hub and the blade suction surface toward the rear of the blade passage. The strong twisterlike vortical motion causes reversed flow regions on the hub surface as well as on the blade suction surface. In the compressor stator, the end of the vortex turns back to the hub surface. According to the numerical results, the two counterrotating vortices that have been identified through oil flow visualization are actually two legs of a single vortex. In the rotor, this vortex bends downstream and diffuses quickly, and only one leg of the vortex is observed on the hub surface" [24]. Hub corner stall was considered to be one of the possible causes of the observed total pressure deficiency near the hub at 100 percent rotor speed at near-peak efficiency. Hence, it is important to optimize the performance of the transonic compressor in the hub region. As described previously, the little increase of the isentropic efficiency near the tip region is the consequence of the presence of weaker shock waves in the optimized blade than in the original blade. As shown in Fig.4.10 and 4.11, the improvement near the hub remains, but it is possible to seen also an increase of the isentropic efficiency in the tip region, especially between the 60% and 80% of the span. This fact seems to be caused by a lower flow vorticity at the outlet of the optimized rotor. This phenomenon implies a lower energy dissipation during the flow mixing. Additional results are available in App. A.1.

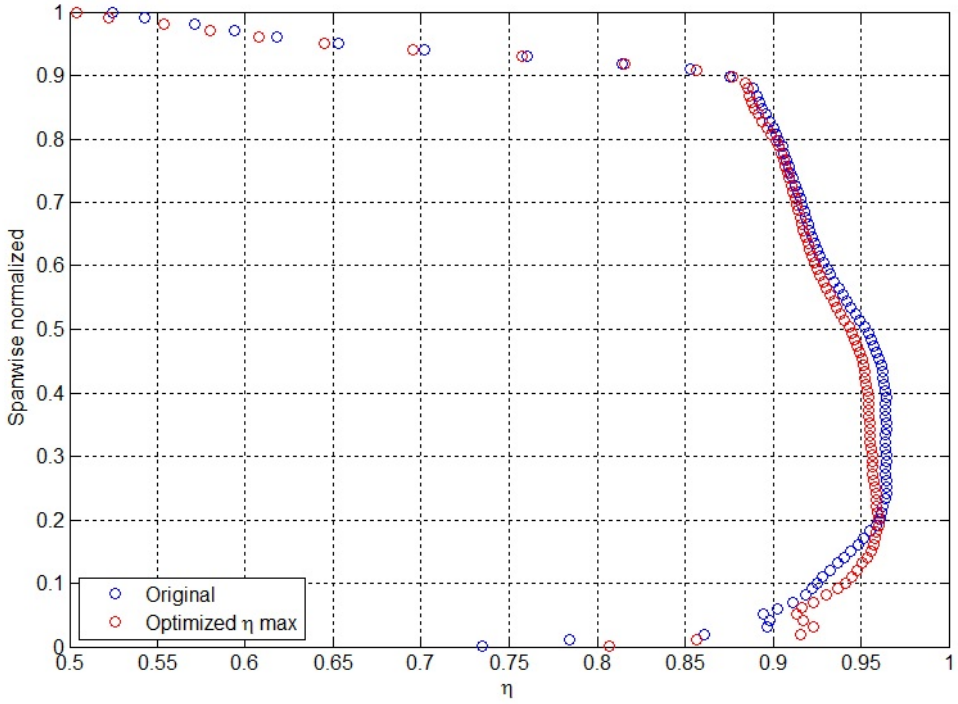


**Figure 4.6:** Isentropic efficiency of the original blade and the optimized blade just downstream the blade.

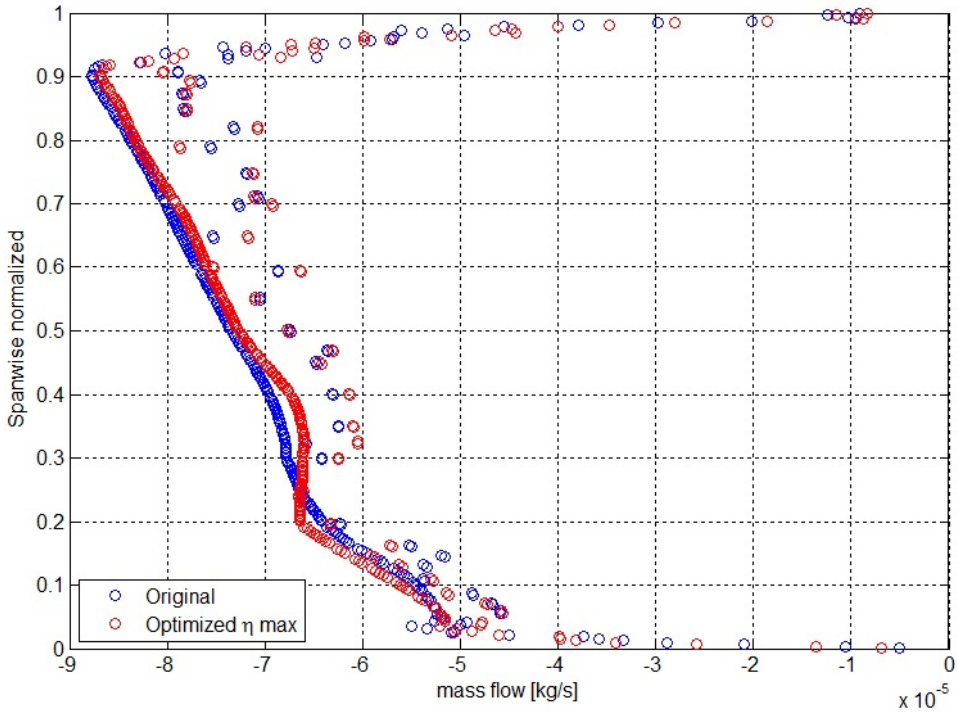


**Figure 4.7:** Mass flow rate of the original blade and the optimized blade just downstream the blade.

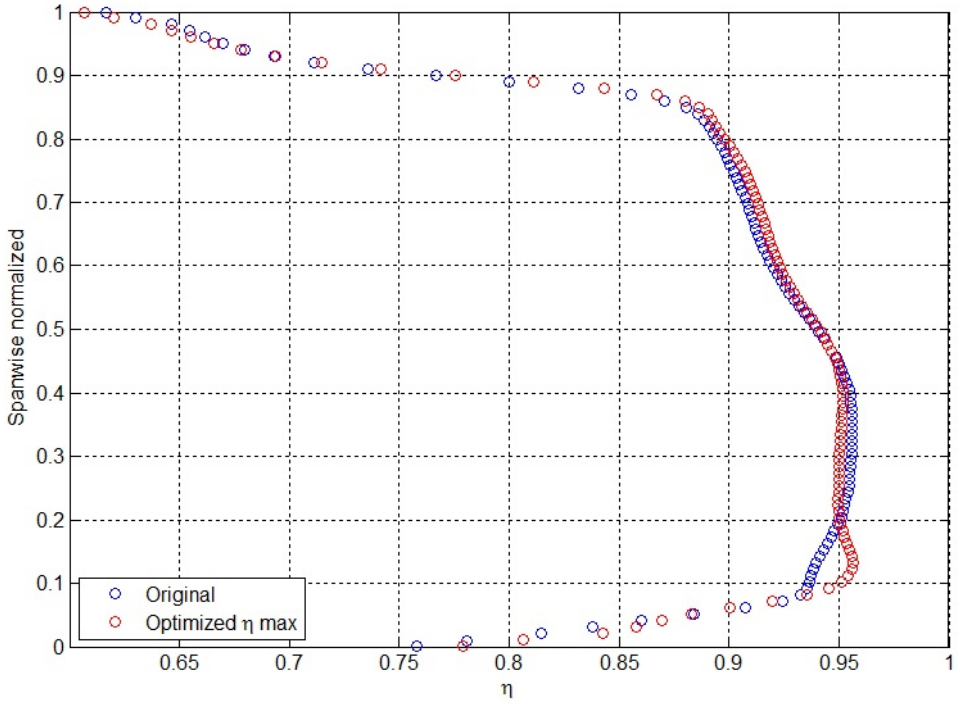


**Figure 4.8:** Isentropic efficiency of the original blade and the optimized blade one chord downstream.

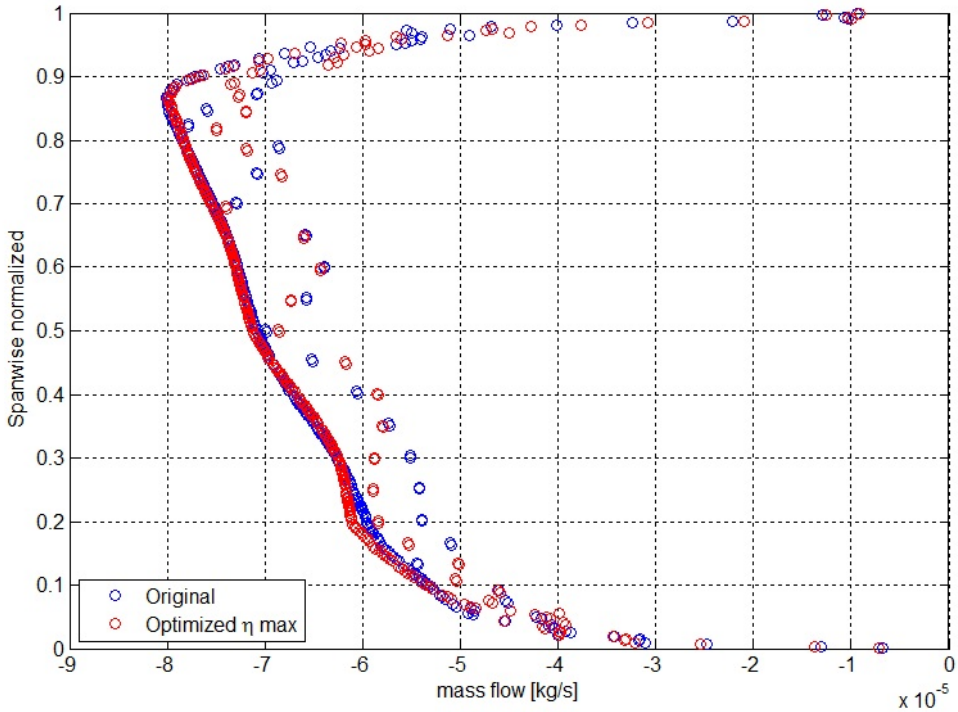


**Figure 4.9:** Mass flow rate of the original blade and the optimized blade one chord downstream.

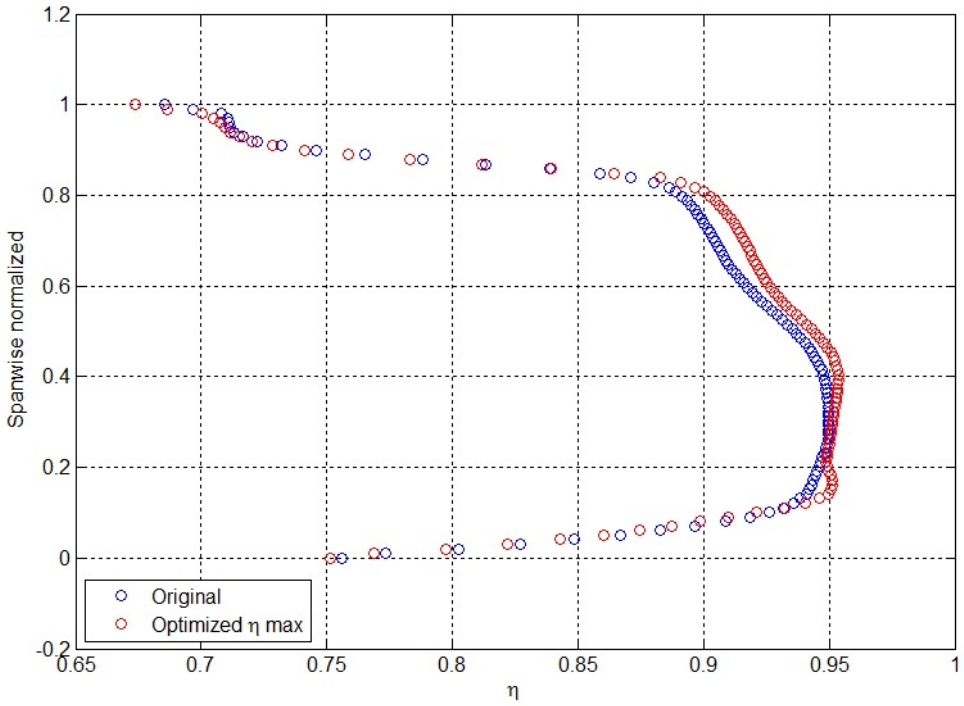


**Figure 4.10:** Isentropic efficiency of the original blade and the optimized blade at duct outlet.

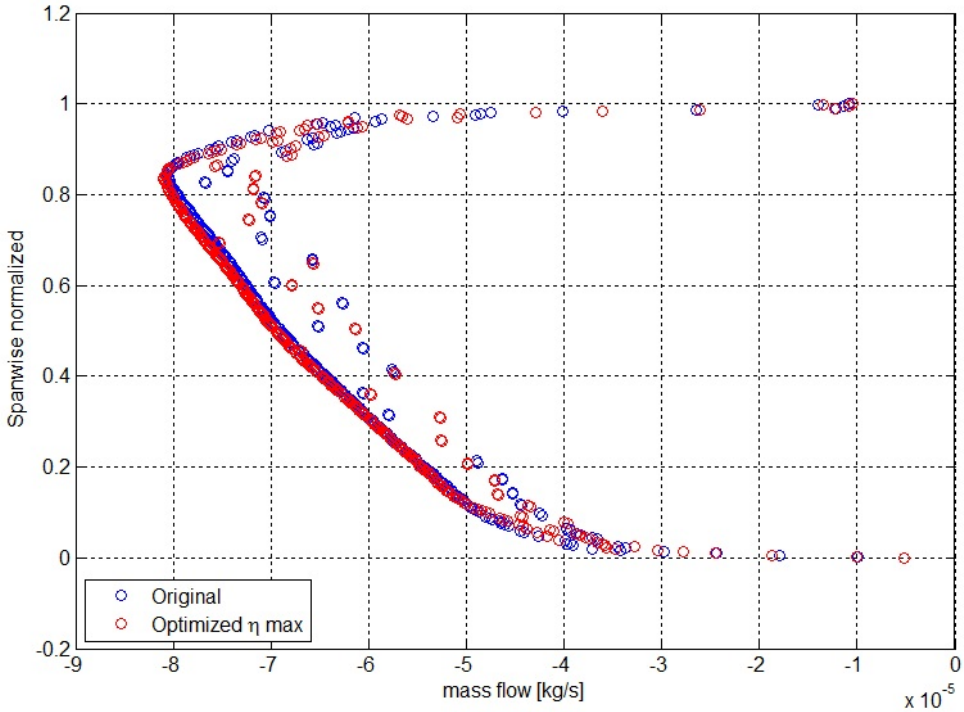


**Figure 4.11:** Mass flow rate of the original blade and the optimized blade at duct outlet.

## 4.2 Optimization of the whole blade

The Fig. 4.12 shows the evolution of the individuals during the optimization process. The Pareto front is composed by four individuals, which belong to the last two generations.

As described in Sect. 3.2.2, the $\Delta\theta$ limit angles $\pm 0.5°$, $\pm 1°$, $\pm 1.5°$ for the control points at 33%, 66% and 90% of the span, and $\pm 1°$, $\pm 2°$ for the last two control points of the tip, depending on the point on 90% of the span. The Fig.4.13-4.17 show that the $\Delta\theta$ range chosen seems to be appropriate, because the distribution of the points is enough far from the boundaries.

The Tab. 4.2 represents the PR and $\eta$ values of the initial configuration of the blade and of the four individuals on the Pareto front.

The point 4 has the maximum isentropic efficiency:

$$\frac{\eta_4}{\eta_{in}} = 1.005 \tag{4.5}$$

Hence, the efficiency increase is 0.5%. To evaluate the pressure ratio increase, the individual represented by the point 1 has been considered:

$$\frac{PR_1}{PR_{in}} = 1.000898 \tag{4.6}$$

Hence, the PR increase is about 0.09%. Hence, the individuals chosen for the result analysis are the individuals represented by the points 1 and 4, and both of them belongs to the last generation. The displacement angles of the individual with maximum PR are 0.3327°, -0.3398°, -0.3387°, -0.1595°, -0.8673°, respectively for the points at 33%, 66%, 90%, 95% and 100%. The sign minus represent the direction of the displacement, that is in the direction of the blade rotational speed. The displacement angles of the individual with maximum isentropic efficiency are 0.3248°, -0.3033°, 0.7777°, 0.00842°, 0.1916°, respectively for the points at 33%, 66%, 90%, 95% and 100% of the span.

| | PR | $\eta$ |
|---|---|---|
| Initial Values | 1.5558 | 0.8916 |
| Point 1 | 1.5572 | 0.8941 |
| Point 2 | 1.5568 | 0.8946 |
| Point 3 | 1.5563 | 0.8953 |
| Point 4 | 1.5551 | 0.8959 |

**Table 4.2:** Blade optimization results

The Fig. 4.18-4.23 shows the trends of isentropic efficiency and the mass flow rate of the optimized blade (individual with PR max and individual with $\eta$ max) just downstream the blade (Fig. 4.18, 4.19), one chord downstream (Fig. 4.20, 4.21) and at the duct outlet (Fig. 4.22, 4.23). As described in Sect. 4.1, there is an increase of the isentropic efficiency especially near the hub, due to the increase of the mass flow rate in that region. As shown in Fig. 4.18 4.19, there's a decrease of the isentropic efficiency around the 40% of the span. The reason is a decrease of the mass flow rate in that region. The trend of the original and optimized blade change moving away from the blade, because the flow mixes and homogenizes itself. Finally, as described in Sect. 4.1, the little increase of the isentropic efficiency near the tip region is due to a reduction of energy dissipation during the flow mixing. Additional results are available in App. A.2.

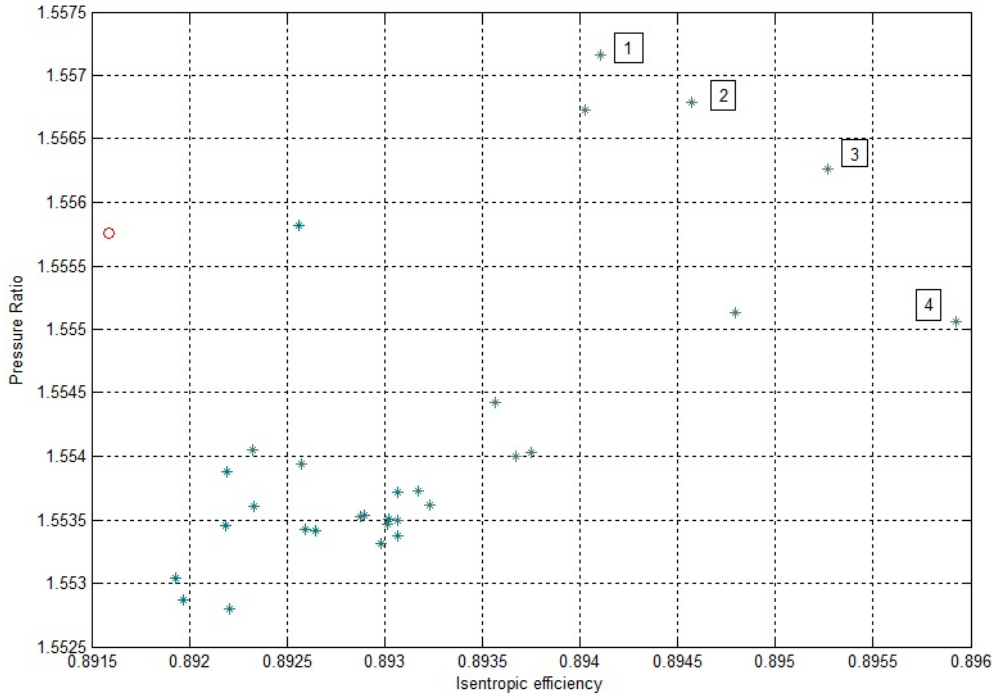


**Figure 4.12:** Evolution of the whole blade optimization

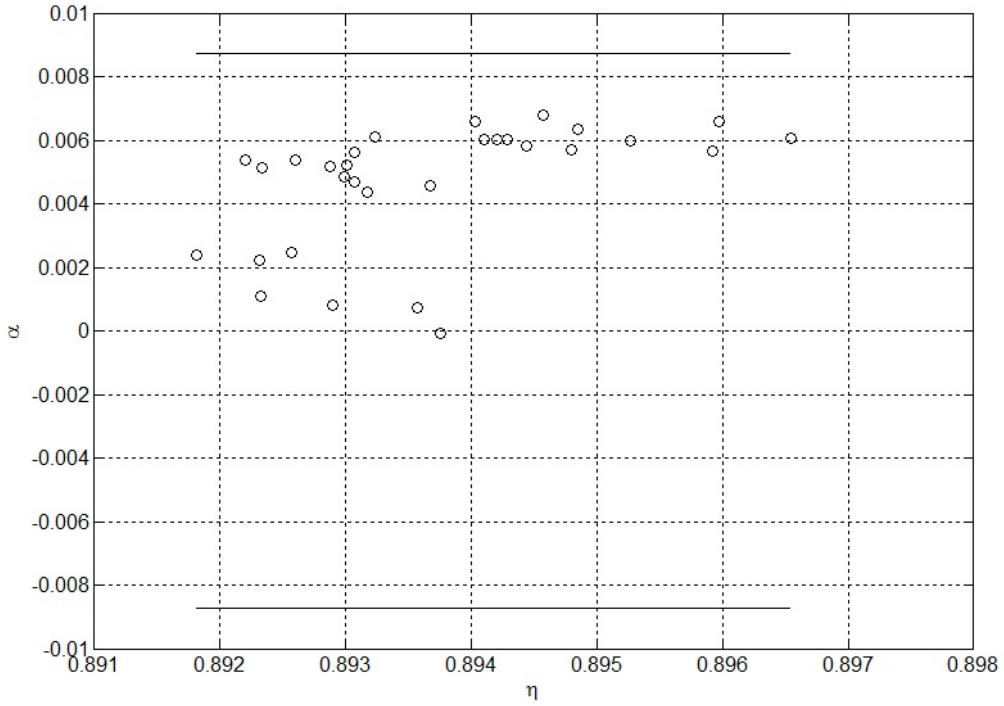


**Figure 4.13:** $\alpha - \eta$ distribution of the control point at 33% of the span

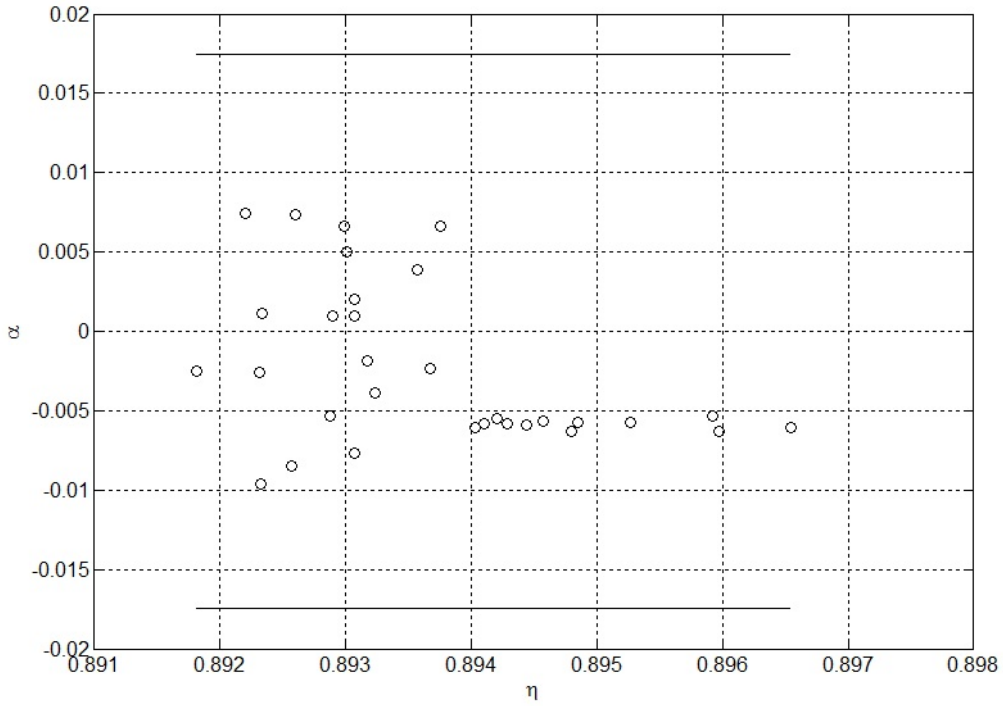


**Figure 4.14:** $\alpha - \eta$ distribution of the control point at 66% of the span

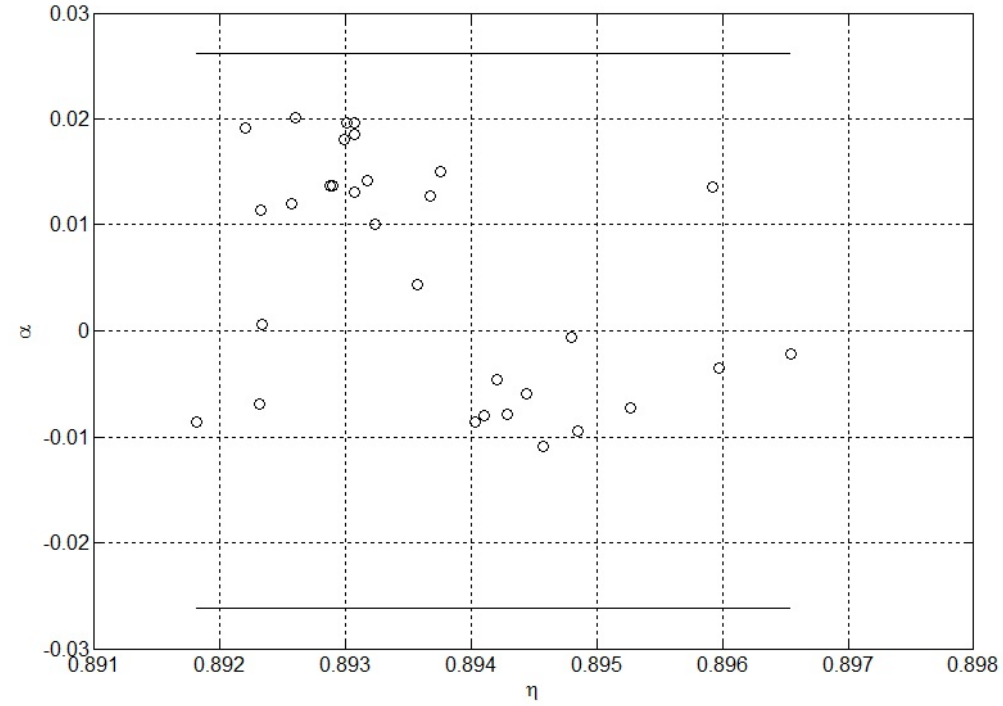


**Figure 4.15:** $\alpha - \eta$ distribution of the control point at 90% of the span

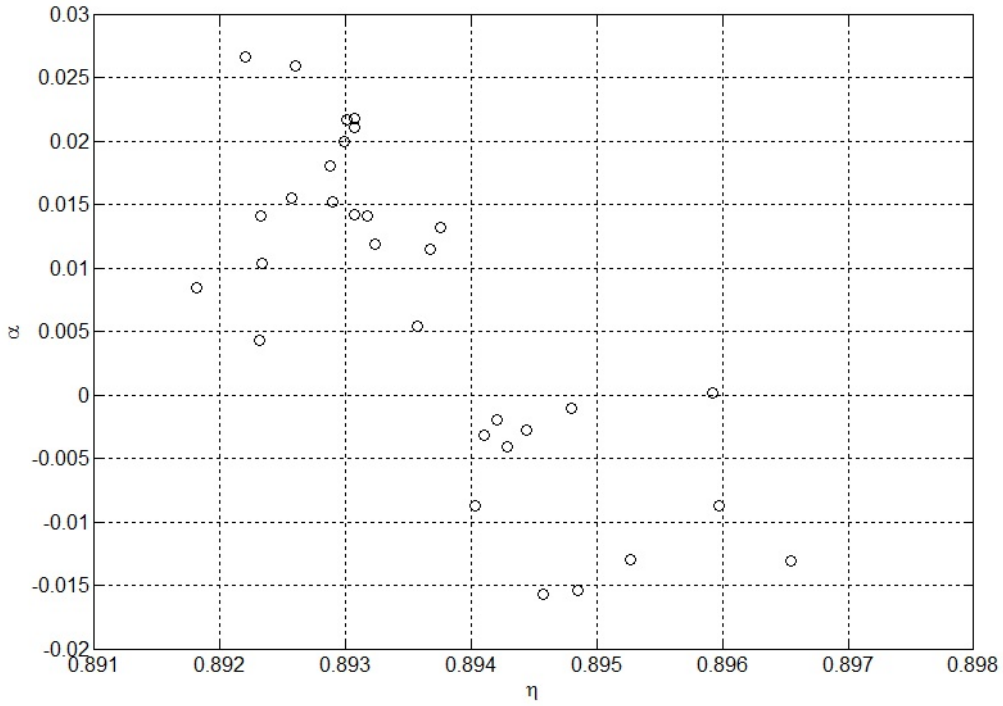


**Figure 4.16:** $\alpha - \eta$ distribution of the control point at 95% of the span

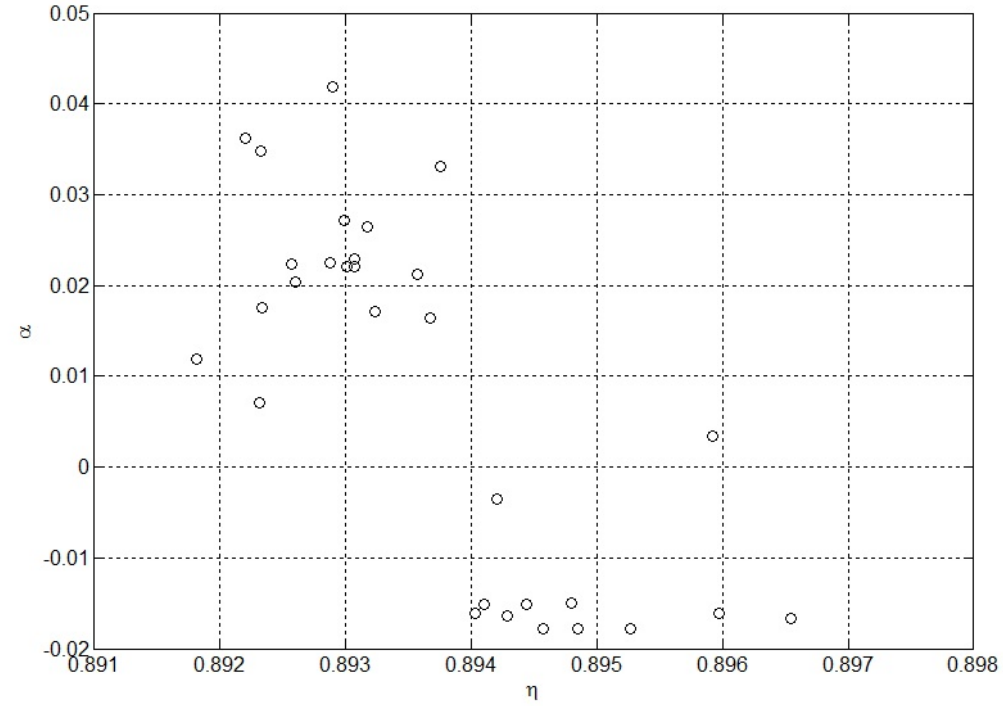


**Figure 4.17:** $\alpha - \eta$ distribution of the control point at 100% of the span

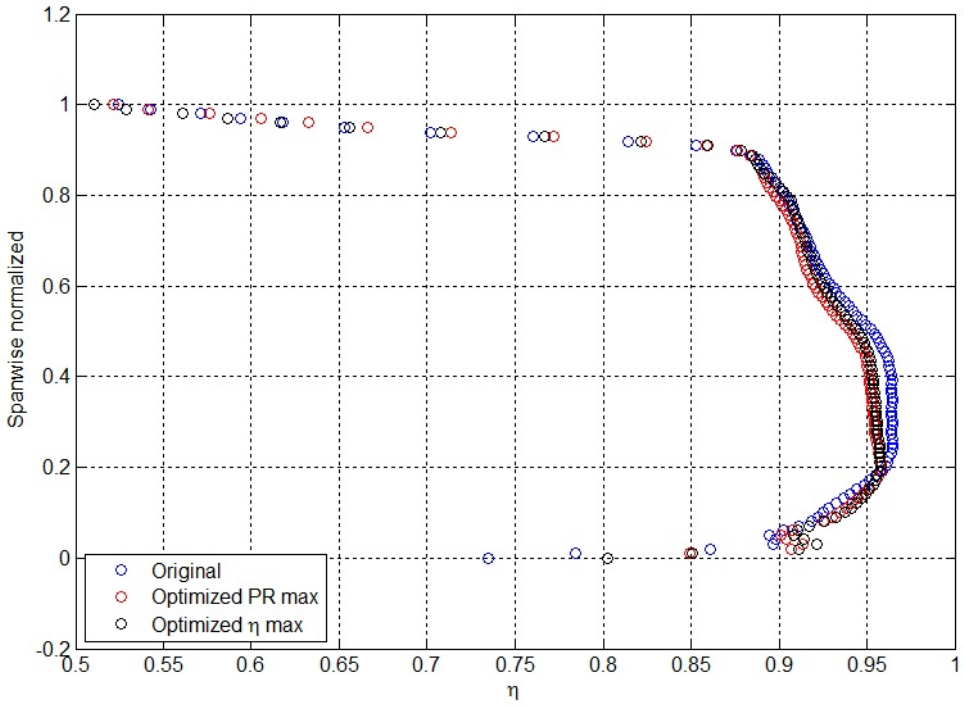


**Figure 4.18:** Isentropic efficiency of the original blade and the optimized blade just downstream the blade.

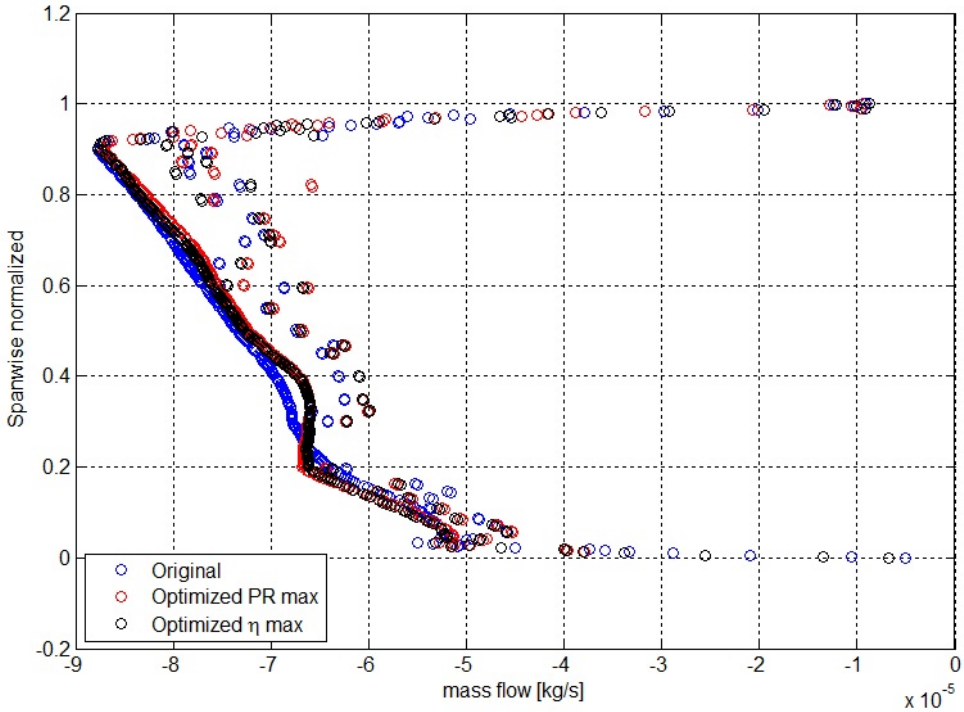


**Figure 4.19:** Mass flow rate of the original blade and the optimized blade just downstream the blade.

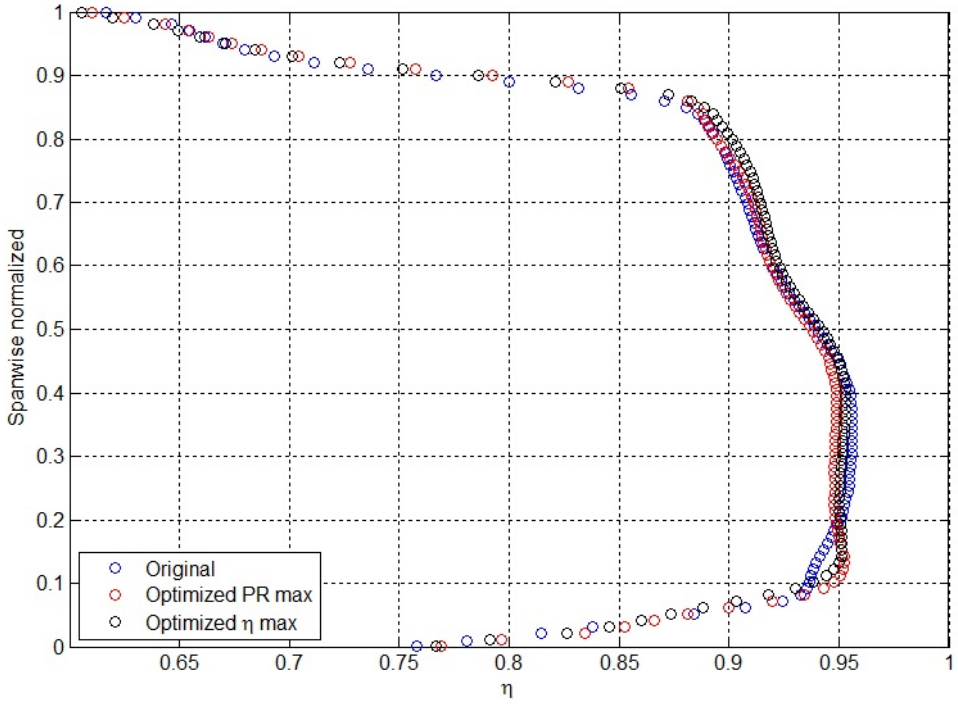


**Figure 4.20:** Isentropic efficiency of the original blade and the optimized blade one chord downstream.

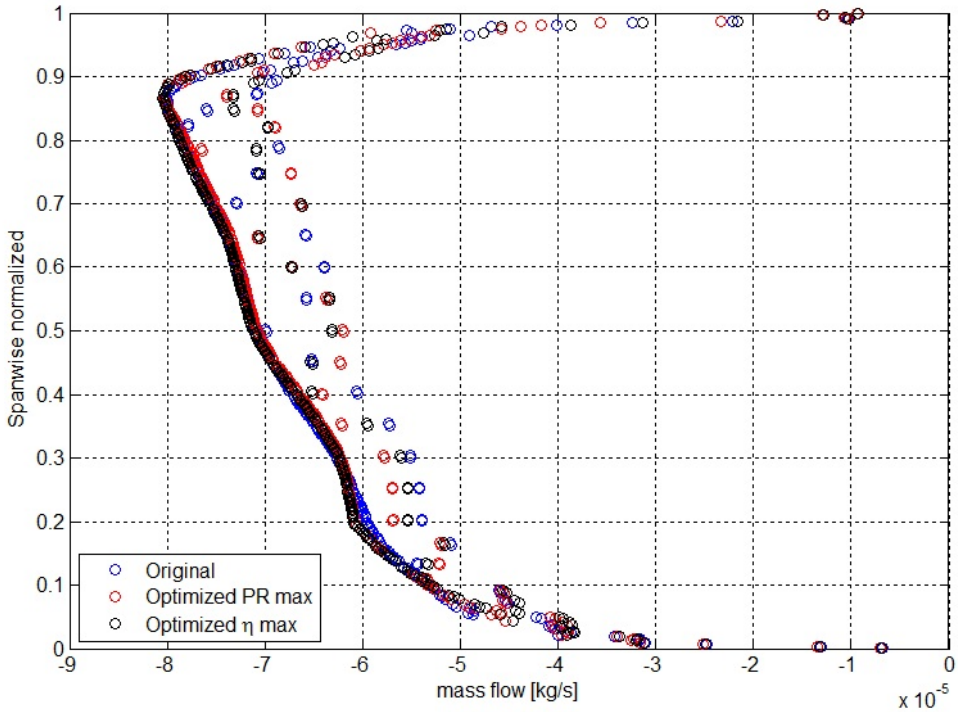


**Figure 4.21:** Mass flow rate of the original blade and the optimized blade one chord downstream.

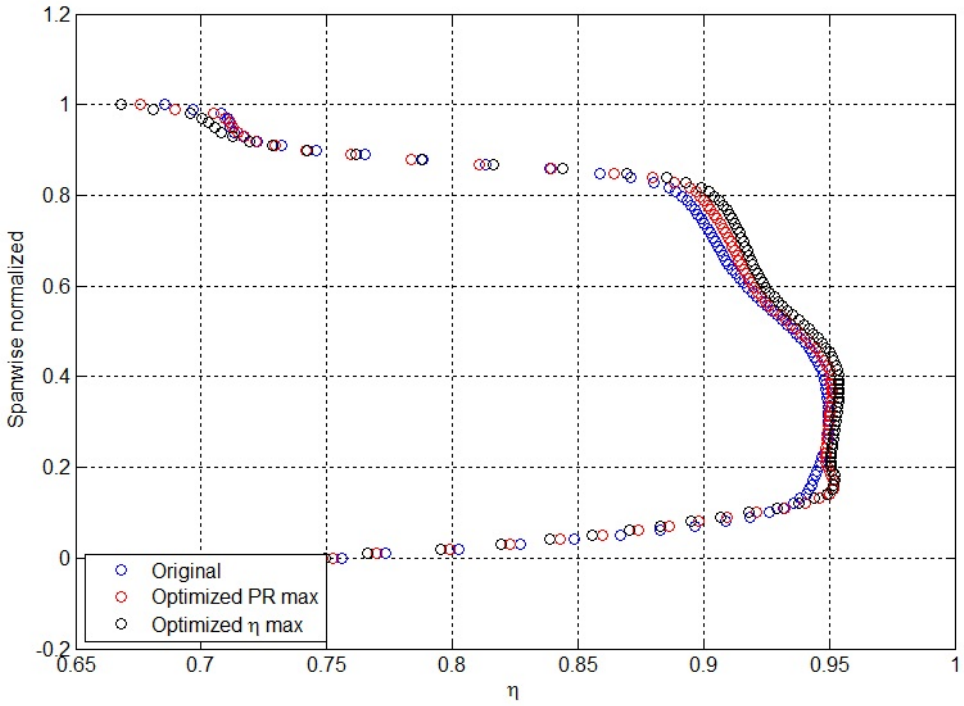


**Figure 4.22:** Isentropic efficiency of the original blade and the optimized blade at the duct outlet.

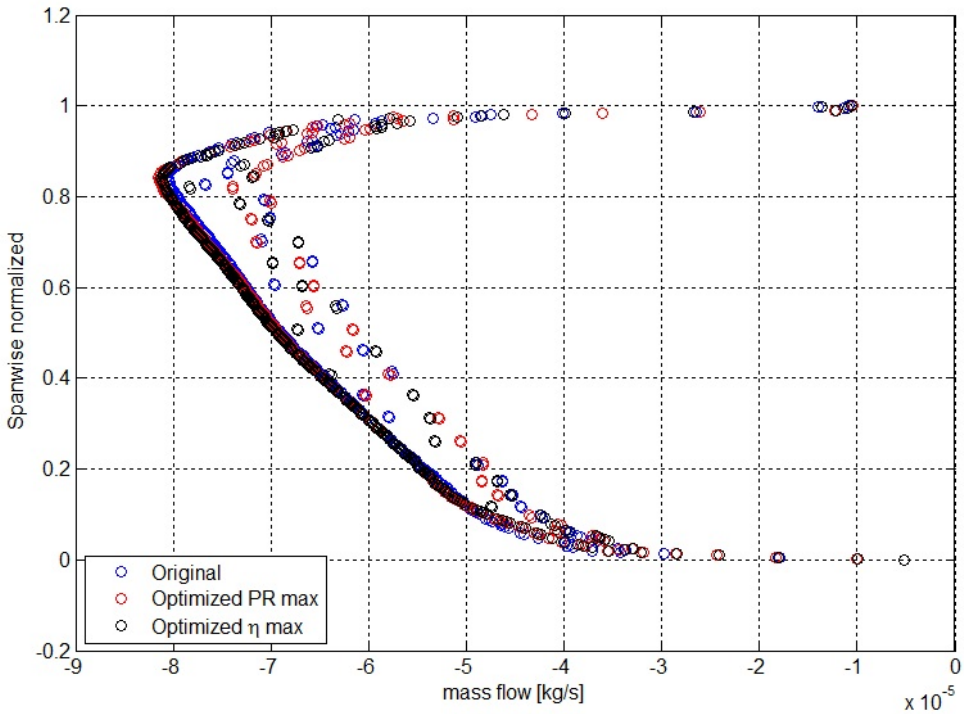


**Figure 4.23:** Mass flow rate of the original blade and the optimized blade at the duct outlet.

# Chapter 5

# Conclusions

The aim of this thesis is to try to optimize a transonic compressor blade, in particular, the NASA Rotor 67. This study wants to maximize the isentropic efficiency and the pressure ratio. The optimization process has been made by changing the stacking line of the blade, or rather by moving the airfoils of the blade on the circumferential plane. This study is divided in two different parts: the optimization of the blade tip and the optimization of the whole blade. The study of the blade tip is important to understand the influence of this region on the 3D pattern of the flow and on the performance of the blade. The blade tip is a critical region because there are shock waves and secondary flows, that entail pressure losses, and hence, they influence negatively the efficiency of the whole blade. In the optimization process, the geometry of the Rotor 67 is discretized by 14 sections, and the Bezier curves have been used for the parameterization of the section displacements. The Bezier curves allows to reduce the degrees of freedom, and they define the position of the airfoils on the circumferential plane compared to the original position. A Bezier curve with four control points (at 0%, 33%, 66%, 90% of the span) has been built to define the displacement angle range $\Delta\theta$ of the section 1 to the section 12. For the last two sections, the optimization coefficients $\Delta\theta$ have been kept independent. For the optimization process, the genetic algorithm has been used, in particular MATLAB GA. As the computer has 12 CPUs, it has been decided to run the simulation in parallel mode on 10 CPUs. The computational time of the optimization of the blade tip was about 7 days. The computational time for the optimization of the whole blade was high, hence, the hierarchical GA has been considered to accelerate the genetic algorithm. Therefore, the computational time of the optimization of the blade was about 10 days.

In the optimization of the blade tip, the individuals on the Pareto front have a significant increase of the isentropic efficiency and no significant variation of the

pressure ratio. The efficiency increase is about 0.7%, and it is be considered satisfying because the flow that affects a transonic compressor rotors is complex. They are characterized by strong shock waves and secondary flows that reduce the performances. Previous studies analyzed the performance of the NASA Rotor 37. The results obtained showed an isentropic efficiency increase of about 1.5% by moving the stacking line of the blade. The NASA Rotor 67 is a more complex rotor than the Rotor 37 and it was already optimized by the NASA laboratory. Hence, the results obtained in this thesis are satisfying. In the optimization of the whole blade there is an increase of isentropic efficiency of 0.5%, and a meaningless pressure ratio increase of about 0.09%. From a comparison between the efficiency of the original blade and the optimized blade, it has been seen that the increase of the efficiency occurs especially near the hub. The reason is that there is an increase of the mass flow rate in the hub region, this fact entails a better incidence angle of the flow and hence a delay of the flow separation. The optimization of the performance in this region is important because the hub corner stall can happen in the transonic compressor. The hub corner stall causes a decrease of efficiency due to the recirculation zone near hub that generates a vortex. The increase of the isentropic efficiency in the tip region is not so high, but this little increase is due to a reduction of energy dissipation during the flow mixing.

A suggestion for the future studies is to increase the number of generations and individuals. In this thesis the number of generations is 10 and the number of the individuals is 6 for the optimization of the blade tip and 10 for the optimization of the whole blade. Another possible future work is to include in the optimization of the blade tip the shape configuration with a negative displacement angle of the control point at 95% of the span and a positive displacement angle of the control point at 100% of the span, and vice versa. Finally, it could be interesting to analyze the flow with the coupling rotor-stator. In this way, it could be seen how the secondary flows influence the stator performances, and hence, the performances of the whole stage.

# Appendix A

# Additional results

## A.1 Optimization of the blade tip

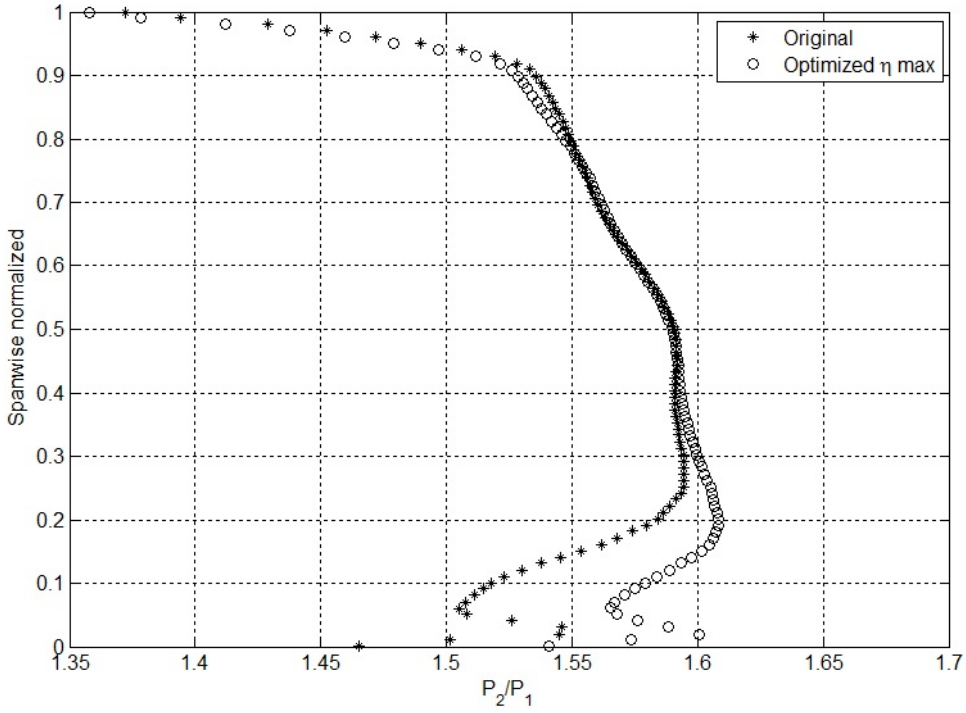


**Figure A.1:** Fig. PR of the original blade and the optimized blade just downstream the blade

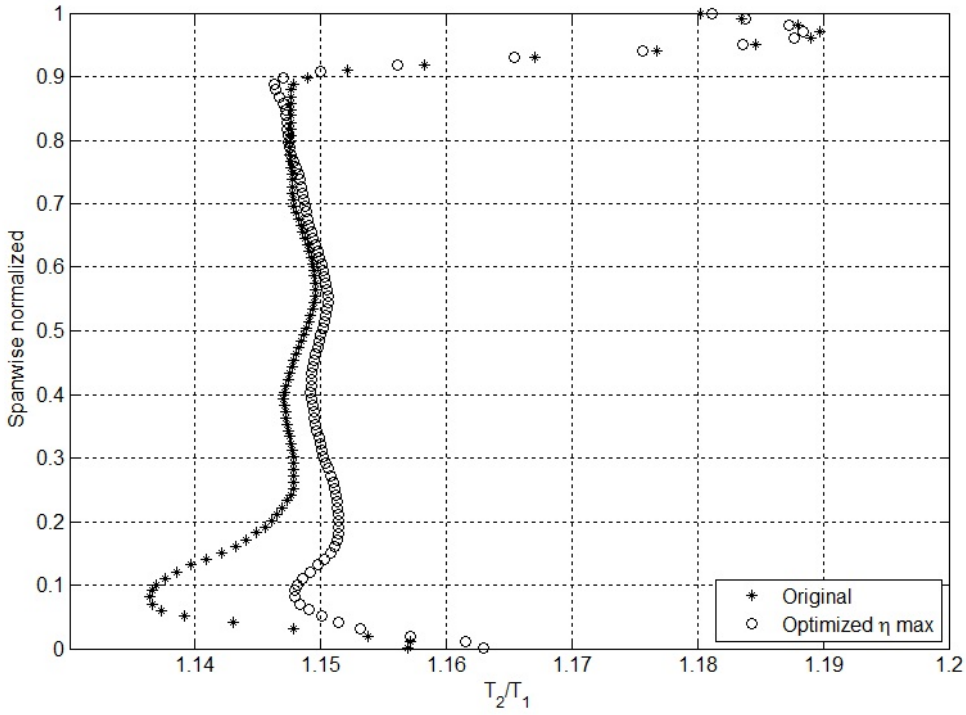


**Figure A.2:** Fig. Total temperature ratio of the original blade and the optimized blade just downstream the blade

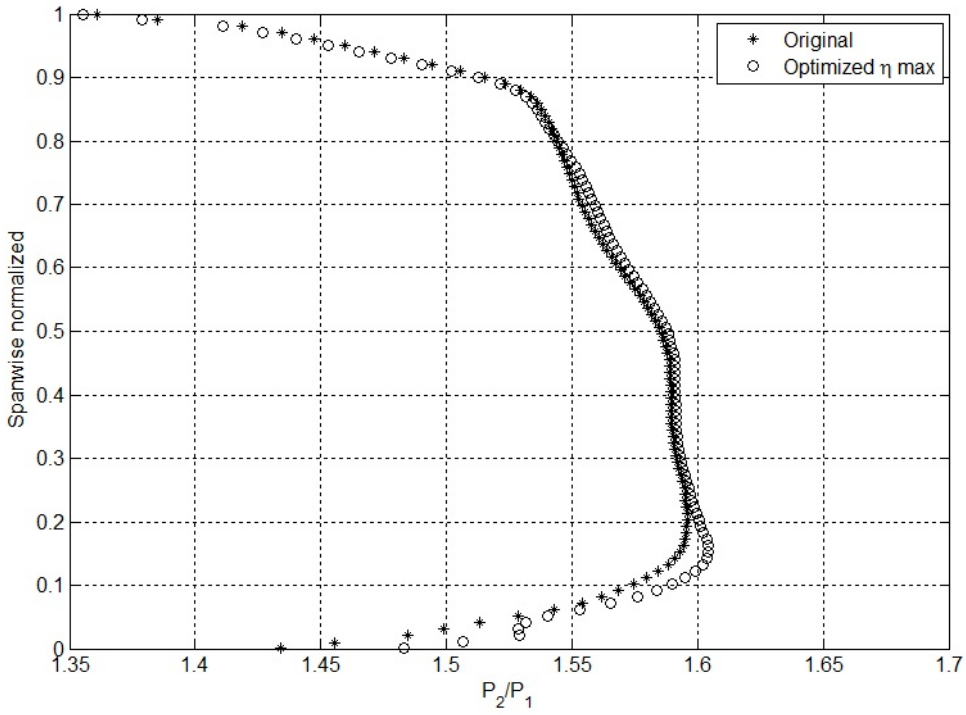


**Figure A.3:** Fig. PR of the original blade and the optimized blade one chord downstream

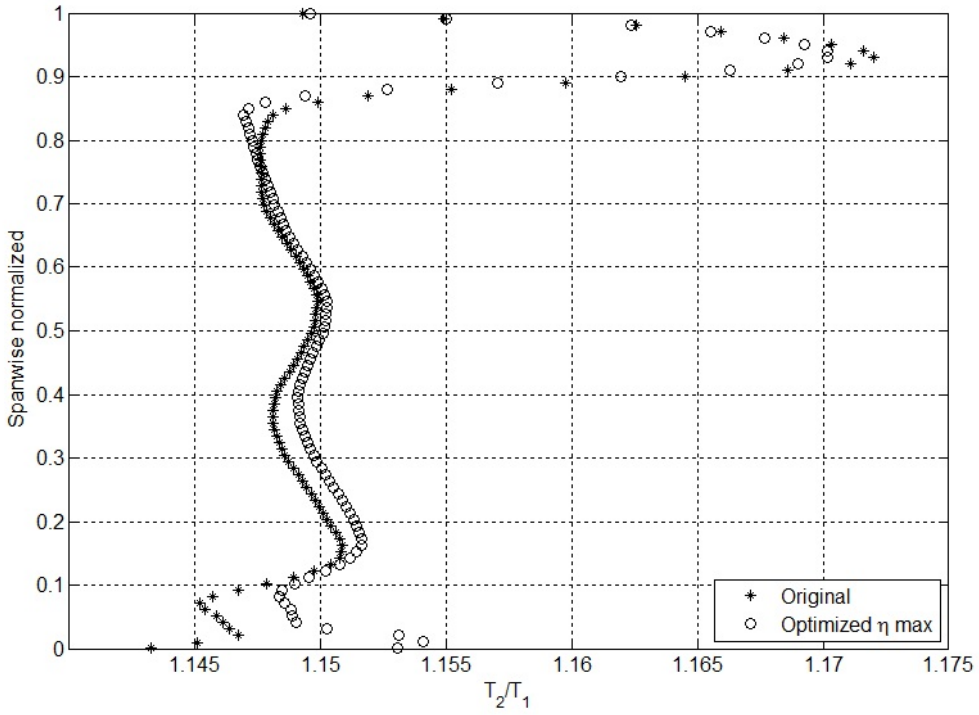


**Figure A.4:** Fig. Total temperature ratio of the original blade and the optimized blade one chord downstream

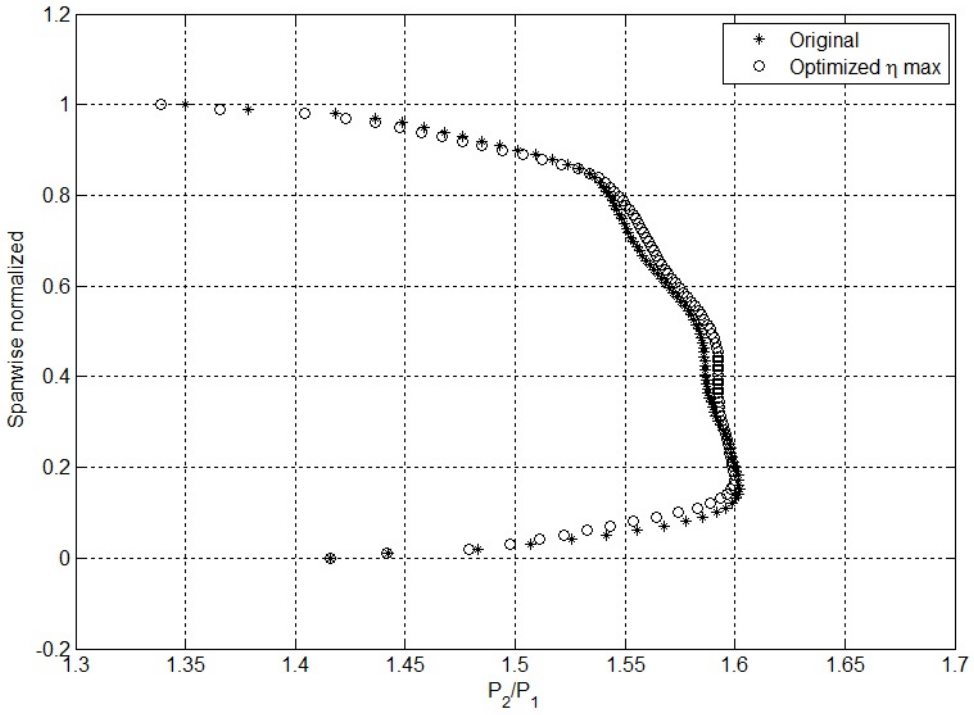


**Figure A.5:** Fig. PR of the original blade and the optimized blade at the duct outlet.

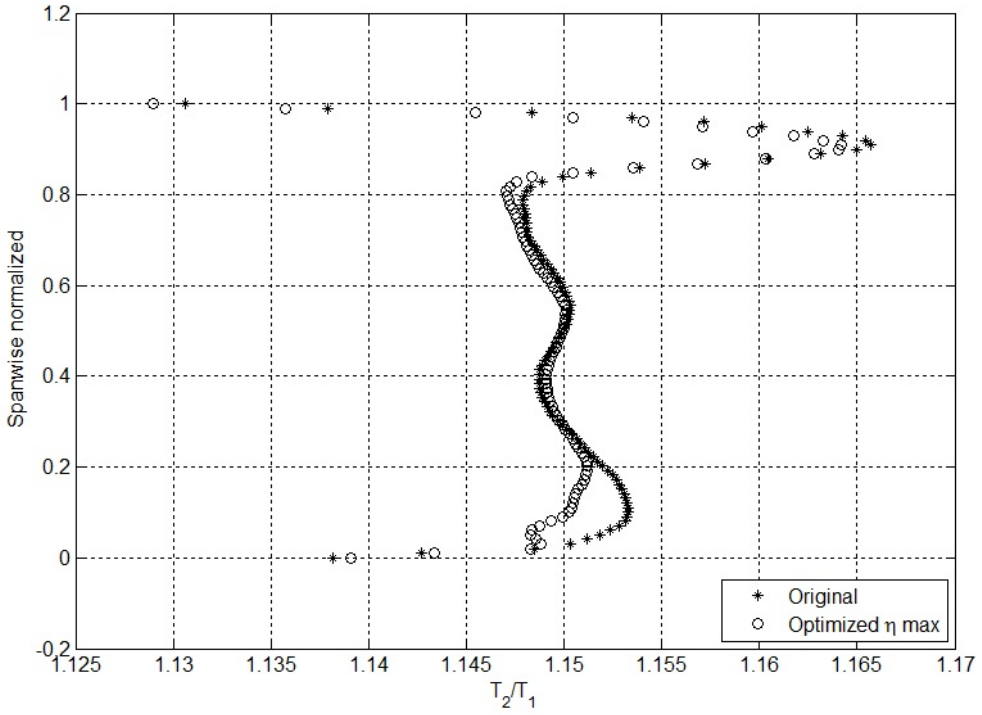


**Figure A.6:** Fig. Total temperature ratio of the original blade and the optimized blade at the duct outlet.

## A.2 Optimization of the whole blade

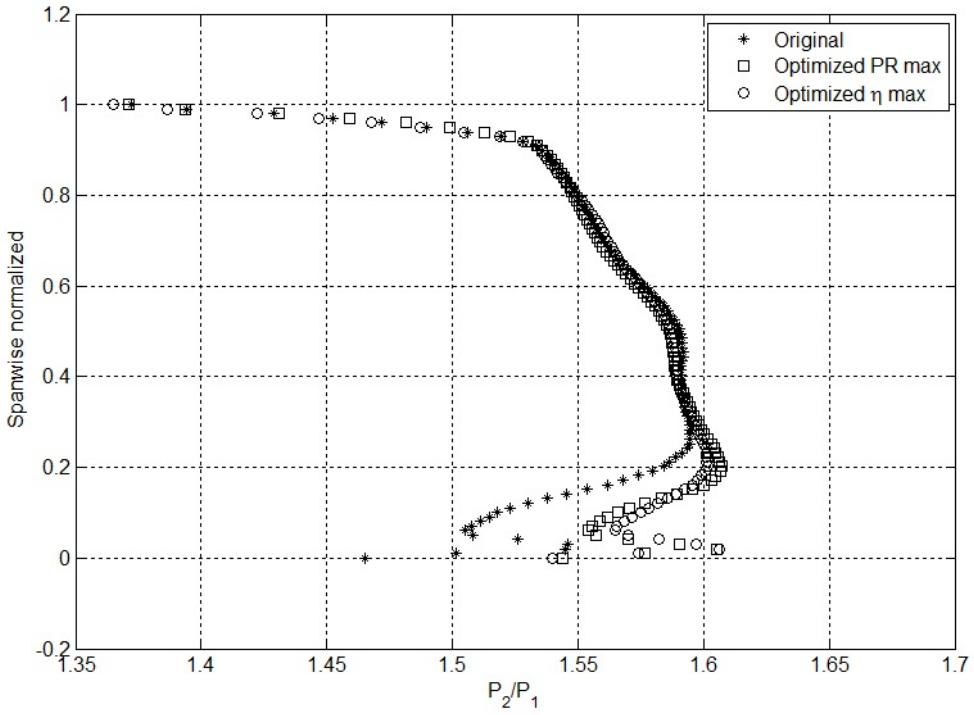


**Figure A.7:** PR of the original blade and the optimized blades just downstream the blade

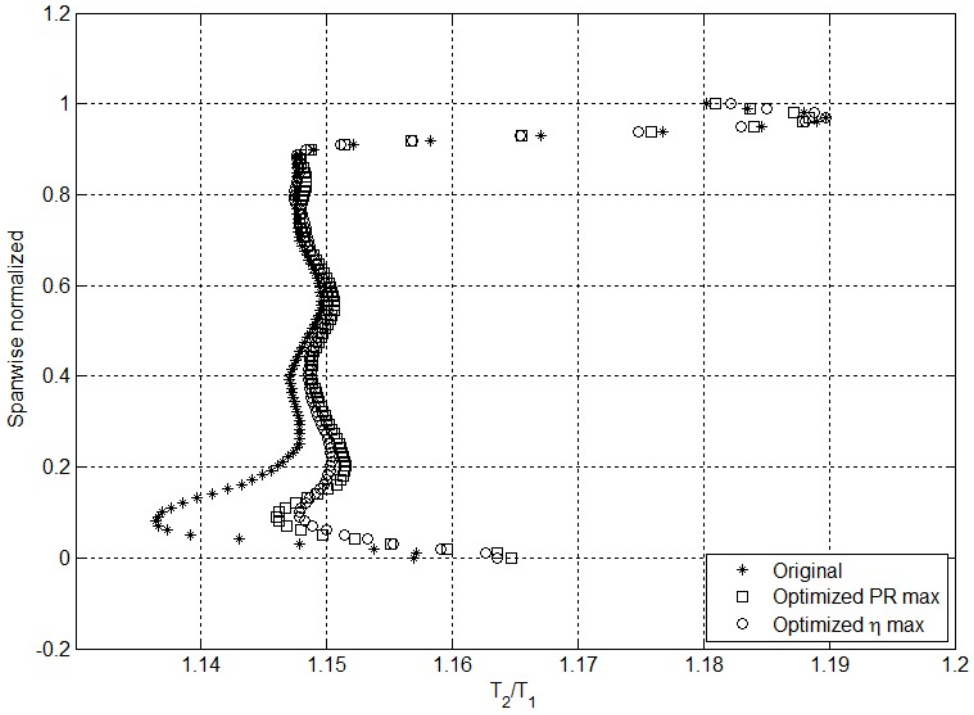


**Figure A.8:** PR of the original blade and the optimized blades just downstream the blade

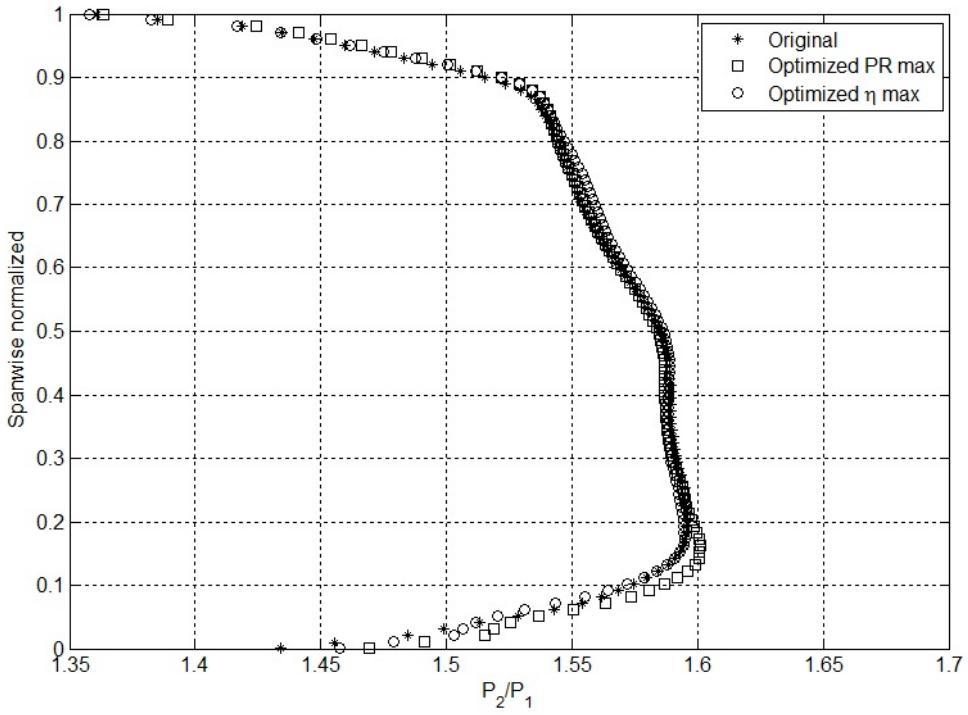


**Figure A.9:** PR of the original blade and the optimized blades one chord downstream

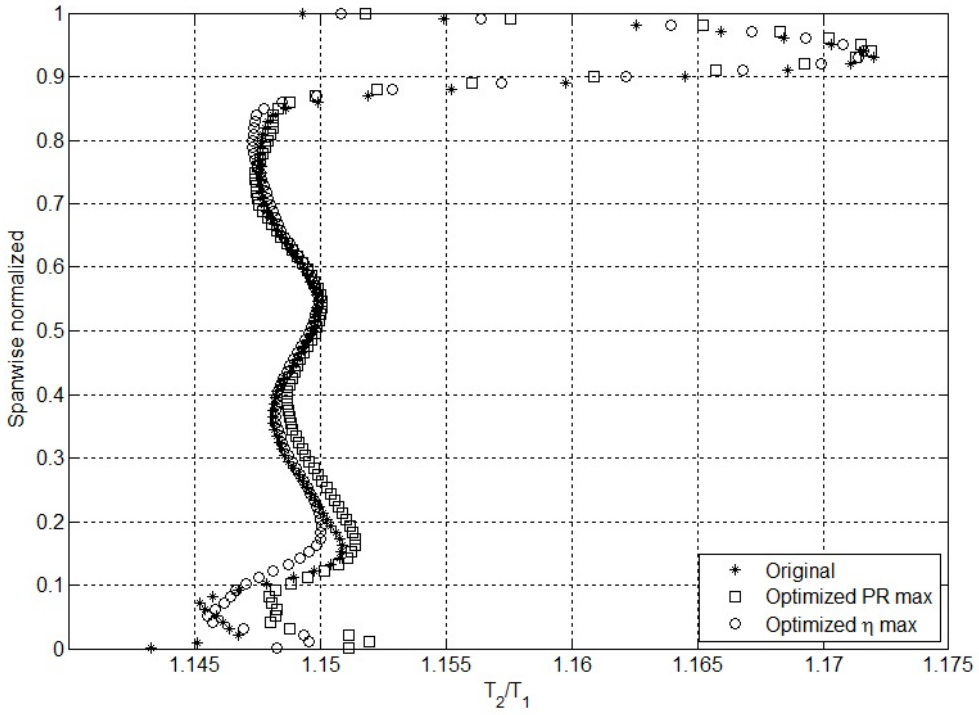


**Figure A.10:** PR of the original blade and the optimized blades one chord downstream

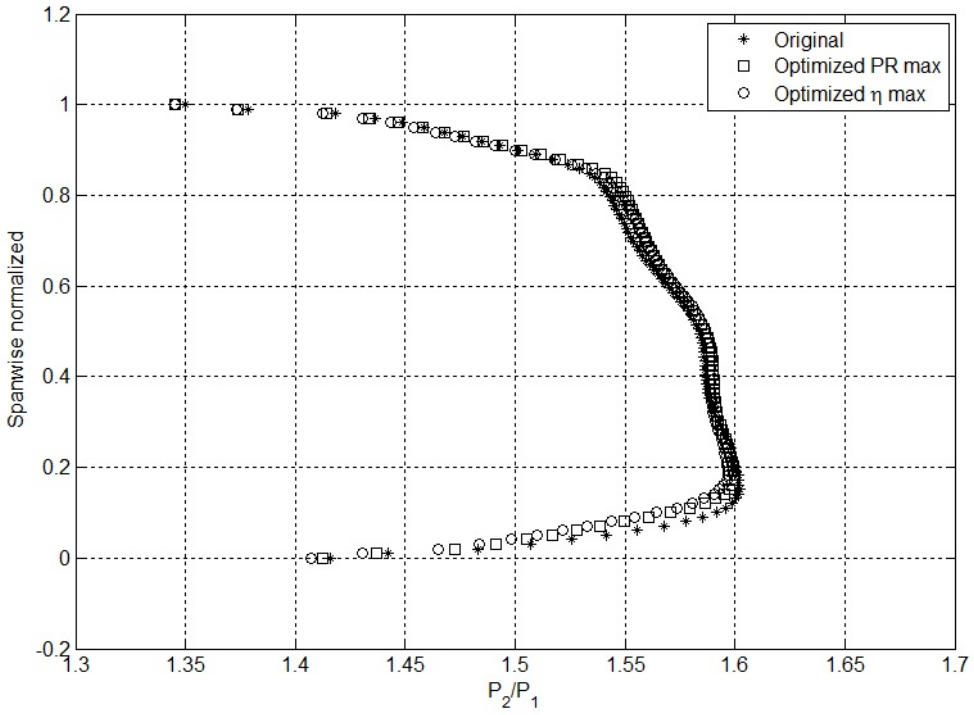


**Figure A.11:** PR of the original blade and the optimized blades at the duct outlet

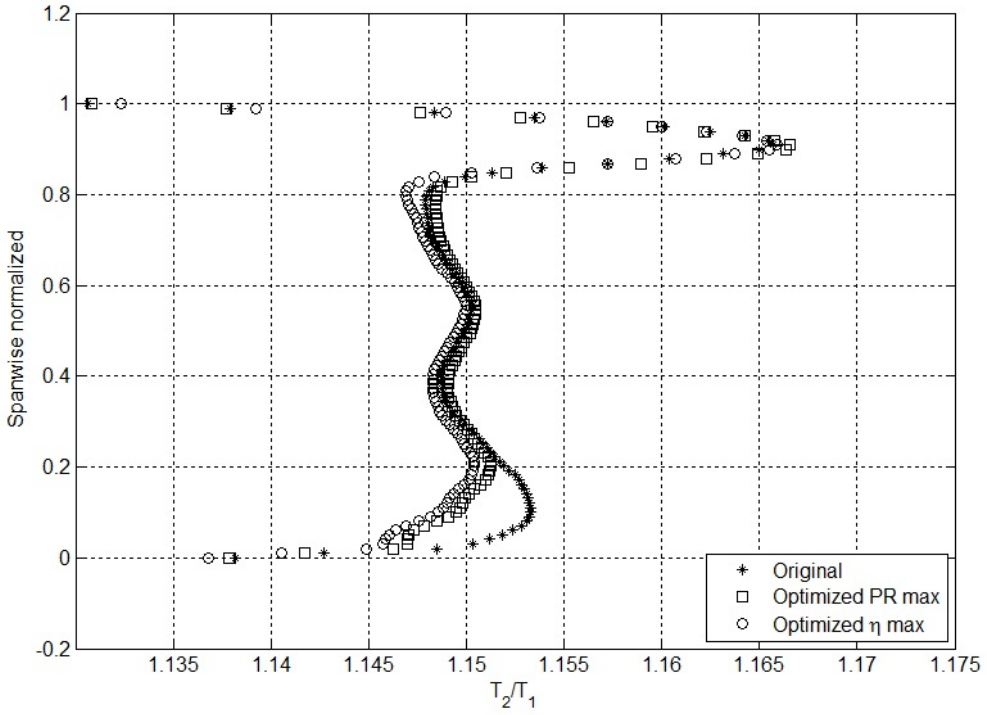


**Figure A.12:** PR of the original blade and the optimized blades oat the duct outlet

# Bibliography


[1] Cumpsty, N. A., *Compressor Aerodynamics*, Longman, 1989.

[2] Biollo, R., *Systematic Investigation on Swept and Leaned Transonic Compressor Rotor Blades*, Ph.D. thesis, Scuola di Dottorato di Ricerca in Ingegneria Industriale, Universita' degli Studi di Padova, 2008.

[3] Hah, C. A., "Numeric modeling of endwall and tip-clearance flow of an isolated compressor rotor," *Trans. ASME Journal of Engineering for Power*, 1986.

[4] N. Yamaguchi, T. Tominaga, S. Hattori, and T. Mitsubishi, "Secondary-Loss Reduction by Forward-Skewing of Axial Compressor Rotor Blading," *Proceedings of 1991 Yokohama International Gas Turbine Congress*, Vol. 2, 1991.

[5] Ernesto Benini and Roberto Biollo, "On the aerodynamics of swept and leaned transonic compressor rotors," *Proceedings of ASME Turbo Expo 2006, Power for Land, Sea and Air*, 2006.

[6] Garbo, A., *Performance improvement assessment of a new tehcnology for VIGVs*, Master's thesis, Tesi di laurea, Facoltà di Ingegneria, Università degli Studi di Padova, 2012.

[7] Ernesto Benini and Roberto Biollo, "Impact on sweep and lean on the aerodynamic behavior of transonic compressor rotors," *The Future of Gas Turbine Technology*, $4^{th}$ International Conference, 2008.

[8] H. Starken and H. J. Lichfuss, "Some experimental results of two-dimensional compressor cascades at supersonic inlet velocities," *Trans. ASME Journal of Engineering for Power*, 1970.

[9] L. B. Ginder and W. J. Calvert, "The design of an advanced civil fan rotor," *Trans. ASME Journal of Engineering for Power*, 1987.

[10] G. R. Miller, G. W. Lewis, and M. J. Hartmann, "Shock losses in transonic rotor rows," *Trans. ASME Journal of Engineering for Power*, 1961.

[11] C. Freeman and N. A. Cumpsty, "A method for the prediction of supersonic compressor blade performance," *Paper to the* $34^{th}$ *ASME Gas Turbine Conference and Exposition*, 1989.

[12] J. D. Denton and L. Xu, "The effect of Lean and Sweep on Transonic Fan Performance," *ASME Paper GT-2002-30327*, 2002.

[13] J. Bergner, D. K. Hennecke, M. Hoeger, and K. Engel, "Darmstadt Rotor No. 2 - Part II. Design of leaned rotor blades," *ISROMAC 9*, 2002.

[14] Benini, E., "Three-Dimensional Multi-Objective Design Optimization of a Transonic Compressor Rotor," *Journal of Propulsion and Power*, Vol. 20, 2004, pp. 559–565.

[15] J. Periaux, L. F. Gonzalez, and D. S. Lee, "MOO Methods for Multidisciplinary Design Using Parallel Evolutionary Algorithms, Game Theory and Hierarchical Topology: Theoretical Aspects," *Introduction to Optimization and Multidisciplinary Design in Aeronautics and Turbomachinery*, Vol. Lecture Series 2010-07, 2010.

[16] Verstraete, T., "Introduction to Optimization and Multidisciplinary Design," *Introduction to Optimization and Multidisciplinary Design in Aeronautics and Turbomachinery*, Vol. Lecture Series 2010-07, 2010.

[17] Jun Li, Hiroshi Tsukamoto, and Nobuyuki Satofuka, "Optimization of Aerodynamic Design for Cascade Airfoil by Means of Boltzmann Selection Genetic Algorithms," *A Collection of the 18th AIAA APPLIED AERODYNAMICS CONFERENCE Technical Papers*, Vol. 2, AIAA, 2000, p. 864.

[18] J. Harinck, Z. Alsalihi, J. P. Van Buijtenen, and R. A. Van den Braembussche, "Optimization of a 3D Radial Turbine by Means of an Improved Genetic Algorithm," *Proceedings of the 6th European Conference on Turbomachinery*, 2005, pp. 1003–1042.

[19] K. C. Giannakoglu and M. K. Karakasis, "Hierarchical and Distributed Metamodel-Assisted Evolutionary Algorithms," *VKI Lecture Series on Introduction to Optimization and Multidisciplinary Design*, 2006, pp. 111–145.

[20] M. K. Karakasis, K. C. Giannakoglu, and D. G. Koubogiannis, "Aerodynamic Design of Compressor Airfoils using Hierarchical, Distributed, Metamodel-Assisted Evolutionary Algorithms," *7th European Conference on Turbomachinery, Fluid Dynamic and Thermodynamics*, 2007.

[21] V. Torczon and M. W. Trosset, "Using approximations to accelerate engineering desifn optimization," Tech. rep., ICASE report, 1998.

[22] *ANSYS CFX User Guide.*

[23] *Matlab R2011a User Guide.*

[24] C. Hah and J. Loellbach, "Development of Hub Corner Stall and Its Influence on the Performance of Axial Compressor Blade Rows," *Journal of Turbomachinery*, 1999.